

Synchronization between two Hele-Shaw cells

A thesis presented by
Ms Angela Bernardini Gagliani
in partial fulfillment of the requirements
for the Degree of Doctor in Applied Mathematics



UNIVERSITY OF NAVARRA
Department of Physics and Applied Mathematics
Faculty of Science

University of Navarra, E-31080 Pamplona, Navarra

Synchronization between two Hele-Shaw cells

A thesis presented by
Ms. Angela Bernardini Gagliani
in partial fulfillment of the requirements for
the Degree of Doctor in Applied Mathematics

October 2005

Department of Physics and Applied Mathematics,
Faculty of Science, University of Navarra,
E-31080 Pamplona, Spain

Doctoral thesis of the Faculty of Science
University of Navarra, Pamplona (Spain)
Angela Bernardini Gagliani (angela@fisica.unav.es)
[\(http://fisica.unav.es/~angela/\)](http://fisica.unav.es/~angela/)
Synchronization between two Hele-Shaw cells
Pamplona, 2005.

This document has been written with PDFL^AT_EX, Version 3.14.

D. Jean Bragard, Profesor del Departamento de Física y Matemática Aplicada de la Universidad de Navarra

CERTIFICA: que la presente Memoria, “Synchronization between two Hele-Shaw cells” ha sido realizada bajo mi dirección en el Departamento de Física y Matemática Aplicada de la Universidad de Navarra por Angela Bernardini Gagliani.

Para que conste, en cumplimiento de la legislación vigente, firmo la presente certificación en Pamplona, el DIA de octubre de dos mil cinco.

Fdo.: Jean Bragard

Ai miei genitori

Acknowledgments

In writing this investigation, I owe a great debt to the joint contribution of several people to whom I wish to express my deep gratitude.

First of all, I wish to thank the European project director Dr. Hector Mancini to have made possible my stay at the department of Physics and Applied Mathematics. As he said: “Ho comprato a scatola chiusa”.

I am very grateful to my scientific advisor Dr. Jean Bragard, with whom I have worked closely for many months, who has prepared and driven me for the realization of this research. But first of all, to be a friend.

I thank Pierre Dauby for his indispensable collaboration started with my stay at Liége University during the years 2004 and continuing until now.

Dr. Stefano Boccaletti contributed with many useful comments and precious discussions for the final elaboration of the manuscript.

I remember my colleagues for the shared pains and laughs, and for all the unforgettable moments that we have enjoyed together: Iker Zuriguel, Martin Pastor, Andrea Vallone, Sergio Casado, Santiago Madruga, Carolina Mendoza, Begoña Peña, Montserrat Miranda, Roberto Arevalo, Cristian Mankoc...

in particular I specially thank Maria Yoldi for having stood my final hysteria and Alberto De La Torre for being the representant of the “egoismo inteligente”.

I thank Thomas Desaive and Huguette Croisier for having me introduced to the tools of the bifurcation theory and to AUTO!!

Many thanks are also addressed to all the department and all the professors who contributed to the completion of this thesis in various way: Wenceslao González-Viñas, Angel Garcimartín, Sergio Ardanza, Carlos Pérez García, María-Jesús Chasco, Pedro Elizalde, Emilio Díaz, Carmen Palacios, Antonio Peláez, Jorge Elorza, Fernando Varela, Diego Maza, Pilar Ayucar, Marijose Collado, Paulina Maza, Manu Mancini...

My deep gratitude goes to Javier Burguete for worrying and taking care of ALL of us students... for realizing some bad moments and comforting me with precious suggestions.

A very special thanks goes to professor Paolo Emilio Ricci who taught me the basics of research and always encourages me to go forward.

I thank Cecilia Wolluscheck that have been my Spanish's teacher, my colleagues of journey, of party and of all the best I remember of Spain.

Benedicte Delsenne has became unforgettable in four months only. "Les deux folles!" Do you remember?

Thanks also to Teresa Pierantozzi for being always by my side.

In addition, I would like to thank the European project COSYC OF SENS (Grant Number BFM 2002-02011) for the financial support which I received from 2001 to 2004 and "La Asociación de Amigos" of the University of Navarra for the fellowship during the course 04-05. I also thank the University of Liège for the grant during my stay in Belgium.

I thank Vitoriano, María Dolores, Nerea and Miguel Etayo for treating me as a daughter and a sister.

Special thanks for their unwavering support and encouragement go to my two favorite beginners mathematicians Anna and Andrea Bernardini. They always observe me suspiciously when I am with my laptop. And I always wait for the same question: Could you explain us, once more, what happens with that rolls?!?!

Finally, I thank Iñaki Etayo for helping me discover something that I never thought I could find during my investigation.

Contents

1	Introduction	1
1.1	Thermal Convection	3
1.1.1	Instability mechanism: Rayleigh-Bénard convection .	4
1.2	Hele-Shaw cell and porous media	6
1.3	Synchronization	7
1.3.1	Complete synchronization	8
1.4	The scope of this work	9
2	Mathematical Formulation	11
2.1	Model equations	11
2.1.1	Stream function equation reformulation	14
3	From Stationary Convection to Chaos	17
3.1	Results of numerical simulations	18
3.2	Conclusions	32
4	Stability analysis	35
4.1	Linear analysis	35
4.1.1	Linearized equations for the perturbations	36
4.1.2	Results	38
4.2	Non linear analysis	43
4.2.1	Computing bifurcation diagrams with AUTO	44
4.2.2	Non linear problem formulation	45
4.2.3	The linear problem	46
4.3	Linear adjoint problem and bi-orthogonal relations	51
4.3.1	Linear adjoint problem	51

4.3.2	Bi-orthogonal relations (I)	52
4.3.3	Bi-orthogonal relations (II)	52
4.4	General expression for the amplitude equations	53
4.4.1	Projection	54
4.4.2	Summary of the amplitude equations	55
4.5	Dynamics reduction	56
4.6	Results	57
4.7	Conclusions	64
5	Synchronization	67
5.1	All internal points are connectors	67
5.2	Coupling through the lateral walls (only)	73
5.3	Finite number of internal points are used as connectors	75
5.4	Non uniform grid	76
5.5	Conclusions	78
6	Conclusions	81
A	Finite Difference methods	85
A.1	Solution of diffusive initial value problem	85
A.2	Implicit scheme	87
A.2.1	Alternating-Direction Implicit scheme	87
A.3	The non-linear term	88
A.3.1	ADI scheme revisited	91
A.4	Boundary value problem	93
A.4.1	Explicit time-stepping procedure	94
B	Spectral collocation method	97
B.1	Chebyshev points	98
B.2	Solving the eigenvalue problem	100
	Bibliography	105

List of Figures

1.1	Hexagonal cells in spermaceti	3
1.2	Organization of convective motions into rolls cell	4
1.3	Hele-Shaw cell experimental device	6
2.1	Schematic representation of a Hele-Shaw cell heated from below	16
3.1	Stationary convection at $Ra = 44$	18
3.2	Temperature fluctuation field at $Ra=400$	20
3.3	Periodic convection at $Ra = 400$	21
3.4	Quasi-periodic convection at $Ra = 520$	23
3.5	Stroboscopic technique	24
3.6	Temperature fluctuation field at $Ra = 600$	25
3.7	Evolution of frequency spectra from $Ra = 505$ to $Ra = 560$	26
3.8	Temperature fluctuation field at $Ra = 900$	28
3.9	Periodic convection at $Ra = 900$	29
3.10	Chaotic convection at $Ra = 1200$	30
3.11	Autocorrelation function	31
3.12	Spatial correlation function	32
4.1	M_{00} mode with $Ra_c = 39.4784$, M_{10} mode with $Ra_c = 61.6850$ and M_{11} mode with $Ra_c = 109.6623$	40
4.2	M_{20} mode with $Ra_c = 157.9137$, M_{30} mode with $Ra_c = 178.2697$ and M_{21} mode with $Ra_c = 185.3292$	41
4.3	M_{31} mode with $Ra_c = 246.7401$, M_{01} mode with $Ra_c = 246.7401$ and M_{40} mode with $Ra_c = 266.8741$	42
4.4	M_{00} mode with $s_1 = 0$, zero mode with $s_2 = -9.8696$, M_{01} mode with $s_3 = -17.7652$	48
4.5	Zero mode with $s_4 = -39.4784$, M_{01} mode with $s_5 = -41.4523$, M_{11} mode with $s_6 = -59.2176$	49

4.6	M_{20} mode with $s_7 = -63.1654$, zero mode with for $s_8 = -88.8264$, M_{02} mode with $s_9 = -94.7482$	50
4.7	Steady branches for the uni-cellular solution	59
4.8	Periodic branches for the uni-cellular solution	62
4.9	Bifurcation diagram for the M_{20} mode	63
4.10	Schematic representation of the quasi-periodic regime stability	64
5.1	Complete synchronization for steady convection at $Ra = 44$	68
5.2	Complete synchronization for periodic convection at $Ra = 400$	69
5.3	Pearson's coefficient for cross correlation	70
5.4	Lissajous-type of plot for stream functions	71
5.5	Space-time plots of the two convective cells	72
5.6	Synchronization errors. All internal points are connectors .	73
5.7	Synchronization errors. Connectors onto the lateral walls .	74
5.8	Comparison of synchronization errors.	76
5.9	Uniform grid and no uniform grid	77
5.10	Synchronization of periodic hele-Shaw cells with non uniform connectors.	78
5.11	Synchronization of quasi-periodic and chaotic Hele-Shaw cells with non uniform connectors.	79
B.1	Spectral accuracy	98
B.2	Geometrical interpretation of the Chebyshev points	99
B.3	Tensor product grid	102

List of Tables

4.1	Spectrum of the critical Rayleigh numbers	39
4.2	Spectrum of the linear growth rate for $\delta = 0$	57
4.3	Position of the first five bifurcation points	60
4.4	Hopf bifurcation and torus bifurcation points of the M_{00} mode	61

Chapter 1

Introduction

If we look around us, we realize that synchronization phenomena appear in nature and social life in different forms and situations: clocks, applauding audience, different forms of behavior of insects [1; 2; 3]... The mechanisms which bring to synchronization are clearly different, since the nature of the objects is different, however they share the same principle: they acquire a common regime.

Theoretical descriptions of these behaviors started in the sixteenth century with Christian Huygens [4]. Observing two pendulum clocks hanging on a wall, he justified the conformity of their rhythms by a motion of the beam. After this seminal contribution many others have followed, bringing the synchronization scenario in many situations. Recently several authors have made synchronization getting closer to another colossal field of research: *Chaos*[5; 6]. For many, one of the most promising field of research, it has been the cause of many questions and debates: What is chaos? What are the routes to chaos? Can you control chaos? Is it possible to synchronize several chaotic systems?

As a first tentative definition, chaos is related with transition from periodic motions, with high regularity and order, to irregular or erratic motions [7]. Both theoretical and experimental investigations have revealed that there is not a unique way in which chaos arises. Landau [8] postulated that chaos is caused by an infinite sequence of Hopf bifurcations. Each bifurcation adds a new fundamental frequency. Thus, as more and more frequencies occur, the motion gets more and more chaotic. However, others authors showed that only two bifurcations are precursory to chaos. Period doubling route is based on the original idea of Landau. If the sequence of period doubling

is infinite the period quickly approach infinity. Pomeau and Manneville [9] also introduced the idea of intermittency, which add a new scenario for the transition from periodic to chaotic dynamics. It refers to oscillations that are periodic for time intervals and then interrupted by bursts of aperiodic oscillations of finite duration. Perora and Caroll [10] showed that it is possible to synchronize chaotic systems, creating the fundamentals to a possible control.

There are two ways for controlling chaos [11]: a (negative) feedback control [12] and a non feedback one [13; 14; 15]. The first one stabilizes an unstable reference orbit by time-dependent perturbations. On the contrary, the other one is not related to certain particular trajectory and in this case controlling chaos means suppression of chaos.

Questions about synchronization in extended chaotic systems have been the starting point of this thesis. The answers that one can give to this so general subject depend on many factors: which systems do we consider, which kind of chaos, which interaction do we apply or which state of synchronization are we looking for. Very likely due to historical reasons in our department, the investigation has been driven to possible synchronization mechanisms in fluid systems. In particular, we have chosen the Hele-Shaw cell [16]. This device is constituted of two transparent plates separated by a small gap. In the interior of the cell, a fluid is heated from below. This is a quite simple system, nevertheless, it is able to reproduce very complex dynamics. The geometry of the Hele-Shaw cell has the advantage of reducing the problem to two spatial dimensions. The analogy of the Hele-Shaw cell with a fluid saturated porous media permit to use important results in the field of porous media for our analysis [17].

In most cases, studies of synchronization have considered external forcings, bidirectional symmetric or unidirectional master-slave coupling configurations. With a bidirectional coupling the trajectories of both systems will change to follow a common new trajectory. With a unidirectional coupling, the trajectories of the response system will converge to the same values as the drive system, and they will remain in step with each other. However recent research has also considered asymmetric coupling configurations [18], due to the impossibility in practical situations to have purely unidirectional or perfectly symmetrical couplings.

Depending of the final conditions of the synchronized systems, it is possible to identify several states of synchronization [19]. In the following sections

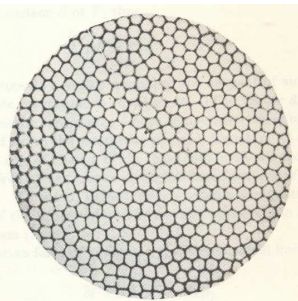


Figure 1.1: Bénard cells in spermaceti. A reproduction of Bénard's original photograph [21].

we formally introduce the concepts of thermal convection, Hele-Shaw cell and synchronization.

1.1 Thermal Convection

The origin of the term *convection* [20], from the Latin “*convectio*”, gives an idea of “carrying with” and it seems to have been used in physics, for the first time, to denote the transport of heat through fluid motion. Earliest description has been written around 1790 by Benjamin Thompson, Count Rumford, who investigated the properties and management of heat. The most significant and systematic experimental work has been carried out by H. Bénard [21] at the beginning of the twentieth century. He studied a seemingly simple convective system which he never knew being so complicated. In fact, in many experiments he used fluid heated from below with no confining plate on the top surface. In this arrangement the top surface is free to move and deform. It was not realized until 1956 that this can lead to an instability mechanism involving gradients in the surface tension. This situation is now called Bénard-Marangoni convection. Bénard observed a first phase in which the fluid formed cells of almost regular shapes, nearly polygons of four to seven sides, which evolved to equal and regularly spaced hexagons, as shown in Fig. 1.1. The circulation of the fluid in the hexagonal cells is generally upwards in the center (up-hexagons) and downwards along the rim. In 1900, convection became the principal subject of investigation of Lord Rayleigh [22]. In one of his last article published in 1916

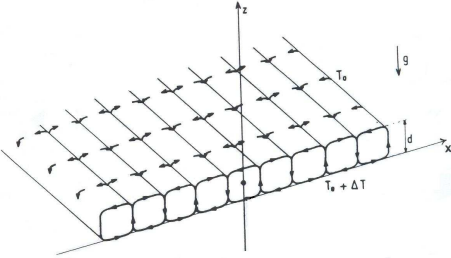


Figure 1.2: Schematic diagram of the organization of convective motions into rolls cells.

he explained what is now known as Rayleigh-Bénard convection. A thin layer of fluid, heated from below, is fully confined between two plates, so that there is no gap (free surface) at the top of the fluid layer. In the case of pure gravity-driven instability, there is an organization of ascending and descending motions in the form of rolls, alternatively turning clockwise and counter-clockwise in space, as shown in Fig. 1.2.

1.1.1 Instability mechanism: Rayleigh-Bénard convection

Let us consider a Newtonian and isotropic fluid layer confined between two rigid horizontal plates, heated from below [20]. If the temperature gradient is small, the temperature profile is purely conductive, and then linear. If we consider a small ascending displacement of a fluid element, this will be surrounded by denser regions producing a net buoyant force that will sustain the initial displacement. Neglecting the molecular diffusion, the fluid element continues to rise and the Archimede's buoyant force amplifies. Convective motion starts when the temperature difference goes beyond a critical value. A fluid element, at height z , is subjected, per unit volume, to the buoyancy force $g\delta\rho = g\alpha\rho_0\delta T$, where g is the acceleration of gravity and δT is the temperature difference between the fluid element and its neighbors, having assumed a linear variation of the density $\rho = \rho_0(1 - \alpha(T - T_0))$, where T is the temperature of the fluid particle, α is the volume expansion coefficient and ρ_0 the fluid density at the reference temperature T_0 . Since the temperature profile is linear, the buoyancy force is $\alpha\rho_0g\Delta Tz/h$, where h is the height of the layer and ΔT is the temperature difference between

the horizontal plates. The equation governing the motion of a fluid particle admits an exponential solution as $z \sim e^{t/\tau_{grav}}$ [23; 24], where τ_{grav} is the time scale related to gravity

$$\tau_{grav} = \sqrt{\frac{h}{\alpha g \Delta T}}. \quad (1.1)$$

This mechanism of instability does not develop suddenly. There exist in fact, two inhibiting factors that tend to dampen this motion. The first one is the viscosity of the fluid, μ , which slows down the motion of the particles. It defines a characteristic time

$$\tau_{visc} = \frac{\rho_0 h^2}{\mu}. \quad (1.2)$$

The second inhibiting factor comes from the exchange of heat between fluid particles at different temperatures. This factor increases as the fluid thermal diffusivity, κ , is larger. We can also define an associated characteristic time with this damping mechanism

$$\tau_{therm} = \frac{h^2}{\kappa}. \quad (1.3)$$

Comparing the characteristic times given by Eqs. (1.1)-(1.3), we can say that the instability takes place when the destabilizing effects are faster than the stabilizing ones, that is when $\tau_{grav}^2 \ll \tau_{visc}\tau_{therm}$ or, in other form

$$Ra = \frac{\tau_{visc}\tau_{therm}}{\tau_{grav}^2} = \frac{\rho_0 g \alpha \Delta T h^3}{\mu \kappa} \gg 1. \quad (1.4)$$

The above relation defines the *Rayleigh number* as the dimensionless parameter which indicates the stability of a fluid layer subjected to a vertical thermal gradient. The simpler parameter for controlling the convection is the temperature difference across the fluid layer. Below a certain critical value, the stabilizing effects drive the fluid back to a conductive rest state. Beyond threshold, the Archimedean force dominates and fluid motion is observed in the layer. For a critical value of the temperature difference, it corresponds a critical value of the Rayleigh number. The critical Rayleigh number is defined as the value of the Rayleigh number from which instability sets in

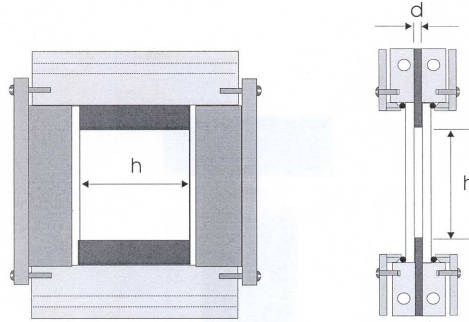


Figure 1.3: Hele-Shaw experimental set up ($d \ll h$), (H. Mancini).

$$\begin{array}{lll} Ra < Ra_c & \text{stable system} & (\text{conduction}), \\ Ra > Ra_c & \text{unstable system} & (\text{convection}). \end{array}$$

1.2 Hele-Shaw cell and porous media

The Hele-Shaw cell, an assembly for fluid investigation and visualization, was named from Henry S. Hele Shaw, the British engineer who devised it around the turn of the twentieth century. This device has recently attracted great interest, due to its simple geometry and its various applications. The cell consists primarily of two transparent plates separated by a small gap, so that one dimension is much smaller than the other two, as shown in Fig. 1.3. In particular, the Hele-Shaw flows have been studied for their potential applications to coastal engineering, water resources, oil industry drilling and more recently in micro-mechanical-electrical systems and biomedical engineering. The success of the Hele-Shaw cell is also coming for its contribution to the understanding of thermal convection in porous medium, the latter being important for a wide range of applications in industrial and geological researches.

In a fluid saturated porous medium, low-Reynolds number flow of an incompressible fluid is described by a linear pressure-velocity relation, called Darcy law [25]

$$\mathbf{v} = \frac{K}{\mu}(-\nabla p + \rho \mathbf{g}) \quad (1.5)$$

where \mathbf{v} is the filtration velocity vector, ∇p the pressure gradient, ρ the fluid density, μ the dynamic viscosity, K the permeability of the medium and \mathbf{g} the acceleration due to gravity. The analogy between an isothermal two-dimensional flow in a porous medium and the motion of an isothermal fluid between two parallel walls separated by a distance d , was first shown by Hele-Shaw [16]. The mean velocity for the flow through a Hele-Shaw cell is given by

$$\mathbf{v} = \frac{d^2}{12\mu}(-\nabla p + \rho\mathbf{g}). \quad (1.6)$$

The hydraulic analogy between viscous fluid motion in a porous medium and motion in a Hele-Shaw cell is rigorous for isothermal flow when an equivalent permeability $K = d^2/12\mu$ is defined [17; 26]. The Hele-Shaw cell is very useful because its geometry forces the disturbances to be purely two-dimensional. In the case of porous media the critical Rayleigh number is known to be $Ra_c = 4\pi^2$, as it has been derived analytically by Horton and Rogers [27] and experimentally shown by Lapwood [28]. The appearance of time dependent motion in a porous layer uniformly heated from below was suggested from experiments by Caltagirone *et al.* [29], and then Horne and O'Sullivan [30] numerically verified the existence of both stationary and oscillatory motions. Cherkaoui and Wilcock [31] numerically determined a sequence of transitions in an open-top square porous layer heated from below: stationary - quasi-periodic - periodic. In the same way, the analysis of time dependent Hele-Shaw convection [32; 33; 34] showed that the transition from the steady state to the chaotic state is preceded by the onset of periodic and then quasi-periodic oscillations, similar to the behavior of convection in a thin horizontal fluid layer.

1.3 Synchronization

Chaos synchronization is an important piece of research in non linear dynamics due to its potential applications in engineering and in the understanding of complicated phenomena in nature. Different kinds of synchronization have been defined: complete synchronization (CS) [10; 35; 36], generalized synchronization (GS) [37; 38], phase synchronization (PS)[39; 40; 41; 42], and lag synchronization (LS) [43]. CS means that the several coupled systems remain in step with each other in the course of time. It is obvious that CS is the simplest and strongest form among the diverse

synchronization behaviors. Only in coupled systems with identical elements can we observe CS. In the GS the dynamical variables from one subsystem are function of the variables of the other subsystem. In the classical case of periodic self-sustained oscillators, described as early as in [4], synchronization is usually defined as locking of the phases, while the amplitude can be quite different. However, PS is not restricted to periodic oscillators. Reference [40] shows that interaction of nonidentical autonomous chaotic oscillators leads to a perfect locking of their phases, whereas their amplitudes remain chaotic and uncorrelated. LS is an intermediate state between PS and CS. It appears as a coincidence of shifted in time states of two systems. Reference [43] shows transition from PS to CS, passing for LS, increasing the coupling between two nonidentical chaotic oscillators. Different regimes of synchronization can be found in the review article by Boccaletti [5].

In view of the future results, we give some more information about the complete synchronization.

1.3.1 Complete synchronization

For chaotic dynamics, synchronization influences not only the mean frequencies but also the chaotic amplitudes. As a result, the signals coincide (or nearly coincide).

Let us consider the temporal evolution of two identical chaotic systems:

$$\begin{aligned}\dot{\mathbf{x}} &= \mathbf{f}(\mathbf{x}), \\ \dot{\mathbf{y}} &= \mathbf{f}(\mathbf{y}),\end{aligned}\tag{1.7}$$

where \mathbf{x} and \mathbf{y} represent the N -dimensional state vectors of the systems, while \mathbf{f} is a vector field $\mathbf{f} : R^n \rightarrow R^n$. As the dynamics of each variable is chaotic, in the case of non interacting systems one sees two independent random-like processes without any mutual correlation. Obviously, there is not a unique way to couple. However, we are looking for a contractive coupling that tends to make the differences $|\mathbf{x} - \mathbf{y}|$ smaller and does not affect the symmetric synchronous state $\mathbf{x} = \mathbf{y}$. Therefore, we demand that the coupling force were proportional to the differences of the state of the two systems and vanishes for coinciding state.

A bidirectional coupling scheme is obtained by introducing the following

additional dissipation term:

$$\begin{aligned}\dot{\mathbf{x}} &= \mathbf{f}(\mathbf{x}) + \mathbf{C} \cdot (\mathbf{y} - \mathbf{x}) \\ \dot{\mathbf{y}} &= \mathbf{f}(\mathbf{y}) + \mathbf{C} \cdot (\mathbf{x} - \mathbf{y})\end{aligned}\quad (1.8)$$

where \mathbf{C} is a $n \times n$ matrix, whose coefficients rule the dissipative coupling. If there is no coupling the two systems are completely independent and uncorrelated; with small coupling the trajectory of the signals will move closer due to the attraction between the two states. If the coupling is strong enough the attraction wins and eventually it leads to a complete synchronized state.

However, we have to pay special attention to how strong is the coupling, for example, if we consider two oscillators that are mechanically coupled with a rigid link, we can not speak of synchronization because the coupling imposes a too strong limitation on the motion of the two systems. To determine what can be considered as a weak or a strong coupling is rather subtle, but we can say that the introduction of coupling should not qualitatively change the behavior of the interacting systems.

1.4 The scope of this work

This thesis is a contribution to the theoretical analysis of possible synchronization mechanisms between two convective Hele-Shaw cells. The objective requires to calculate the evolution of the flow and heat transport patterns in a single Hele-Shaw cell uniformly heated from below. The first numerical approach, has been supported by a linear and weakly non linear stability analysis of the model. Synchronization is investigated using a thermal bidirectional coupling in stationary, periodic and chaotic dynamical regimes. Different numerical methods have been implemented to optimize the computational speed. The minimal number of connectors has been established to prepare favorable conditions for future experimental realizations.

The mathematical formulation of the model of the flow in a Hele-Shaw cell is given in Chapter 2. The configuration, which we have modelled consists in a rectangular parallelepiped of width and height h and thickness $d \ll h$. The vertical boundaries are considered adiabatic. The horizontal top and bottom are isothermal, with the bottom surface hotter than the top

one. When there is no motion, a vertical linear temperature distribution is set in the system.

In chapter 3, we will analyze the dynamics of a single Hele-Shaw cell. Two type of transition are characterized: the first one is a decrease in the horizontal aspect ratio of the cells; the second one is from steady to unsteady flow pattern. Due to the simple geometry of the Hele-Shaw cell, this thesis starts with a simple numerical scheme: a second order finite difference scheme. We give the transitional Rayleigh numbers that separate the different dynamical regimes and describe the characteristics of the convective patterns after each transition.

In chapter 4, linear and non linear analysis of the conductive state is presented. The linear analysis permits to determine the stability threshold. The non linear evolution is described by the amplitude of the unstable modes. In order to solve the linear and non linear problem, we implement the spatial collocation method which is computationally more efficient than the finite difference scheme.

In chapter 5, after a brief discussion over what determines the spatial structures of the flow, we investigate possible synchronization mechanisms between two Hele-Shaw cells. Using a weak bidirectional thermal coupling between all the points of the two systems, we obtain complete coincidence of the dynamics. We also investigate the minimal number of points necessary to get synchronization and we also consider the possibility of coupling both systems only through the lateral walls.

We conclude with chapter 6 by summarizing the main results.

In general, there is no analytical tools available for solving nonlinear complicated PDE. Therefore, in Appendices A and B, we have recalled the numerical techniques that permit to calculate the time evolution of the flow inside the Hele-Shaw cell. In order to integrate the flow during a long period of time, we propose a set of numerical methods, which permit to compute in an accurate and stable way the time evolution of the system. In Appendix A, we discuss the discretization of initial-value problems and boundary value problems, considering, more specifically the advection-diffusion equations and the Poisson equation. One-step and multistep methods are considered for explicit and implicit schemes, paying special attention to the accuracy and stability of discretization. In Appendix B, we introduce spectral methods, making evident their advantages in term of convergence, but also their complexity in term of implementation.

Chapter 2

Mathematical Formulation

Two dimensional systems are in general more amenable to experiments and simulations than three dimensional systems, mainly because the reduction of the dimension significantly reduces the amount of data required to specify the flow. Flow in third dimension can be suppressed through rotation, stable density gradients, magnetic field or thinness of a fluid layer, as in the present work. In this chapter, we deduce the equations which model 2D convection in Hele-Shaw cell, a cell that is very thin compared to its horizontal width and vertical height. In this way the three dimensional Navier-Stokes equations can be reduced to two dimensional equations. This task is obtained following the procedure exposed in Bizon *et al.* [44; 45]. Finally, stream function formulation of the governing equations allows us to make evident the analogy between flows in porous medium and in a Hele-shaw cell.

2.1 Model equations

The geometry which we consider is a rectangular parallelepiped of width and height h in direction x and y , and thickness $d \ll h$ in the z direction. The fluid in the cell is buoyantly driven by a vertical gradient of temperature which ranges from $T = T_b$ at $y = 0$ (the bottom of the cell) to $T = T_t$ at $y = h$ (the top of the cell). To model the fluid motion, we start with the

Navier-Stokes equations in the Boussinesq approximation:

$$\nabla \cdot \mathbf{v} = 0 \quad (2.1)$$

$$\partial_t T + \mathbf{v} \cdot \nabla T = \kappa \nabla^2 T \quad (2.2)$$

$$\partial_t \mathbf{v} + (\mathbf{v} \cdot \nabla) \mathbf{v} = \nu \nabla^2 \mathbf{v} - \frac{1}{\rho_0} \nabla p + \mathbf{g} \frac{\rho_f}{\rho_0} \quad (2.3)$$

where \mathbf{v} , p , ρ and T are the velocity, pressure, density and temperature of the fluid. The parameters ν and κ are the kinematic viscosity and the thermal diffusivity, respectively. Gravity \mathbf{g} is directed downward, in the y direction. Boussinesq approximation consists of setting constant all the physical properties of the medium, except the one that is involved in the buoyancy term. The equation of state of an isothermal fluid, in the most general form, is

$$\rho_f = \rho_f(T, p). \quad (2.4)$$

We suppose that the temperature and the pressure are sufficiently small with respect to their reference values, in order to write

$$\rho_f = \rho_0 [1 - \alpha(T - T_0)] - \beta(p - p_0) \quad (2.5)$$

where T_0 and p_0 are the temperature and the pressure of reference, α is the thermal expansion coefficient and β is the compression coefficient. Furthermore, if we suppose that the perturbations of the mass due to the variations of the pressure are small with respect the variations of temperature, the relation (2.5) becomes

$$\rho_f = \rho_0 [1 - \alpha(T - T_0)]. \quad (2.6)$$

Because d is much smaller than h , the flow parallel to the side walls may be turbulent, while the crosswise Reynolds number, ud/ν , is no larger than order ten. Here \mathbf{u} refers to either x and y components of the velocity. This allows to assume, for such flows, a parabolic profile [46; 47; 48] in z as

$$\mathbf{v}(x, y, z, t) = f(z) \mathbf{u}(x, y, t) \quad (2.7)$$

where

$$f(z) = 4 \frac{z}{d} \left(1 - \frac{z}{d}\right), \quad \mathbf{u} \cdot \hat{\mathbf{e}}_z = 0, \quad (2.8)$$

$\hat{\mathbf{e}}_z$ is the unit vector in the z direction and \mathbf{u} lies in the (x, y) plane. Hence, the temperature and the pressure may be considered independent of z [44].

Inserting this profile in (2.1)-(2.3) and averaging in the z direction, the Eqs. (2.1)-(2.3) become:

$$\begin{aligned} \int_0^d f(\nabla_{\perp} \cdot \mathbf{u}) dz &= 0 \\ \int_0^d \partial_t T + f(\mathbf{u} \cdot \nabla_{\perp}) T - \kappa \nabla^2 T dz &= 0 \\ \int_0^d f \partial_t \mathbf{u} + f^2 (\mathbf{u} \cdot \nabla_{\perp}) \mathbf{u} - \nu f \nabla_{\perp} \mathbf{u} - \nu \partial_y^2 f \mathbf{u} + \frac{\nabla_{\perp} p}{\rho_0} - \mathbf{g} \frac{\rho_f}{\rho_0} dz &= 0 \end{aligned}$$

that is

$$\begin{aligned} \nabla_{\perp} \cdot \mathbf{u} &= 0 \\ \partial_t T + \frac{2}{3} \mathbf{u} \cdot \nabla_{\perp} T &= \kappa \nabla_{\perp}^2 T \\ \partial_t \mathbf{u} + \frac{4}{5} (\mathbf{u} \cdot \nabla_{\perp}) \mathbf{u} &= \nu [\nabla_{\perp}^2 - \frac{12}{d^2}] \mathbf{u} - \frac{\nabla_{\perp} p}{\rho_0} + \mathbf{g} \frac{\rho_f}{\rho_0}. \end{aligned} \quad (2.9)$$

Here the subscript \perp refers to the (x, y) plane. In order to generate dimensionless variables (that are of order one in the flow fields), we scale with respect to the new variables:

$$\begin{aligned} \tilde{t} &= \frac{h^2}{\kappa} t, \\ \tilde{\mathbf{x}} &= \frac{\mathbf{x}}{h}, \\ \tilde{\mathbf{u}} &= \frac{h}{\kappa} \mathbf{u}, \\ \tilde{p} &= \mu \frac{\kappa}{h^2} p, \\ \tilde{T} &= \frac{T}{\Delta T}. \end{aligned} \quad (2.10)$$

where $\Delta T = T_b - T_t$. The proper scales depend on the nature of the flow and are obtained equating the terms that are dominant in the flow field. In particular, at low Rayleigh number the dominant terms are the pressure

and the viscous forces. Thus, our model 2D system results:

$$\nabla_{\perp} \cdot \mathbf{u} = 0, \quad (2.11)$$

$$\partial_t T + \frac{2}{3} \mathbf{u} \cdot \nabla_{\perp} T = \nabla_{\perp}^2 T, \quad (2.12)$$

$$\begin{aligned} \frac{1}{Pr} \left(\partial_t \mathbf{u} + \frac{4}{5} (\mathbf{u} \cdot \nabla_{\perp}) \mathbf{u} \right) &= [\nabla_{\perp}^2 - \frac{12h^2}{d^2}] \mathbf{u} - \nabla_{\perp} p + \\ &+ \frac{[1 - \alpha \Delta T(T - T_0)]}{\nu \kappa} h^3 \mathbf{g}, \end{aligned} \quad (2.13)$$

where $Pr = \nu/\kappa$ is the Prandtl number. Apart from numerical factors, the difference between these equations and the two dimensional Boussinesq equation is the extra dissipation term proportional to h^2/d^2 . Now, because the scale of flow structures is larger than d , the $\nabla_{\perp}^2 \mathbf{u}$ term is outweighed by this linear Hele-Shaw drag term. Furthermore, for large Prandtl number equations (2.11)-(2.13) become

$$\mathbf{u} = \frac{d^2}{12h^2} \left(-\nabla_{\perp} p + \frac{[1 - \alpha \Delta T(t - T_0)]}{\nu \kappa} h^3 \mathbf{g} \right) \quad (2.14)$$

$$\partial_t T + \mathbf{u} \cdot \nabla_{\perp} = \nabla_{\perp}^2 T \quad (2.15)$$

$$\nabla \cdot \mathbf{v} = 0 \quad (2.16)$$

2.1.1 Stream function equation reformulation

As an alternative way of solving the governing equations in primitive variables, it is possible to avoid the explicit appearance of the pressure term by using the stream function formulation. In two dimensions the Eqs. (2.14)-(2.16) are:

$$\frac{\partial u_x}{\partial x} + \frac{\partial u_y}{\partial y} = 0, \quad (2.17)$$

$$\frac{\partial p}{\partial x} + 12 \frac{h^2}{d^2} u_x = 0, \quad (2.18)$$

$$-\frac{[1 - \alpha \Delta(T - T_0)]}{\nu \kappa} h^3 g + \frac{\partial p}{\partial y} + 12 \frac{h^2}{d^2} u_y = 0, \quad (2.19)$$

$$\frac{\partial T}{\partial t} + u_x \frac{\partial T}{\partial x} + u_y \frac{\partial T}{\partial y} = \left(\frac{\partial^2 T}{\partial x^2} + \frac{\partial^2 T}{\partial y^2} \right). \quad (2.20)$$

In order to remove the pressure variable, we derive Eq. (2.19) with respect to x and subtract the derivative of Eq. (2.18) with respect to y . The resulting equation is:

$$12 \frac{h^2}{d^2} \left(\frac{\partial u_y}{\partial x} - \frac{\partial u_x}{\partial y} \right) - \frac{\alpha g \Delta T h^3}{\nu \kappa} \frac{\partial T}{\partial x} = 0. \quad (2.21)$$

Being $u_z = 0$, the governing equations can be presented in terms of a stream function defined by:

$$u_x = \frac{\partial \psi}{\partial y} \quad ; \quad u_y = -\frac{\partial \psi}{\partial x}. \quad (2.22)$$

Using the stream-function formulation the equations (2.20) and (2.21) become:

$$\begin{aligned} \frac{\partial T}{\partial t} &= \nabla^2 T - \frac{\partial \psi}{\partial y} \frac{\partial T}{\partial x} + \frac{\partial \psi}{\partial x} \frac{\partial T}{\partial y} \\ \nabla^2 \psi &= -Ra \frac{\partial T}{\partial x} \end{aligned} \quad (2.23)$$

where

$$Ra = \frac{\alpha g \Delta T h d^2}{12 \nu \kappa} \quad (2.24)$$

is the Hele-Shaw Rayleigh number. For a square bounded porous medium, the linear theory gives a Rayleigh number equals to $4\pi^2$ for the onset of convection (Lapwood [28]) and it is defined as

$$Ra^{PM} = \frac{g \alpha \Delta T h K}{\nu \kappa} \quad (2.25)$$

where κ is the thermal diffusivity of the fluid-filled medium, K is the permeability of the medium, α is the coefficient of thermal expansion of the fluid, ν is the kinematic viscosity of the fluid and h is the height of the square porous medium. A comparison of (2.24) and (2.25) reveals that the Hele-Shaw Rayleigh number is identical to the porous medium Rayleigh number if the permeability is taken to be

$$K = \frac{d^2}{12}. \quad (2.26)$$

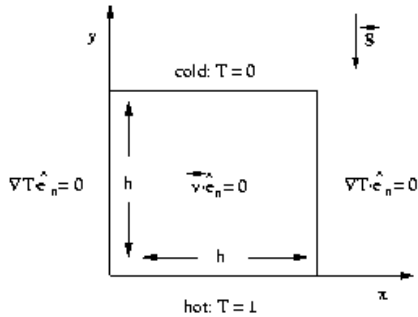


Figure 2.1: Schematic representation of an Hele-Shaw cell heated from below.

As indicated before, the Hele-Shaw cell is represented by a rectangular parallelepiped of width and height h in directions x and y , and thickness d in the z direction. As all boundaries are rigid the flow must follow the impermeability conditions that is, $\mathbf{v} \cdot \hat{\mathbf{e}}_n = 0$ on the boundaries, where $\hat{\mathbf{e}}_n = 0$ is the unit vector normal to the boundary. The temperature boundary conditions are $T = 1$ at $y = 0$, $T = 0$ at $y = h$ and $\nabla T \cdot \hat{\mathbf{e}}_n = 0$ at the lateral walls (insulating conditions), (see Fig. 2.1). The first equation of (2.23), is a diffusion equation for the temperature field. The non linear term is usually called *advection* term and takes the form of a Jacobian. The second equation is of Poisson type and is written for the stream function. The boundary conditions for the stream function are $\psi = 0$ on all solid boundaries and express the impermeability of the walls.

Chapter 3

From Stationary Convection to Chaos

In this section we will illustrate that a fluid layer when heated from below may exhibit several behaviors: stationary convection, oscillating convection, formation of thermal plumes, chaotic convection, and turbulence. Experimental investigations of Caltagirone *et al.* (1971) [29], for two-dimensional flow in porous media uniformly heated from below, showed irregular fluctuations. The experimental analysis of Koster (1980) [33] of time dependent convection in a thin vertical fluid layer, demonstrated that the transition from steady to chaotic state is preceded by the onset of periodic, and then quasi-periodic oscillations. Horne and O'Sullivan (1974) [30] modelled the experiment of Caltagirone and proved that, in certain case, two distinct modes of flow were possible, one of which was oscillating, the other being steady. Koster (1981) [32] and Frick (1983) [34] gave numerical support to the oscillatory convection in the Hele-Shaw cell. Kimura *et al.* (1986-87) [49; 50], with simulations of an initial value problem for convection in porous medium, explained the route to chaos through the following temporal sequence: steady, periodic, quasi-periodic, and another final periodic regime. They found two chaotic states at $Ra = 1000$. Graham and Steen (1994) [51] showed that it was an artefact due to the insufficient spatial resolution of the numerical discretization and that chaotic behavior appeared only at $Ra = 1200$.

In this chapter, we present the dynamics of a single square Hele-Shaw cell heated from below. The Rayleigh number is varied from 44, (10% above its critical value), until 1200. The first numerical method used to solve

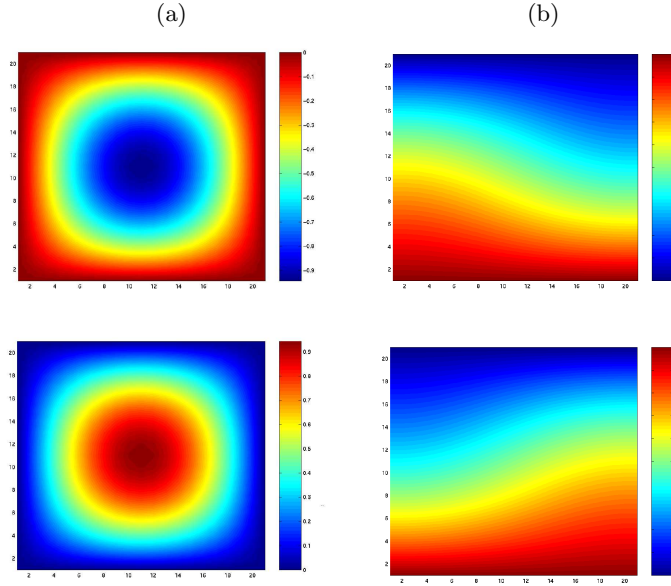


Figure 3.1: Stationary convection at $\text{Ra}=44$. (a) The spatial pattern preferred by the flow is a uni-cellular mode (stream-function) for the two possible rotation i.e. clockwise (upper) and counterclockwise (lower) (b) The snapshots of the corresponding temperature field.

equations (2.23) is a simple second order accurate finite difference scheme. A square uniform ($\Delta x = \Delta y$) grid of 129×129 points has been used. In order to avoid aliasing errors, the advection term is treated with a second order Arakawa Jacobian [52; 53; 54]. Time integration is achieved with an Adams-Bashforth method. Details about the numerical method are reported in Appendix A.

3.1 Results of numerical simulations

The onset of convection is defined when the parallel fringe pattern of the state of pure heat conduction is slightly deformed to a wavy shape, indicating the appearance of a vertical flow component rising upward along one of the two vertical walls. At low Rayleigh number, $\text{Ra} = 44$, the convective

flow begins in the most favorable mode for that value, that consists of a roll with its axis parallel to the shorter side of the box, namely the uni-cellular mode. The single roll can turn clockwise or counterclockwise depending on the initial condition. In a single cell, the fluid is swept horizontally toward the lateral boundary. Due to buoyancy it rises and eventually impacts the upper boundary layer in the corner where the side wall meets the upper surface of the cell. In this way the fluid carries heat flux away from the hot boundary layer. In that corner the fluid is redirected horizontally, subsequently it becomes a dominant part of the fluctuation which sweeps along the upper boundary layer, exchanging heat flux directly with the sheared, cold boundary layer. The heavier fluid goes down and meets with the lower hot boundary layer where the colder heat flux diffuses. Note that this scenario does not involve the central region of the cell in any way. It is remarkable that after the convection is fully developed the sense of rotation of the roll remains invariant, independent of the heating rate (until we observe transitions to new states).

Snapshots of the stream function and temperature for the solution at $Ra = 44$ are shown in Fig. 3.1.

At variance at high Rayleigh numbers, converged solutions display a multi-cellular convective pattern. Starting from $Ra = 350$, it exist two distinct possible modes of flow, one of which is time dependent (single cell mode), the other being steady with a three-cellular mode. The boundary layer becomes unstable and new upwelling sites develop. Starting from a single roll it is possible to see a continuous development of three weak circulations inside the primary convective roll. By further increasing of the heating, such circulations grow, and the flows continuously transform into a three-roll flow. This transition brings the system from a steady one-cell pattern to a steady three-cell pattern.

The aim of this investigation is to consider the possible synchronization between two chaotic Hele-Shaw cells. By increasing slowly the Rayleigh number it is possible to bring the uni-cellular convective cell into a chaotic state. This dynamical regime is preferred in view of the subsequent study of synchronization. The multi-cellular modes are in general stationary at low Rayleigh number and therefore not interesting from the point of view of dynamical systems. By increasing the Rayleigh number, we have to be careful to keep the system onto the single cell mode of convection because this solution maybe unstable with respect to the multi-cellular modes. This

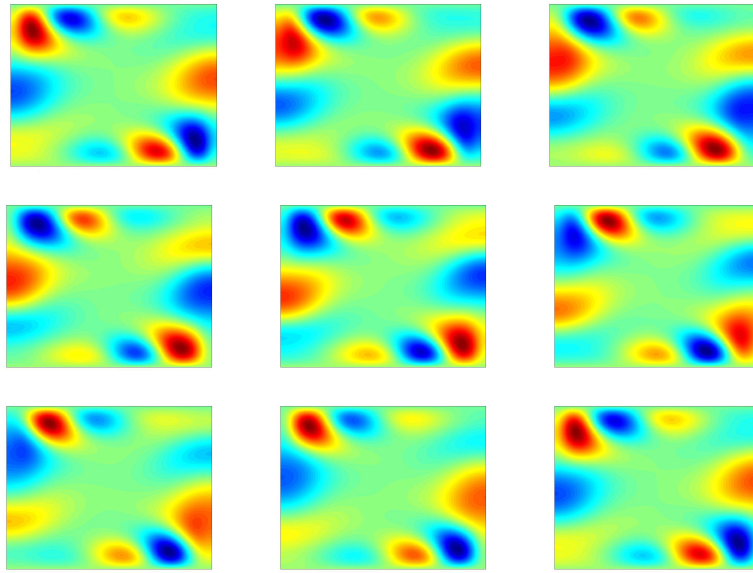


Figure 3.2: Snapshots of the instantaneous temperature fluctuation from the main field at $Ra = 400$, showing wave number equal to 5. Wave number is computed as one-half the number of sign changes in the fluctuation field around the perimeter of the container. Time is increasing from left to right and from top to bottom. First snapshot is for $t = 0.1498$. Sampling time is $\Delta t = 0.0014$. For this Rayleigh number the dimensionless period is $\tau_p = 0.01183$.

task proved to be delicate. The mode selection depends from the history of heating. Indeed, uni-cellular structure can be permanently maintained in the range that we have studied by a slow and controlled increase of the heating. Starting with the uni-cellular solution at $Ra = 44$, we drive the flow to remain into this mode by increasing the Rayleigh number only by small increments. Hence, we force the solution into the uni-cellular mode which becomes unsteady for Rayleigh number larger than approximately 350. The possibility of imposing the spatial patterns in the experimental solutions is due to Horne and O'Sullivan [30]. In general a very rapid heating introduces multi-cellular modes (stationary). Because we have multistability of modes, we will refer to the most favorable mode, not to the

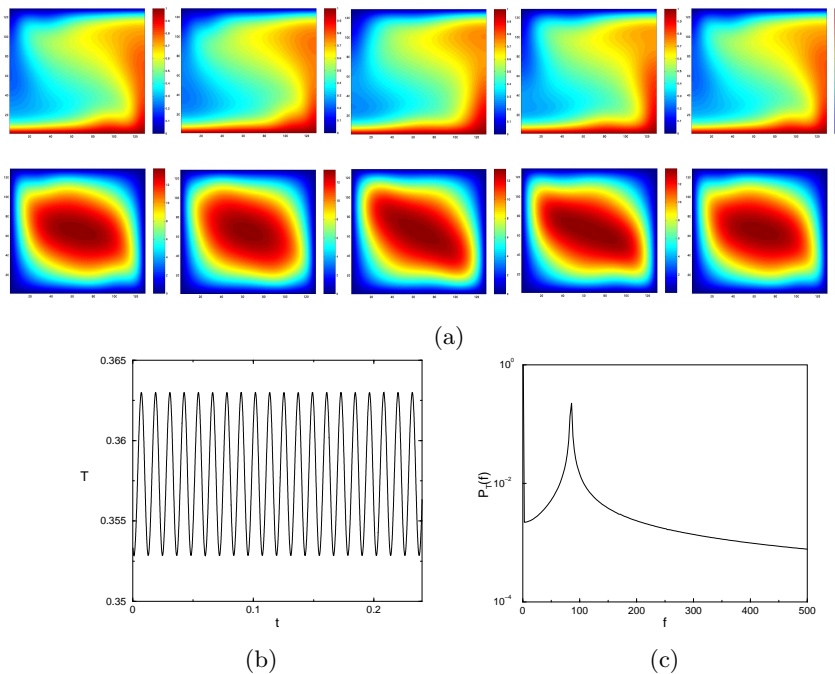


Figure 3.3: Temporal characteristics of convection at $Ra = 400$. (a) Evolution of the temperature and the stream function over one oscillatory period. Time proceeds from left to right and it is increased from $t = 0.2$ with time interval $\Delta t = 0.0029$. The period in dimensionless units is $\tau_p = 0.01183$. (b) Temperature as function of time at point $(x = 1/3, y = 1/3)$. (c) Power spectrum of the temperature signal shown in (b) is plotted in log-linear scale. Only one fundamental frequency $f_5 = 84.53$ is observed.

most stable. At this point of the exposition, we need only information about the dynamics of the uni-cellular solution. We deal with its stability analysis in the following chapter.

For $Ra = 386.35$ regular oscillations appear. We fix $Ra = 400$ and measure the dimensionless period τ_p . The nature of the disturbance that generates the oscillations is a travelling wave pattern of five pairs of alternating warm and cold blobs swept around the box [55]. The latter can be identify counting the number of extrema in one half of the box, as shown in Fig. 3.2. The physical explanation of the instability is that as the Rayleigh number increases, the flow gets stronger, bringing cold fluid close to the warm boundary and vice versa. The destabilizing mechanism is the same as it occurs at the convection onset. Now, the difference is that a flow already exists. The resulting flow is the sum of a steady mean component and a fluctuation with travelling wave structure. The evolution of the solution through a single oscillation period is illustrated in Fig. 3.3(a). The sequence is of five isothermal and five streamline plots evenly spaced in time ($\tau_p/4$). The numerical simulation is characterized by one prevailing frequency, $f_5 = 84.5308$. The power spectrum, defined as the squared modulus of the Fourier transform of the temperature is plotted on log linear scale and is characteristic of a single periodic regime, (see Fig. 3.3(c)). The convective system departs from this single periodic state at $Ra = 505$ when a second fundamental frequency, incommensurate with the first one, appears in the power spectrum. The competing stationary solution has now a four cellular spatial mode. A close look at the Poincaré section [56], Fig. 3.4(c) for $Ra = 520$, suggests a quasi-periodic dynamics. Starting from the time series of the temperature we construct the Poincaré section by plotting the sequence of time intervals between successive maxima (Δt_{n+1} vs Δt_n). The advantage of the Poincaré section is that it permits to visualize the organization of the trajectory in the phase space. Fig. 3.4(c) shows that the phase trajectory is inscribed on a torus T^2 . The lowest and strongest frequency is $f = 27.86$. The frequency of the $n = 5$ unstable periodic state is $f_5 = 104.37$, as shown in Fig. 3.4(b). In order to know what frequency refer to which particular spatial mode, we have made use of a stroboscopic technique. The name comes from the well-known optical devices that measure the frequency of oscillation (or rotation) of mechanical objects by shining a bright light at periodic intervals, so that the object appears stationary if the frequency of light flashes is equal to the frequency

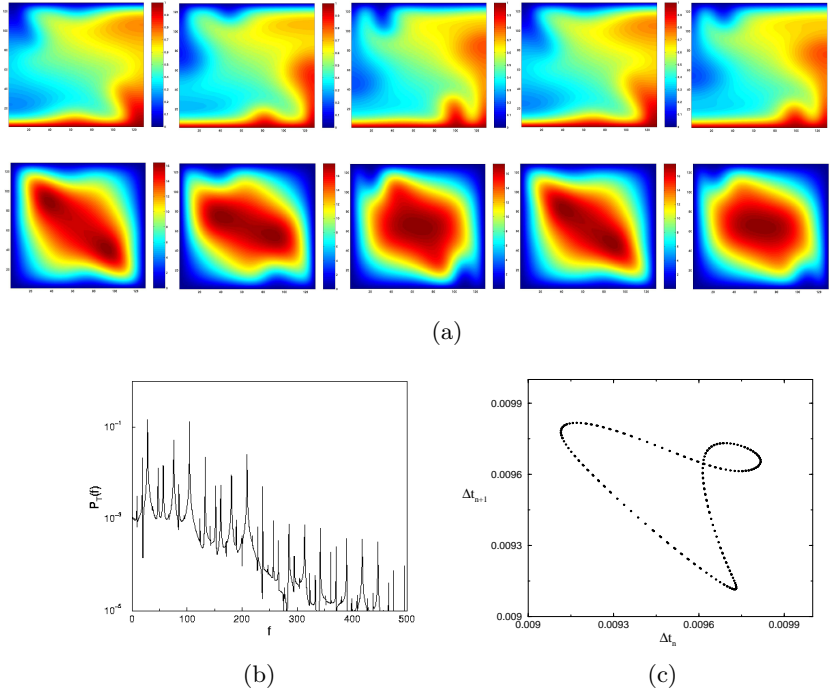


Figure 3.4: (a) Snapshots of temperature and stream function for the solution at $Ra = 520$. For this value of the Rayleigh number, thermal plumes appears for the first time. They are swept horizontally in the lower boundary layer to rise along the right lateral wall by buoyancy. Time is going from $t = 0.4149$ to $t = 0.5189$. The time interval between successive snapshots is $\Delta t = 0.026$. (b) The spectrum of the temperature signal taken at the point $(x = 1/3, y = 1/3)$ shows a quasi-periodic behavior: $f_5 = 104.37$ is the limit cycle frequency and $f = 27.87$ is the second frequency that appears at the secondary bifurcation. (c) The Poincaré section displays the typical "eight" of a quasi-periodic state.

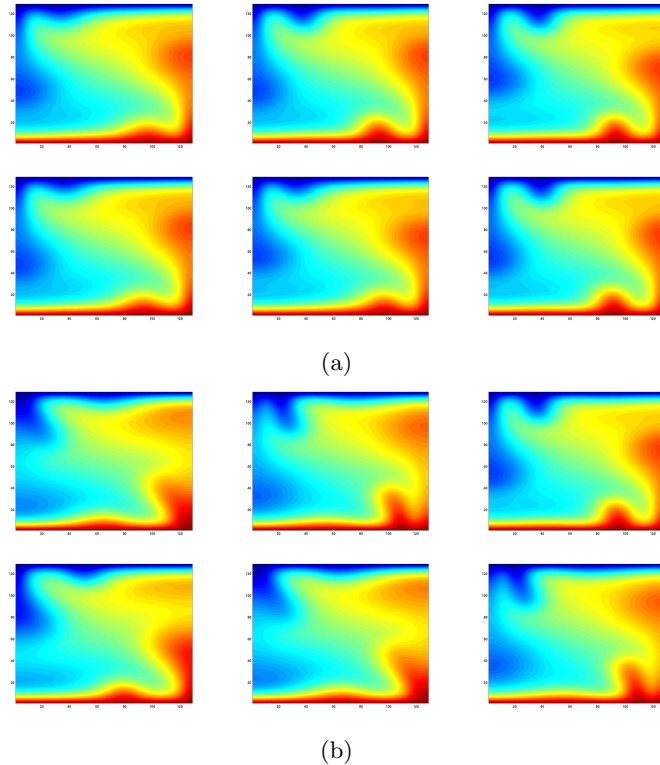


Figure 3.5: (a) Snapshots of the temperature fixing f_5 . Snapshots are separated by time intervals $\Delta t = 0.009$ ($1/f_5$). (b) snapshots of the temperature fixing f , the time interval between each picture is $\Delta t = 0.036$ ($1/f$).

of the moving object. If the frequencies are slightly different, the object appears to be slowly oscillating (or rotating). Figures 3.5 have been obtained using this stroboscopic technique. Starting from the temporal signal of the temperature taken at the point $(x, y) = (1/3, 1/3)$, we take snapshots of the temperature field separated by time interval $\Delta t = 1/f_5$, as shown in Fig. 3.5(a). Analyzing the evolution of the photographs, we understand that the lowest frequency (f) is the frequency related to the vertical movement of the plume in the boundary layer. In the same way, we discover that f_5 is the frequency of the $n = 5$ travelling wave.

Numerical analysis permits to identify that the most dangerous pertur-

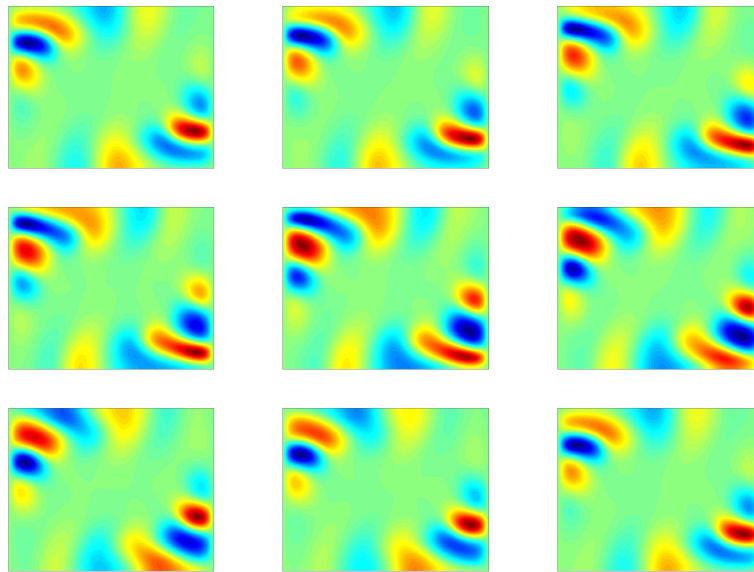


Figure 3.6: Snapshots of the instantaneous temperature fluctuation field at $Ra = 600$, showing a travelling wave with wave number equal to 7. The wave number is equal to one half of the number of sign changes in the fluctuation field around the perimeter of the container. Time is increased from $t = 0.149$ (upper-left) to $t = 0.155$ (bottom-right), with time interval $\Delta t = 0.00075$.

bation for this quasi-periodic state, is a travelling wave with wave number $n = 7$. This travelling wave is the responsible of a new periodic regime starting at $Ra = 560$, as shown in Fig. 3.6. Figure 3.7 shows the evolution of the frequency spectra for Rayleigh numbers in the range [505, 560]. At $Ra = 505$, the frequency f_5 prevails with its harmonics. At $Ra = 510$, the frequency $f + f_5$ appears. From $Ra = 520$ to $Ra = 540$ the two frequencies (f_5, f) and their harmonics are more and more pronounced. At $Ra = 560$ the spectrum is characteristic of a single periodic dynamics with frequency $f + f_5 = f_7$ and its harmonics. Thus, the frequency f_5 is the primary limit cycle frequency and f_7 is the secondary frequency that arises at the secondary bifurcation. The quasi-periodic regime is the result of the non linear interaction between the steady state and two periodic fluctuations with different wave numbers.

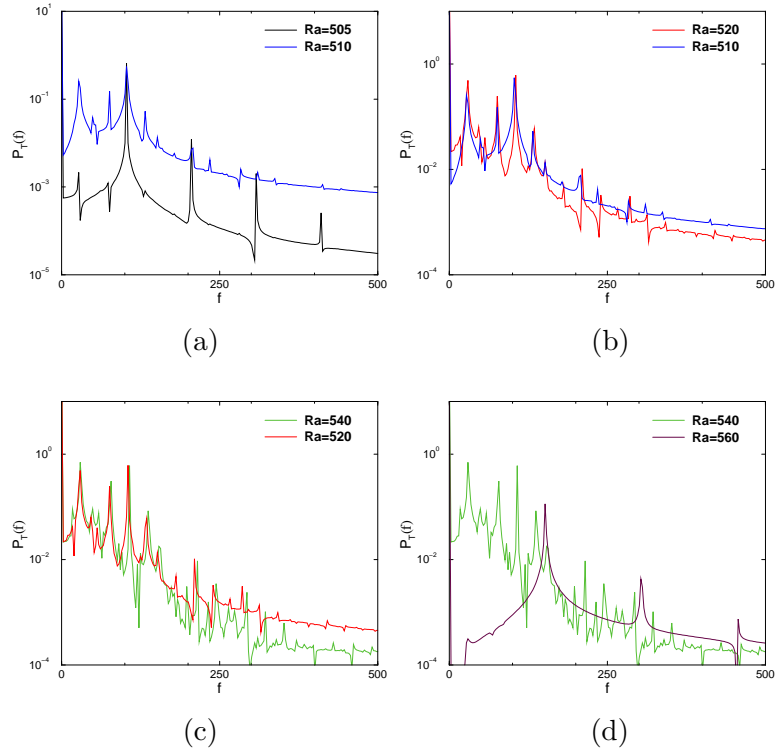


Figure 3.7: Evolution of frequency spectra for $Ra \in [505, 560]$. (a) At $Ra = 505$, f_5 is dominant and f is just formed on the left side. At $Ra = 510$, f has increased and two new frequencies appear on both sides of f_5 . They are identified as $f_5 - f$ and $f_5 + f$. (b) and (c) between 520 and 550 the harmonics of f_5 and f become more marked. (d) At $Ra = 560$ all frequencies vanish, except $f_5 + f$ and its harmonics. The nature of the disturbance at $Ra = 560$ is a travelling wave with a wave number $n = 7$.

Many qualitatively changes are observed in the spatial structure associated with the quasi-periodic state. The flow patterns are characterized by the appearance of a vertical portion of flow in the middle of the lower boundary. This portion of hotter fluid, initially infinitesimal, grows while is swept horizontally by the mean flow. By buoyancy, it rises along the side wall, but the rise is not uniform as in the periodic case, see Fig. 3.4(a) and 3.5. The flow breaks, creating a new particle of hot fluid which continues to rise upward alone. At this Rayleigh number we can observe, for the first time, the formation of the so-called thermal plumes. As an operational definition, we say that a plume is formed when an isotherm in the boundary layer is buckled. In other words, a plume is formed when some portion of fluid becomes nearly vertical (away from the downstream corner). In the quasi-periodic regime, no plumes are identical. The horizontal position of each plume is shifted, so with each plume formation, the cycle differs slightly in position relative to each other: each plume forms slightly upstream or downstream of the main position of formation. This process occurs in the following way: a fluctuation in the bottom boundary layer causes a plume to form just a little bit earlier, causing a horizontal compression of the wave train (and vertical expansion). This leads to two plumes being slightly closer to each other than they would otherwise be. These two plumes together do a more efficient function of removing heat of the boundary layer than usual. This leads to a little longer induction time for the next plume to form, a larger interval between plumes and a slightly worse job of cleaning out the boundary layer. Thus the next plume forms a little earlier and the flow develops a phase-modulated train of disturbance. For $Ra = 560$, the solution turns back to a simply periodic regime. As shown in Fig. 3.6, the nature of the perturbation is a periodic oscillation with wave number $n = 7$, i.e. 14 blobs turning around the perimeter of the container are identified. The key element is always the formation of thermal plumes, which changes as Ra increases. At $Ra = 520$, the plumes are created around the middle of the bottom boundary layer. They are small and grow more in width than in height as they are convected across the horizontal layer. At $Ra = 900$, the plumes start closer to the left lateral boundary with greater strength. They are narrow and expand vertically. The periodic state is now a travelling wave with $n = 11$, as shown in Fig. 3.8. Figure 3.9(a) shows the evolution of the thermal plumes and stream function over one oscillatory cycle, at $Ra = 900$. The competing stationary solution has now a two rolls pattern

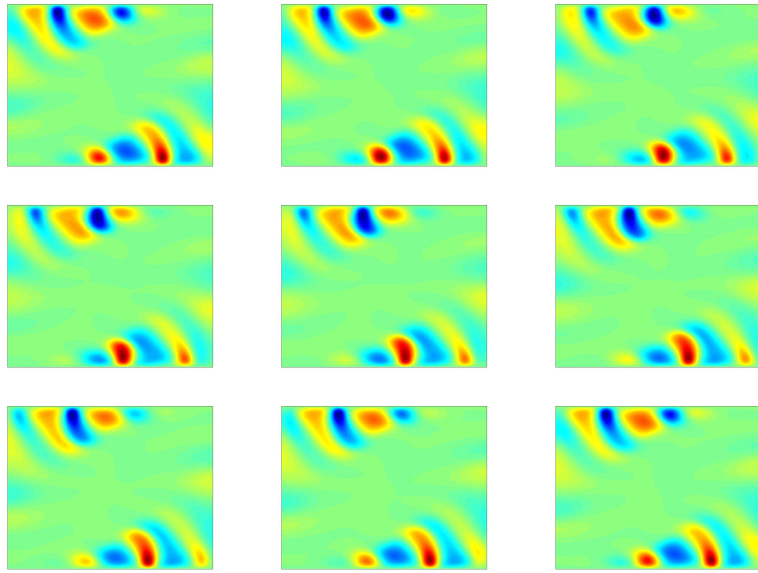


Figure 3.8: Snapshots of the instantaneous temperature fluctuation extracted from the main field at $Ra = 900$, showing a wave number equal to 11. Time is evenly distributed from $t = 0.2$ (upper-left) to $t = 0.202$ (bottom-right).

organization. Every plume is identical after applying a time shift. The period, in dimensionless units, is equal to 0.00273. The power spectrum of the temperature displays a single frequency, $f_{11} = 365.21$, as shown in Fig. 3.9. The Poincaré section is very simple as it reduces to a simple point, (see Fig. 3.9(c)). Starting from $Ra = 950$, the quasi-periodic scenario repeats again. Travelling waves interact in the same way as described above, but this time ending up in a new regime. At $Ra = 1200$, the amplitude of the variations in the heat transport reaches its maximum value and a strong broad band noise appears in the power spectrum, which is a characteristic of non-periodic motion, as shown in Fig. 3.10(b). Exponential decay in the power spectra at high frequency is expected for bounded smooth deterministic dynamics [57; 58]. The Poincaré section shows a very large number of scattered points, as displayed in Fig. 3.10(c). The convective regime is now chaotic. Qualitatively, however, the flow patterns appear

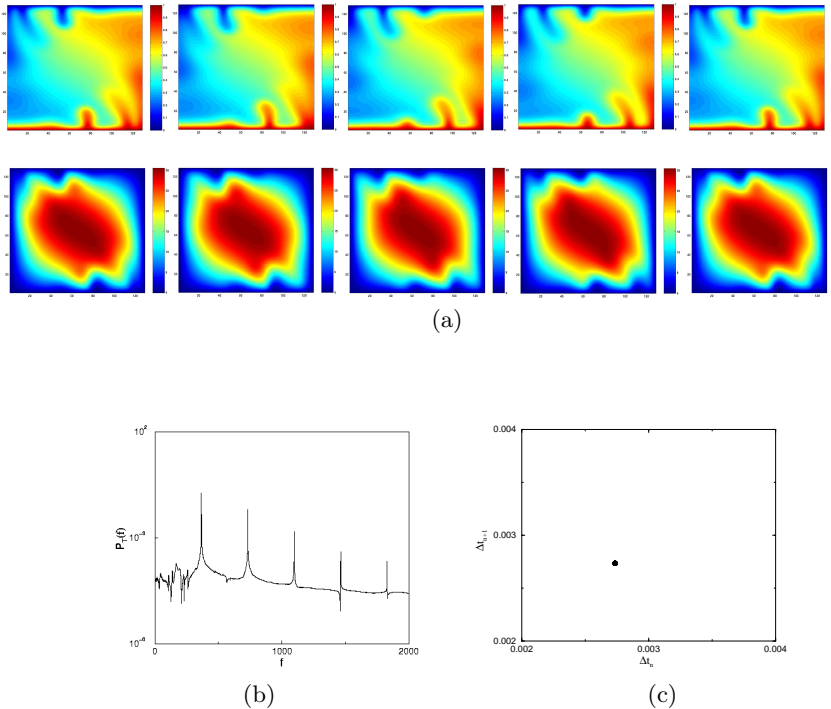


Figure 3.9: Same as figure 3.4 except that $Ra = 900$. (a) Temporal evolution of the temperature (up) and stream function (bottom) over one oscillation period, $\tau_p = 0.00273$. This time sequence shows the entire plume formation process. The overall circulation of the flow is counterclockwise. Time is increased from $t = 0.2$ with time interval $\Delta t = 0.0006$. (b) At $Ra = 900$ a single frequency, $f_{11} = 365.21$, and its harmonics prevail. (c) Poincaré section of the temperature signal at point $(x = 1/3, y = 1/3)$.

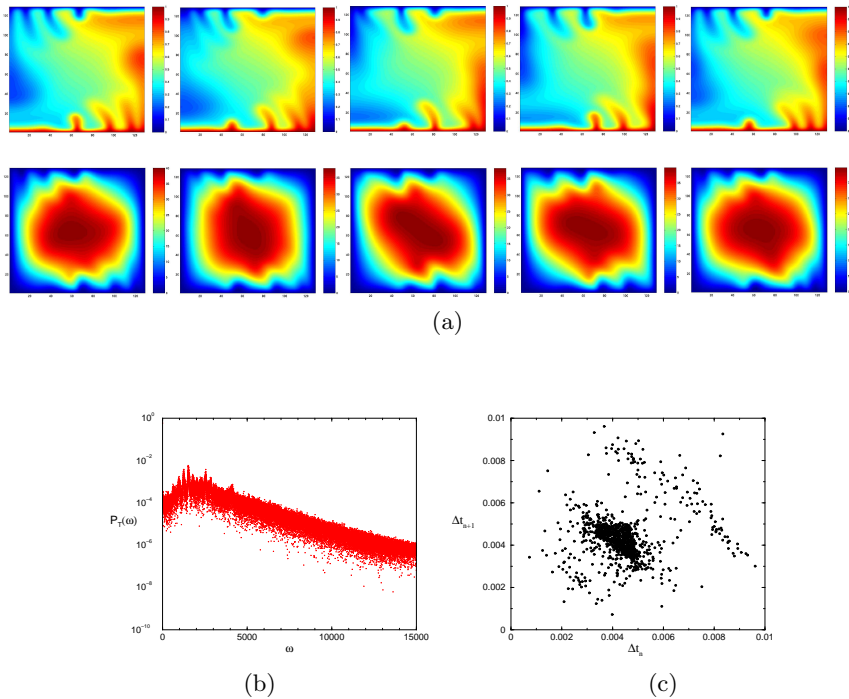


Figure 3.10: Same as figure 3.4 except that $Ra = 1200$. No single frequency prevails in the power spectrum. (a) Snapshots are taken evenly in time from $t = 0.5$ to $t = 0.604$, with time interval $\Delta t = 0.026$. (b) The power spectrum on a log linear scale illustrates the region of exponential decay. (c) Poincaré section showing the scattered points in the plane $(\Delta t_n, \Delta t_{n+1})$.

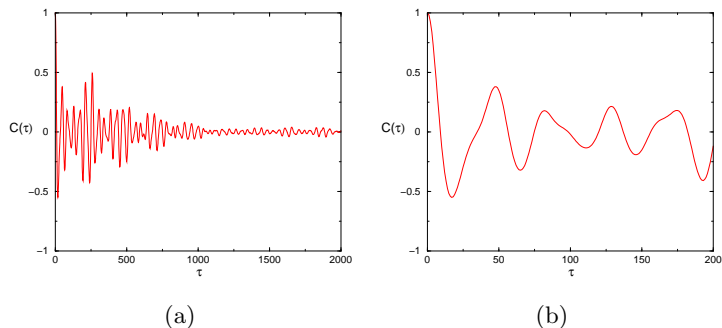


Figure 3.11: (a) The autocorrelation function of the temperature signal at point $(x = 10/128, y = 10/128)$. (b) is a close up of (a).

to follow a cycle, characterized by thermal plumes. The flow structure is similar to those at lower Rayleigh numbers, except that the plumes are very tight and stretched. This pattern repeats itself intermittently from the left of the lower boundary without any specific regularity in time, as shown in Fig. 3.10(a).

In order to gain some knowledge about the time evolution of the system one can introduce some indicators as e. g. the *autocorrelations* of time signal [59; 60]. In general, the measurement s_l of the state at time l is expressed through the probability distribution, $p(s)$, of observing different values or sequences of value. The probability distribution can be inferred from the time series. The mean of the probability distribution can be estimated by the mean of the time series

$$\langle s \rangle = \frac{1}{N} \sum_{l=1}^N s_l \quad (3.1)$$

where $\langle \cdot \rangle$ denotes the average over time and N is the total number of measurements in the time series. The variance of the probability distribution is estimated by the variance of the time series

$$\sigma^2 = \frac{1}{N-1} \sum_{l=1}^N (s_l - \langle s \rangle)^2. \quad (3.2)$$

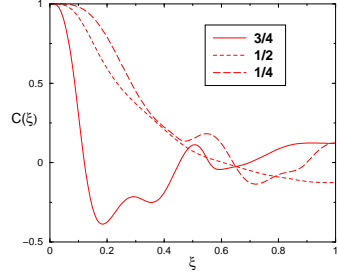


Figure 3.12: The spatial correlation function of the temperature for $\xi \in [0, 1]$, at $y = 1/4$, $y = 1/2$ and $y = 3/4$.

The autocorrelation value at lag time ν is given by

$$c_\nu = \frac{\langle (s_l - \langle s \rangle)(s_{l-\nu} - \langle s \rangle) \rangle}{\sigma^2}. \quad (3.3)$$

The autocorrelation c_ν quantifies how the signal is related with itself at time $t - \nu$. If there is no correlation $c_\nu = 0$. If the signal is observed over a continuous time, one can introduce the *autocorrelation function* $C(\tau)$ and the correlation of equation (3.3) are estimated of $C(\tau = \nu\Delta t)$. Autocorrelation of signals extracted from chaotic systems decay exponentially with increasing lag time [56]. Our simulations indicate, indeed, that the correlation functions of the temperature, decay exponentially (at least for the envelope of the function), as shown in Fig. 3.11. The spatial correlation function of the temperature has the same behavior. Figure 3.12 shows the spatial correlation curves between points at three different heights ($y = 1/4$, $y = 1/2$ and $y = 3/4$).

3.2 Conclusions

In this section, convective motions in the forms of rolls have been numerically investigated in a square Hele-Shaw cell. From chapter 1 we know the temperature difference above which convection begins, ($Ra_c = 4\pi^2$). The dynamics is simulated in the range of Rayleigh numbers between $Ra = 44$ until $Ra = 1200$. In this range, several transitions take place, modifying significantly the characteristic of the flow. These transitions are of two types. The first type is a decrease in the horizontal aspect ratio of the

cells. The second type is from steady to unsteady pattern. The principal objective of this chapter is to reproduce a chaotic behavior and letting the question of the stability analysis for the following chapters. The route to chaos found in this chapter confirms the results of time dependent behaviors by Kimura *et al.* [49; 50]. In particular, chaotic regime starts at $Ra = 1200$, in agreement with the results of Graham and Steen [51].

Chapter 4

Stability analysis

With the available analytical tools, a theoretical study of the strongly non linear convective regime is not possible. In order to get some insights of what happens when the control parameter is increased (the vertical temperature gradient in the present problem), we study the stability of a known solution (the conductive rest state). By applying infinitesimal perturbations to the basic state the threshold of stability is obtained by solving linearized equations (linear stability analysis). In the second part of this chapter, the asymptotic evolution of the finite perturbations is considered by solving a set of weakly non linear equations (non linear stability analysis). The results are compared with the experiments of Caltagirone and Fabrie [61], that show the sequence of periodic - quasi-periodic - periodic dynamics. They interpreted it as the result of a frequency locking mechanisms. However, the experimental frequency spectrum was not consistent, as showed by Graham and Steen [62], with this interpretation. The latter affirmed that quasi-periodic dynamics in porous medium convection was related with strongly interacting travelling waves.

4.1 Linear analysis

Linear stability analysis for the Hele-Shaw cell leads to calculate the minimal value of the temperature difference for which the perturbations are not damped. From the numerical point of view, the method of finite differences is replaced by the spectral collocation method, which is more accurate. A detailed description of the spectral collocation method can be found in

Appendix B.

4.1.1 Linearized equations for the perturbations

We consider the infinitesimal perturbations of the stream function ψ and of the temperature θ added to the conductive solution:

$$\psi = \psi, \quad (4.1)$$

$$\theta = T - T_{cond}, \quad (4.2)$$

the index *cond* refers to the conductive solution. By observing that T_{cond} satisfies Eqs. (2.23) and neglecting the terms with order higher than one, we obtain the linear equations satisfied by the perturbations:

$$\nabla^2 \psi = -Ra \frac{\partial \theta}{\partial x} \quad (4.3)$$

$$\frac{\partial \theta}{\partial t} = \nabla^2 \theta - \frac{\partial \psi}{\partial x}. \quad (4.4)$$

In the same way, we obtain the boundary conditions for the perturbation:

$$\begin{aligned} \psi &= \partial_x \theta = 0 & x = 0, 1 & y \in [0, 1] \\ \psi &= \theta = 0 & y = 0, 1 & x \in [0, 1] \end{aligned} \quad (4.5)$$

The linearized equations (4.3) and (4.4) represent an eigenvalue problem with solutions written as

$$\theta(x, y, t) = f(x, y) e^{st} \quad (4.6)$$

$$\psi(x, y, t) = g(x, y) e^{st} \quad (4.7)$$

where $s = \sigma + i\omega$ is the linear growth rate of the infinitesimal perturbations. By substituting Eqs. (4.6)-(4.7) in Eqs. (4.3)-(4.4), we obtain an eigenvalue problem for the Rayleigh number or alternatively for the growth rate

$$(D_x^2 + D_y^2)g = -Ra D_x f, \quad (4.8)$$

$$sf = (D_x^2 + D_y^2)f - D_x g, \quad (4.9)$$

in which we have done the substitution

$$\nabla^2 \rightarrow D_x^2 + D_y^2, \quad (4.10)$$

$$\partial_x \rightarrow D_x, \quad (4.11)$$

where D_x and D_y are the corresponding spectral operators. The instability takes place when, for a certain mode, the real part of the linear growth rate becomes positive ($\Re(s) \geq 0$). Generally the growth rate is a complex number. Hence, the marginal condition of stability $\Re(s) = 0$, may occur with $\Im(s) \neq 0$, which corresponds to an oscillatory solution with frequency $\omega = \Im(s)$. However, in the present case, the matrix of the linear problem has all the eigenvalues real. This guarantees that the instability is stationary. Since we are in the first place, mainly interested in determining the critical Rayleigh number characterizing the marginal stability, we fix $s = 0$ into Eqs. (4.8)-(4.9)

$$(D_x^2 + D_y^2)g = -RaD_x f, \quad (4.12)$$

$$(D_x^2 + D_y^2)f = D_x g, \quad (4.13)$$

with the corresponding boundary conditions

$$\begin{aligned} g &= f = 0 & y = 0, 1 & x \in [0, 1] \\ D_x f &= g = 0 & x = 0, 1 & y \in [0, 1] \end{aligned} \quad (4.14)$$

A compact form of Eqs. (4.12)-(4.13) can be written by defining some differential operators

$$L\mathbf{u} = -RaM\mathbf{u} \quad (4.15)$$

where the vector \mathbf{u} is given by

$$\mathbf{u} = (f, g)^T \quad (4.16)$$

and the matrices L and M are the following linear differential operators

$$L = \begin{pmatrix} D_x^2 + D_y^2 & -D_x \\ 0 & D_x^2 + D_y^2 \end{pmatrix}, \quad M = \begin{pmatrix} 0 & 0 \\ D_x & 0 \end{pmatrix}. \quad (4.17)$$

Equation (4.15) is a generalized eigenvalue problem $AX = \lambda BX$. Further details about the resolution are found in Appendix B.

For the case of marginal stability, we see immediately that there exists an exact solution

$$f(x, y) = \cos(k\pi x) \sin(h\pi y) \quad (4.18)$$

$$g(x, y) = \frac{-(h^2 + k^2)^2}{k^2} \sin(k\pi x) \sin(h\pi y) \quad (4.19)$$

with $h = 1, 2, \dots$ and $k = 0, 1, \dots$, are the set of natural numbers and

$$Ra = \frac{\pi^2(k^2 + h^2)^2}{k^2}. \quad (4.20)$$

It is straightforward to show that Ra is minimum when $h = 1$ and $k = 1$. The corresponding critical Rayleigh number is $Ra_c = 4\pi^2 \simeq 39.4784$.

4.1.2 Results

Before giving the results of the linear stability analysis, we give here only some basic information about the introduction of the spectral matrices in view of the numerical resolution of Eqs. (4.12)-(4.13). Due to the complexity of their implementation, we leave details in Appendix B for the interested reader.

The collocation spectral method needs the definition of the Chebyshev points in the interval $[-1, 1]$. We define the new variables $\tilde{x} = 2x - 1$ and $\tilde{y} = 2y - 1$, with $\tilde{x}, \tilde{y} \in [-1, 1]$. Equations (4.12)-(4.13) become:

$$(D_{\tilde{x}}^2 + D_{\tilde{y}}^2)\tilde{g} + \frac{1}{2}RaD_{\tilde{x}}\tilde{f} = 0 \quad (4.21)$$

$$(D_{\tilde{x}}^2 + D_{\tilde{y}}^2)\tilde{f} - \frac{1}{2}D_{\tilde{x}}\tilde{g} = 0 \quad (4.22)$$

with boundary conditions

$$\tilde{g} = \tilde{f} = 0 \quad \tilde{y} = -1, 1, \quad \tilde{x} \in [-1, 1] \quad (4.23)$$

$$D_{\tilde{x}}\tilde{f} = \tilde{g} = 0 \quad \tilde{x} = -1, 1 \quad \tilde{y} \in [-1, 1] \quad (4.24)$$

In the following, in order to make the notation lighter, tildes are omitted expecting no confusion for the reader. In the numerical procedure, we set up a grid based on 22×22 Chebyshev points independently in each direction [63]. The computation of the operator $D_x^2 + D_y^2$ is done by using combinations of Kronecker products between the identity matrix and the spectral matrix squared. The operator D_x is developed with the Kronecker product between the identity matrix and the spectral matrix D . Dealing with homogeneous Dirichlet boundary conditions is relatively easy. The corresponding matrix is stripped off its first and last rows and columns. The application of Neumann conditions at the lateral walls is realized by replacing the first and last rows of the matrix by the first and last row of the

n	m	Ra_c
0	0	39.4784
1	0	61.6850
1	1	109.6623
2	0	157.9137
3	0	178.2697
2	1	185.3292
3	1	246.7401
0	1	246.7401
4	0	266.8741

Table 4.1: n and m are integer numbers representing the geometrical node lines through the flow in the x and y direction, respectively. The flow is segmented in both directions in $n(x)$ and $m(y)$ regions. Each mode has a critical value of the Rayleigh number.

spectral differentiation matrix of first order. The matrices are not sparse as one typically gets with finite difference methods. Fortunately, given the spectral accuracy, we obtain satisfactory results with much smaller matrices.

The first nine critical modes (temperature field and stream function) are displayed in Figs. 4.1, 4.2 and 4.3. By consideration of the stream function structure, we indicate the modes with the notation, M_{nm} , where M stands for mode and the subscripts n and m are integer numbers representing the number of node lines in the x and y direction, respectively, through the flow. In other words, the flow is separated in both directions in $n(x)$ and $m(y)$ regions. Each geometrical disposition is associated with a mode.

At $Ra = 39.4784$ the spatial flow pattern preferred by the flow is the unicellular mode M_{00} . The parallel fringe of the temperature of the pure conduction have been deformed and a vertical portion of fluid rises upward along one of the lateral boundary. An increase of the Rayleigh number leads to a continuous development of two weak circulations inside the primary convective roll. At $Ra = 61.6850$ the real part of the linear growth corresponding to the two-roll flow M_{10} becomes positive. The next linear mode that becomes unstable is the M_{11} mode for $Ra = 109.6623$. At $Ra = 157.9137$ the three-roll flow M_{20} is linearly unstable. The results of the linear stability analysis are summarized in Table 4.1 where the critical Rayleigh numbers are given for the first nine unstable modes.

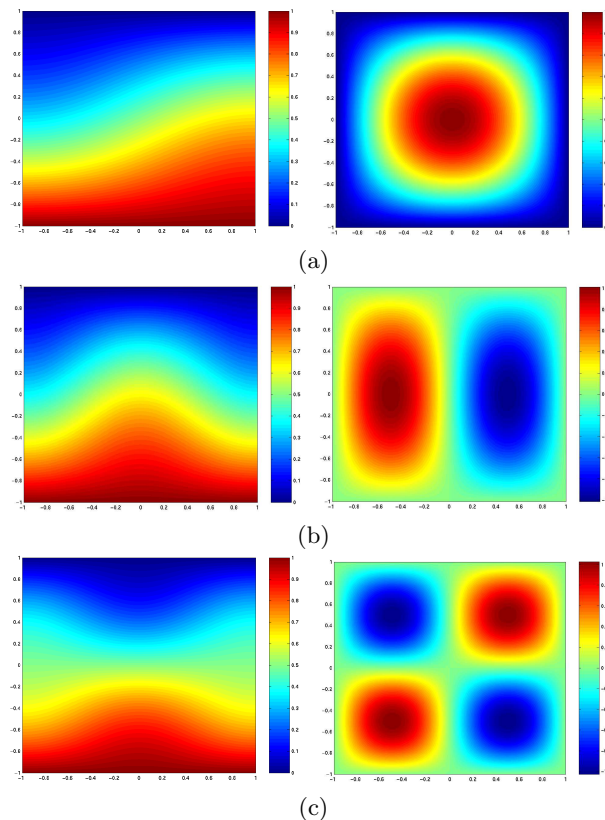


Figure 4.1: Snapshots of temperature and stream function for the first three unstable modes. (a) M_{00} mode with $Ra_c = 39.4784$; (b) M_{10} mode with $Ra_c = 61.6850$; (c) M_{11} mode with $Ra_c = 109.6623$.

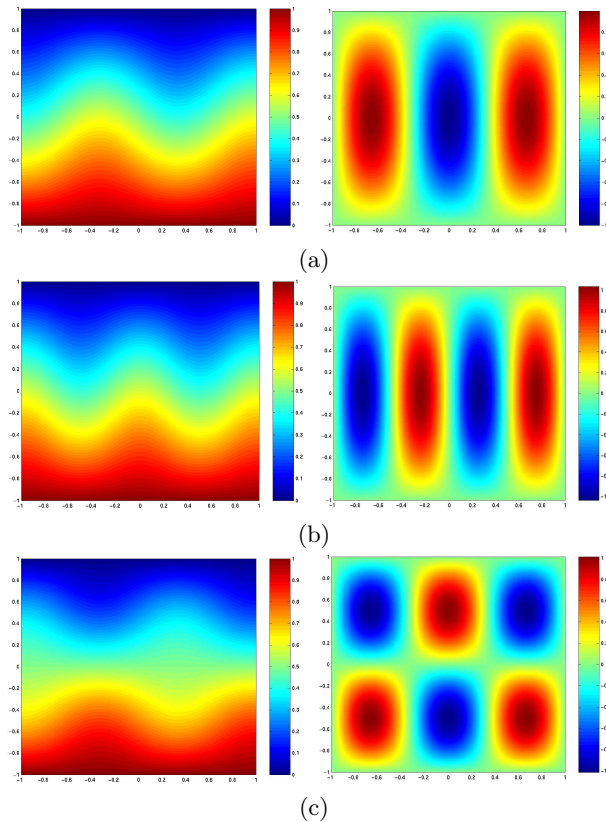


Figure 4.2: (a) M_{20} mode with $Ra_c = 157.9137$; (b) M_{30} mode with $Ra_c = 178.2697$; (c) M_{21} mode with $Ra_c = 185.3292$.

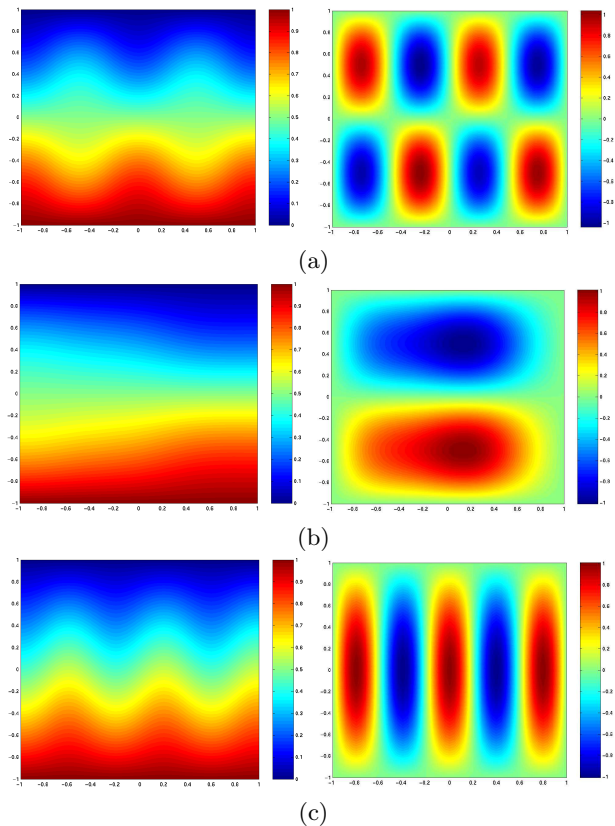


Figure 4.3: (a) M_{31} mode with $Ra_c = 246.7401$; (b) M_{01} mode with $Ra_c = 246.7401$; (c) M_{40} mode with $Ra_c = 266.8741$.

4.2 Non linear analysis

The purpose of the non linear analysis is to follow the dynamics of the linear unstable modes above threshold. The linear stability analysis has determined the thresholds from which the perturbations are not damped, but does not permit to calculate their non linear evolution. Since, close to threshold, the dynamics is governed by only a few modes, called *master* modes, (while the others, *slaves*, follow them adiabatically), a weakly non linear analysis is sufficient. The original partial differential equations is reduced to a non linear system of coupled ordinary differential equations for the amplitudes of the master modes [64].

The first task is to recognize which modes are master and which are slave. The latter will appear in the equations only as non linear interactions of the master modes. In a bounded system the spectrum of the linear operator is discrete, there is a large gap between unstable and stable modes and the distinction between master and slave is clear. Modes that are marginally unstable ($\Re(s) \sim 0$) belong to the first group, while damped modes ($\Re(s) < 0$) belong to the second one. In this context the central manifold theorem guarantees that the dynamics of the Eqs. (2.23) can be described accurately by following the evolution of the amplitude equations of the master modes. Indexing the unstable modes with M and the stable ones with S the amplitude equations are

$$\begin{aligned} \frac{dA_M}{dt} &= s_M A_M + f_M(A_M, A_S), \\ \frac{dA_S}{dt} &= s_S A_S + f_S(A_M, A_S), \end{aligned} \quad (4.25)$$

where s_M are ~ 0 , positive or negative, while s_S are negative and large. If we consider amplitudes with growth rate s_M , $|dA_S/dt| \sim |s_M|A_S$ are negligible with respect to $|s_S|A_S$ in the equations of A_S . The slow variables A_M drive the evolution of the fast variable A_S . Indeed, $A_S \simeq (-1/s_S)f_S(A_M, A_S) = g(A_M)$.

In this thesis we use the method of *Galerkin-Eckaus* [65] to get the expression for the amplitude equations. This method basically consists in doing the adiabatic elimination described above. The solution of the non linear problem is written by means of a series expansion in terms of the eigenfunctions of the linear problem. This expansion is then introduced in the non linear equations and projected onto the eigenfunctions of the adjoint linear

problem. This procedure results in an infinite set of ordinary differential equations, which is truncated by an adiabatic elimination [66]. We notice that the idea of this principle is to consider only a few active modes by splitting the number of eigenmodes into two categories: master and slave modes.

4.2.1 Computing bifurcation diagrams with AUTO

For many years non linear phenomena were unknown, and this principally for the absence of a general theory to describe them. Every problem is a particular case that one has to solve independently from the others. However recently, powerful techniques, as bifurcation theory, dynamical system theory, catastrophe theory, etc..., have been developed to solve non linear problem in a general framework. The elegant methods for qualitative analysis of differential equations, that give us the tools of phase plane and bifurcation analysis, were introduced by Poincaré in the 1890^{ies} and further developed by mathematicians as Hopf [67], Andronov and many others during the twentieth century. Bifurcation and phase plane analysis allow to identify changes in the dynamics of a system, such as hysteresis, the onset of oscillation, changes in the type of oscillation (such as period-doubling), or extinction of a solution. Bifurcation analysis refers to a body of mathematical theory and computational methods for tracking how the steady state solution of a dynamical system changes as one or more parameters are varied.

The software package AUTO [68] is specialized in continuation and bifurcation problems in ordinary differential equations. Early version of AUTO was described by Doedel [69], Doedel and Kernévez [70], Doedel and Wang [71].

The analysis of Eqs. (4.25) has been done using XPPAUT [72] which is a graphical interface for AUTO. AUTO is used for solving differential equations, difference equations, delay equations, functional equations, boundary value problems and stochastic equations. It contains the code for AUTO. Despite of what the author says, “I have put a friendly face on AUTO so you do not need to know much about it to play around with it”, XPPAUT does not have a pretty buttons and windows interface or very sophisticated graphical capabilities. There are size restrictions on some AUTO constants: the effective problem dimension, the number of collocation points, the number of mesh intervals, the effective number of equations parameters, etc...

These size restrictions can not be changed if you are using AUTO kernel with the XPPAUT interface. Furthermore, the total length of any code line can not exceed 1000 characters. We can circumvent this restriction by including files in which we define auxiliary quantities. Clearly, these files have the same restriction, and the operation “include file” is infinite.

All the above reasons explain why we have preferred the original AUTO program, for which we have access to all the parameters. A source file *xxx.f* (*xxx* stands for a user-selected name) contains the Fortran subroutines for solving the ordinary differential equations, and the relative AUTO-parameters for *xxx.f* are in a corresponding file, *r.xxx*. Only one difficulty persists: all the graphical user interfaces are lost, everything must be done in command modes.

4.2.2 Non linear problem formulation

The equations which govern the non linear evolution of the perturbations are

$$\frac{\partial \theta}{\partial t} = \nabla^2 \theta - \frac{\partial \psi}{\partial x} - \frac{\partial \psi}{\partial y} \frac{\partial \theta}{\partial x} + \frac{\partial \psi}{\partial x} \frac{\partial \theta}{\partial y}, \quad (4.26)$$

$$\nabla^2 \psi + Ra \frac{\partial \theta}{\partial x} = 0. \quad (4.27)$$

A compact form of these equations is given by

$$\mathcal{L}_t \partial_t \mathbf{p} = \mathcal{L} \mathbf{p} + \mathcal{N}\mathcal{L}(\mathbf{p}, \mathbf{p}), \quad (4.28)$$

where \mathbf{p} is the vector of unknowns

$$\mathbf{p} = (\theta, \psi)^T, \quad (4.29)$$

\mathcal{L} and \mathcal{L}_t are the linear differential operators

$$\mathcal{L} = \begin{pmatrix} \nabla^2 & -\partial_x \\ Ra\partial_x & \nabla^2 \end{pmatrix}, \quad (4.30)$$

$$\mathcal{L}_t = \begin{pmatrix} 1 & 0 \\ 0 & 0 \end{pmatrix}, \quad (4.31)$$

while $\mathcal{N}\mathcal{L}(\mathbf{p}, \mathbf{p})$ is the operator which represents the non linear terms

$$\mathcal{N}\mathcal{L}(\mathbf{p}, \mathbf{p}) = \begin{pmatrix} -\partial_y \psi \partial_x \theta + \partial_x \psi \partial_y \theta \\ 0 \end{pmatrix}. \quad (4.32)$$

4.2.3 The linear problem

The set of function used for the expansion of the solution is constituted by the eigenmodes of the linear problem (4.3)-(4.4), written in operator formulation

$$\mathcal{L}\mathbf{p} - \mathcal{L}_t\mathbf{p} = 0, \quad (4.33)$$

with boundary conditions

$$\begin{aligned} \psi = \theta &= 0 & y = 0, 1 & x \in [0, 1], \\ \partial_x \theta = \psi &= 0 & x = 0, 1 & y \in [0, 1], \end{aligned} \quad (4.34)$$

where the linear differential operators \mathcal{L} and \mathcal{L}_t are the same as Eqs. (4.30)-(4.31). The solutions are $(\theta_i, \psi_i) = [f_i(x, y), g_i(x, y)]e^{s_i t}$, where $f_i(x, y)$ and $g_i(x, y)$ satisfy the eigenvalue problem

$$(D_x^2 + D_y^2)g_i + Ra_c D_x f_i = 0, \quad (4.35)$$

$$s f = (D_x^2 + D_y^2)f_i - D_x g_i. \quad (4.36)$$

In Eqs. (4.8)-(4.9) we have considered as eigenvalue the growth rate, while the Rayleigh number is fixed to $Ra_c = 4\pi^2$:

$$L_c \mathbf{u}_i = s_i L_t \mathbf{u}_i \quad (4.37)$$

wherein the following notation has been used

$$L_c = \begin{pmatrix} D_x^2 + D_y^2 & -D_x \\ Ra_c D_x & D_x^2 + D_y^2 \end{pmatrix}, \quad L_t = \begin{pmatrix} 1 & 0 \\ 0 & 0 \end{pmatrix}, \quad \mathbf{u}_i = \begin{pmatrix} f_i \\ g_i \end{pmatrix} \quad (4.38)$$

L_c comes from \mathcal{L} , evaluated this time at the threshold for the most unstable mode. In this case the analytical solution is

$$f(x, y) = \cos(k\pi x) \sin(h\pi), \quad (4.39)$$

$$g(x, y) = \frac{-4\pi k}{h^2 + k^2} \sin(k\pi x) \sin(h\pi y), \quad (4.40)$$

where $h = 1, 2, \dots$ and $k = 0, 1, \dots$ are natural numbers and the linear growth rate is

$$s = -\frac{\pi^2[(h^2 + k^2)^2 - 4k^2]}{h^2 + k^2}. \quad (4.41)$$

The largest eigenvalue is zero and it corresponds to the marginally stable convective mode (see Fig. 4.4(a)). The values of the first nine eigenmodes

are shown in Figs. 4.4, 4.5 and 4.6.

For the second, fourth and eighth eigenvalue the stream function vanishes. These eigenmodes are called zeroth-modes. They are obtained by setting in Eqs. (4.39)-(4.40) $k = 0$. For these modes s is given by $s = -h^2\pi^2$. The solution of the non linear equations is then expressed as the following series in the eigenmodes (f_p, g_p):

$$\begin{pmatrix} \theta \\ \psi \end{pmatrix} = \sum_{p=1}^{\infty} A_p(t) \begin{pmatrix} \frac{Ra_c}{Ra} f_p \\ g_p \end{pmatrix}, \quad (4.42)$$

where A_p is the amplitude of the mode p . We underline that the functions used in this decompositions are not exactly the eigenmodes of the physical problem, due to the rescaling factor Ra_c/Ra . However, for each value of the Rayleigh number, the function g_p and $(Ra_c/Ra)f_p$ may be considered as eigenmodes of a “mathematical” eigenvalue problem, which is obtained from the original problem by adding this factor. It may be also checked that the adjoint eigenmodes of this problem are given by $((Ra/Ra_c)f_p^*, g_p^*)$, where the (f_p^*, g_p^*) are the adjoint eigenmodes of the original problem, [73]. From a more physical point of view, the introduction of the factor Ra_c/Ra in Eqs. (4.26)-(4.27) has been defined with temperature scale ΔTh , while the linear problem is solved fixing $Ra = Ra_c$. When the unknown fields are written under the form (4.42) and introduced in Eqs. (4.26)-(4.27), the latter leave defined in Ra_c . In this way the resulting Eqs. (4.26)-(4.27) are the sum of the solved linear problem with the non linear term. In the following sections, we will show that the adjoint solutions verify the bi-orthogonal relations. We will prove the bi-orthogonal relations also in the case of the added scaling factor (Ra_c/Ra) .

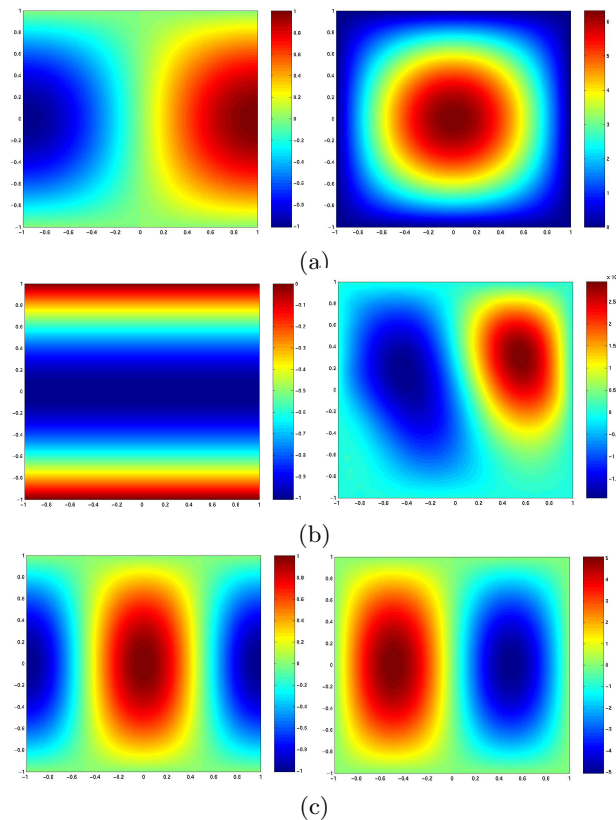


Figure 4.4: On the left: temperature perturbation; on the right: stream function perturbation; (a) M_{00} mode with $s_1 = 0$; (b) Zero mode with $s_2 = -9.8696$ ($h = 1$); (c) M_{01} mode with $s_3 = -17.7652$.

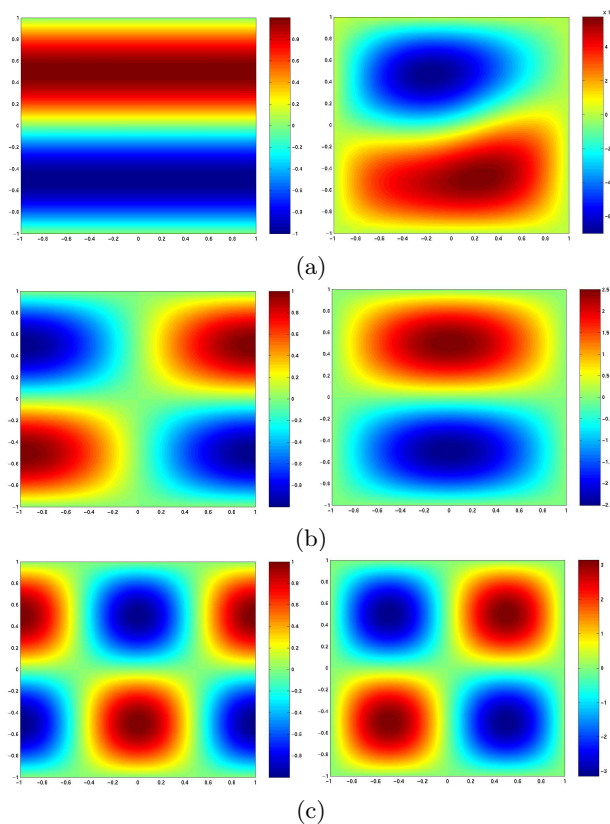


Figure 4.5: Caption as in Figure 4.4. (a) Zero mode with $s_4 = -39.4784$ ($h = 2$). (b) M_{01} mode with $s_5 = -41.4523$. (c) M_{11} mode with $s_6 = -59.2176$.

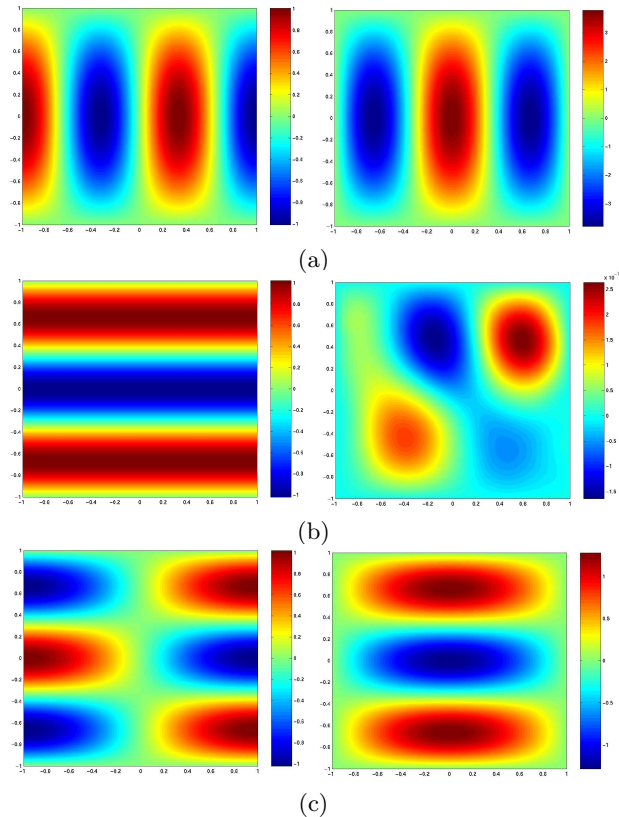


Figure 4.6: Caption as in figure 4.4. (a) M_{20} mode with $s_7 = -63.1654$. (b) Zero mode with for $s_8 = -88.8264$ ($h = 3$). (c) M_{02} mode with $s_9 = -94.7482$.

4.3 Linear adjoint problem and bi-orthogonal relations

4.3.1 Linear adjoint problem

The adjoint problem is defined by

$$\mathcal{L}^* \mathbf{p}^* - \mathcal{L}_t^* \mathbf{p}^* = 0 \quad (4.43)$$

$$\mathcal{B}^* \mathbf{p}^* = 0 \quad (4.44)$$

where \mathcal{B}^* is the adjoint of the operator \mathcal{B} which brings together the boundary conditions (4.14). From the definition of the adjoint, the operator \mathcal{L}^* and \mathcal{L}_t^* must verify the following relations

$$\langle \mathbf{p}^*, \mathcal{L}(\mathbf{p}) - \mathcal{L}_t(\mathbf{p}) \rangle = \langle \mathcal{L}^*(\mathbf{p}^*) - \mathcal{L}_t^*(\mathbf{p}^*), \mathbf{p} \rangle \quad (4.45)$$

where $\langle \dots \rangle$ denotes the integral on $[0, 1] \times [0, 1]$. By performing a series of integration by parts and using the boundary conditions Eq. (4.14), we obtain that

$$\mathcal{L}^* = \begin{pmatrix} \nabla^2 & -Ra_c \partial_x \\ \partial_x & \nabla^2 \end{pmatrix}, \quad (4.46)$$

$$\mathcal{L}_t^* = \begin{pmatrix} 1 & 0 \\ 0 & 0 \end{pmatrix}. \quad (4.47)$$

The operator which contains the boundary conditions of the adjoint problem is the same as of the direct problem ($\mathcal{B}^* = \mathcal{B}$). By analogy with the direct problem, the adjoint problem admits the solutions

$$\begin{pmatrix} \theta_i^* \\ \psi_i^* \end{pmatrix} = \begin{pmatrix} f_i^* \\ g_i^* \end{pmatrix} e^{s_i^* t}, \quad i = 1, 2, \dots \quad (4.48)$$

where s_i^* , f_i^* and g_i^* are respectively the eigenvalue and the eigenfunctions of

$$L_c^* \mathbf{u}_i^* = s_i^* L_t^* \mathbf{u}_i^*, \quad (4.49)$$

$$\mathcal{B}^* \mathbf{u}_i^* = 0. \quad (4.50)$$

L_c^* and L_t^* are the discretized operators \mathcal{L}^* and \mathcal{L}_t^* as in Eqs. (4.10)-(4.11). The analytical solution of the adjoint problem

$$f(x, y) = \cos(k\pi x) \sin(h\pi y), \quad (4.51)$$

$$g(x, y) = -\frac{k\pi}{k^2\pi^2 + h^2\pi^2} \sin(k\pi x) \sin(h\pi y), \quad (4.52)$$

where $h = 1, 2, \dots$ and $k = 0, 1, \dots$ are natural numbers and

$$s = \frac{\pi^2[k^2 - (k^2 + h^2)^2]}{k^2 + h^2}. \quad (4.53)$$

By the way, we check that the direct system and its adjoint have the same set of eigenvalues [74]. The adjoint system is solved by means of spectral collocation method, in complete analogy with the direct problem.

4.3.2 Bi-orthogonal relations (I)

The first reason for which we choose the eigenmodes of the adjoint problem as a base of projection, is the existence of bi-orthogonality relations between these functions and the eigenmodes of the direct problem. Starting from the eigenvalue problems

$$\begin{aligned} L_c \mathbf{u}_p &= s_p L_t \mathbf{u}_p, \\ L_c^* \mathbf{u}_q^* &= s_q^* L_t^* \mathbf{u}_q^*, \end{aligned} \quad (4.54)$$

and multiplying respectively, by \mathbf{u}_q^* and \mathbf{u}_p ; integrating over the volume and keeping in mind Eq. (4.45), the following relation is verified

$$(s_q^* - s_p) \langle \mathbf{u}_q^*, L_t \mathbf{u}_p \rangle = 0. \quad (4.55)$$

The above relation is called the *bi-orthogonality relations*. They express that the eigenmodes of the direct problem are orthogonal with the eigenmodes of the adjoint problem. These relations are very useful for the projection of the non linear equations into the adjoint modes. Using the definition of the operator L_t , the above relations become

$$(s_q^* - s_p) \langle f_q^*, f_p \rangle = 0. \quad (4.56)$$

4.3.3 Bi-orthogonal relations (II)

The presence of this second section for the bi-orthogonality relations is justified by the particular choice

$$\theta = \frac{Ra_c}{Ra} \sum_{p=1}^{\infty} A_p f_p. \quad (4.57)$$

In this case the expression of the eigenvalue problems is given by

$$\begin{aligned} L_c \begin{pmatrix} \frac{Ra_c}{Ra} f_p \\ g_p \end{pmatrix} &= s_p L_t \begin{pmatrix} \frac{Ra_c}{Ra} f_p \\ g_p \end{pmatrix} \\ L_c^* \begin{pmatrix} \frac{Ra}{Ra_c} f_q^* \\ g_q^* \end{pmatrix} &= s_q^* L_t^* \begin{pmatrix} \frac{Ra}{Ra_c} f_q^* \\ g_q^* \end{pmatrix} \end{aligned} \quad (4.58)$$

and we do not have, for the operators $L_{c,t}$ and $L_{c,t}^*$, an analogous relation (4.45). But an identical procedure, made of multiplication and integrations, brings to the same relation (4.56).

4.4 General expression for the amplitude equations

After introducing the expansion (4.42) into equations (4.28), one projects them on the adjoint eigenfunctions of the linear problem. We multiply equation (4.26) by $Ra/Ra_c f^*$, the temperature field of the adjoint eigenvalue problem, and equation (4.27) by g^* , the velocity field of the adjoint eigenvalue problem. These two relations are added together and integrated over the whole volume. Making use of the bi-orthogonality relations between the solutions of the eigenvalue problem and its adjoint, together with the boundary conditions, we obtain the time evolution equations for the amplitudes. This procedure can be summarized as follows

$$\langle \mathbf{U}_q^*, \mathcal{L}_t \partial_t \mathbf{U} \rangle = \langle \mathbf{U}_q^*, \mathcal{L}_c \mathbf{U} \rangle + \langle \mathbf{U}_q^*, \mathcal{N} \mathcal{L}(\mathbf{U}, \mathbf{U}) \rangle, \quad q = 1, 2, \dots \quad (4.59)$$

where

$$\mathbf{U} = \sum_{p=1}^{\infty} \begin{pmatrix} \frac{Ra_c}{Ra} f_p \\ g_p \end{pmatrix}, \quad \mathbf{U}_q^* = \begin{pmatrix} \frac{Ra}{Ra_c} f_q^* \\ g_q^* \end{pmatrix}. \quad (4.60)$$

The Eq. (4.59) defines an infinite system of ordinary differential equations for the amplitudes A_p . In the following, after having developed relation (4.59), we show in which way it is possible to reduce the dynamics to a small number of modes.

4.4.1 Projection

Projection of \mathcal{L}

$$\begin{aligned}
\mathcal{P}_q^{\mathcal{L}} &= \langle \mathbf{U}_q^*, \mathcal{L}\mathbf{U} \rangle = \left\langle \frac{Ra}{Ra_c} f_q^*, \sum_{p=1}^{\infty} A_p \left(\frac{Ra_c}{Ra} \nabla^2 f_p - \partial_x g_p \right) \right\rangle \\
&\quad + \left\langle g_q^*, \sum_{p=1}^{\infty} A_p \left(\nabla^2 g_p + Ra \frac{Ra_c}{Ra} \partial_x f_p \right) \right\rangle \\
&= \sum_{p=1}^{\infty} A_p \left\langle f_q^*, \nabla^2 f_p - \frac{Ra}{Ra_c} \partial_x g_p \right\rangle + \sum_{p=1}^{\infty} A_p \left\langle g_q^*, \nabla^2 g_p + Ra_c \partial_x f_p \right\rangle \\
&= \sum_{p=1}^{\infty} A_p \left\langle f_p, \nabla^2 f_q^* \right\rangle + \sum_{p=1}^{\infty} A_p \left\langle g_p, \frac{Ra}{Ra_c} \partial_x f_q^* \right\rangle \\
&\quad + \sum_{p=1}^{\infty} A_p \left\langle g_p, \nabla^2 g_q^* \right\rangle + \sum_{p=1}^{\infty} A_p \left\langle f_p, -Ra_c \partial_x g_q^* \right\rangle \\
&= \sum_{p=1}^{\infty} A_p \left\langle f_p, (\nabla^2 f_q^* - Ra_c \partial_x g_q^*) \right\rangle \\
&\quad + \sum_{p=1}^{\infty} A_p \left\langle g_p, (\nabla^2 g_q^* + \frac{Ra}{Ra_c} \partial_x f_q^*) \right\rangle \\
&= \sum_{p=1}^{\infty} A_p \left\langle f_p, s_q f_q^* \right\rangle + \sum_{p=1}^{\infty} A_p \left\langle g_p, \nabla^2 g_q^* + \frac{Ra}{Ra_c} \partial_x f_q^* \right\rangle \\
&= s_q \sum_{p=1}^{\infty} A_p \delta(p, q) + \sum_{p=1}^{\infty} A_p \left\langle g_p, \nabla^2 g_q^* + \frac{Ra}{Ra_c} \partial_x f_q^* \right\rangle \\
&= s_q A_q + \sum_{p=1}^{\infty} A_p \left\langle g_p, \nabla^2 g_q^* + \frac{Ra}{Ra_c} \partial_x f_q^* \right\rangle
\end{aligned} \tag{4.61}$$

Adding and subtracting from Eq. (4.61) the term

$$\sum_{p=1}^{\infty} A_p \left\langle g_p, \partial_x f_q^* \right\rangle \tag{4.62}$$

$\mathcal{P}_q^{\mathcal{L}}$ becomes

$$\mathcal{P}_q^{\mathcal{L}} = s_q A_q + \left(\frac{Ra - Ra_c}{Ra_c} \right) \sum_{p=1}^{\infty} A_p \langle g_p, \partial_x f_q^* \rangle \quad (4.63)$$

Projection of the temporal term

$$\begin{aligned} \mathcal{P}_q^{\mathcal{L}_t} &= \langle \mathbf{U}_q^*, \mathcal{L}_t \partial_t \mathbf{U} \rangle \\ &= \left\langle \frac{Ra}{Ra_c} f_q^*, \sum_{p=1}^{\infty} \frac{dA_p}{dt} \frac{Ra_c}{Ra} f_p \right\rangle = \sum_{p=1}^{\infty} \frac{dA_p}{dt} \delta(p, q) \\ &= \frac{dA_q}{dt} \end{aligned} \quad (4.64)$$

Projection of $\mathcal{N}\mathcal{L}$

$$\begin{aligned} \mathcal{P}_q^{\mathcal{NL}} &= \langle \mathbf{U}_q^*, \mathcal{NL}(\mathbf{U}, \mathbf{U}) \rangle \\ &= \left\langle \frac{Ra}{Ra_c} f_q^*, \sum_{p=1}^{\infty} \sum_{p'=1}^{\infty} A_p A_{p'} \frac{Ra_c}{Ra} (-\partial_y g_p \partial_x f_{p'} + \partial_x g_p \partial_y f_{p'}) \right\rangle \\ &= \sum_{p=1}^{\infty} \sum_{p'=1}^{\infty} A_p A_{p'} \langle f_q^*, -\partial_y g_p \partial_x f_{p'} + \partial_x g_p \partial_y f_{p'} \rangle \end{aligned} \quad (4.65)$$

4.4.2 Summary of the amplitude equations

Combining relations (4.63), (4.64) and (4.65) the amplitude equations take the following form

$$\begin{aligned} \frac{dA_q}{dt} &= s_q A_q + \delta \sum_{p=1}^{\infty} A_p \langle g_p, \partial_x f_q^* \rangle \\ &\quad - \sum_{p=1}^{\infty} \sum_{p'=1}^{\infty} A_p A_{p'} \langle f_q^*, \partial_y g_p \partial_x f_{p'} - \partial_x g_p \partial_y f_{p'} \rangle, \end{aligned}$$

that is

$$\frac{dA_q}{dt} = s_q A_q + \delta \sum_{p=1}^{\infty} C_1(q, p) A_p - \sum_{p=1}^{\infty} \sum_{p'=1}^{\infty} C_2(q, p, p') A_p A_{p'} \quad (4.66)$$

where

$$C_1(q, p) = \langle g_p, \partial_x f_q^* \rangle, \quad (4.67)$$

$$C_2(q, p, p') = \langle f_q^*, \partial_y g_p \partial_x f_{p'} - \partial_x g_p \partial_y f_{p'} \rangle. \quad (4.68)$$

The partial differential equations Eqs. (2.23) have been transformed into a system of infinite ordinary differential equations, where $\delta = (Ra - Ra_c)/Ra_c$ is the relative distance to the threshold.

4.5 Dynamics reduction

System (4.66) is clearly impossible to manage. By using the adiabatic elimination, it may be reduced to a finite number of ordinary differential equations for the amplitudes of the most unstable modes of convection.

The infinite number of eigenmodes has to be split into two categories: master and slave modes. These latter do not really take part in the dynamics of the system, but they have to be considered because they represent the response of the system to the growth of the unstable modes. Slaved modes will be present in the solution only as quadratic interactions of the unstable modes. Their own dynamics can be neglected. To be more explicit, for a slave mode the term multiplying δ may be neglected with respect to $s_q A_q$ since δ remains small, while s_q is quite negative for a well-damped eigenmode. The time derivative vanishes since the slave modes do not participate in the dynamics of the system. Furthermore, the quadratic term can be expressed as a quadratic expression in which only the amplitudes of the master modes appear, because near the threshold the amplitudes of the slave modes are rather small and terms of order higher than two can be neglected. The amplitudes of the slave modes can be expressed as

$$A_{S_q} = \frac{1}{s_{S_q}} \sum_{M_p, M_{p'}} C_2(S_q, M_p, M_{p'}) A_{M_p} A_{M_{p'}}, \quad (4.69)$$

where the sub-index S_q refers to a slaved mode, while M_p and $M_{p'}$ refer to master modes. In particular equation (4.69) shows that the amplitudes A_{S_q} become smaller as S_q increases, since the corresponding growth rate become more negative. Thus, eigenmodes with growth rate sufficiently negative can be ignored since their amplitudes are very small. By introducing the Eq.

n	s_n
1	0
2	-9.8696
3	-17.7652
4	-39.4784
5	-41.4523
...	...

Table 4.2: Spectrum of the linear growth rate for $\delta = 0$.

(4.69) in Eq. (4.66) we obtain

$$\begin{aligned} \frac{dA_{M_q}}{dt} &= s_{M_q} A_{M_q} + \delta \sum_{M_p} C_1(M_q, M_p) A_{M_p} \\ &- \sum_{M_p, M_{p'}} C_2(M_q, M_p, M_{p'}) A_{M_p} A_{M_{p'}} \\ &- \sum_{M_p, M_{p'}, M_{p''}} C_3(M_q, M_p, M_{p'}, M_{p''}) A_{M_p} A_{M_{p'}} A_{M_{p''}} \quad (4.70) \end{aligned}$$

where the matrix C_3 is given by

$$\begin{aligned} C_3(M_q, M_p, M_{p'}) &= \sum_{S_r} \frac{1}{s_{S_r}} C_2(M_q, M_p, S_r) C_2(S_r, M_{p'}, M_{p''}) \\ &+ \sum_{S_r} \frac{1}{s_{S_r}} C_2(M_q, S_r, M_p) C_2(S_r, M_{p'}, M_{p''}) \quad (4.71) \end{aligned}$$

4.6 Results

The spectrum of the linear operator \mathcal{L} ($\delta = 0$) is summarized in Table 4.2. All the modes are strongly damped, except the first one that is marginal.

The first few equations are explicitly given by

$$\begin{aligned}
 \frac{dA_1}{dt} &= s_1 A_1 + \delta C_1(1, 1) A_1 - C_2(1, 1, 4) A_1 A_4, \\
 \frac{dA_2}{dt} &= s_1 A_2 + \delta C_1(1, 1) A_2, \\
 \frac{dA_3}{dt} &= s_1 A_3 + \delta C_1(3, 3) A_3, \\
 \frac{dA_4}{dt} &= s_4 A_4 + \delta C_1(4, 4) A_4 - C_2(4, 1, 1) A_1 A_1 \\
 \frac{dA_5}{dt} &= s_5 A_5 + \delta C_1(5, 5) A_5, \\
 &\dots
 \end{aligned} \tag{4.72}$$

Weakly non linear analysis makes sense near the threshold. In this case, assuming for $n > 1$ that $dA_n/dt \equiv 0$ and $\delta A_n \equiv 0$ we get

$$\frac{dA_1}{dt} = (s_1 + \delta C_1(1, 1)) A_1 - \frac{1}{s_4} C_2(4, 1, 1) C_2(1, 1, 4) A_1^3. \tag{4.73}$$

Equation (4.73) corresponds to the normal form of a supercritical *pitchfork* bifurcation [75], which is valid close to the stability threshold of the conductive solution (i.e. $Ra_c = 4\pi^2$). The bifurcation diagram shown in Fig. 4.7 has been computed with AUTO. The conduction branch is represented in all the following graphs by blue lines. Other branches are represented with black lines. Solid lines indicate stable stationary solutions, dashed lines indicates unstable solution. The stable branch of conduction becomes unstable at $\delta = 0$ where the first bifurcation point is located. The branch point $(0, 0)$ separate domains of different qualitative behavior (see Fig. 4.7). For $\delta > 0$, one observes a steady solution formed by a two-dimensional roll. Starting from $Ra = 400$, numerical calculations of the Eq. (2.23) have shown that the evolution of the temperature and stream function fields becomes time dependent. Equation (4.73) alone is not sufficient to describe the dynamics for such a large value of δ . In fact, the steady state solution of Eq. (4.73) is always stable for $\delta > 0$. As the distance to the threshold increases, the number of modes that participate to the dynamics also increases and the amplitude equation Eq. (4.73) is not valid anymore. We need to add more amplitude equations for other modes. Previous works of Steen and collaborators about bifurcation in Hele-Shaw slots [76; 77] and

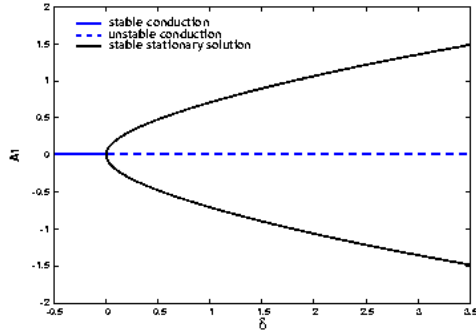


Figure 4.7: Conduction (blue lines) loses stability at $\delta = 0$, where a first bifurcation (supercritical pitchfork bifurcation) takes place (black lines). The pattern above the bifurcation point is a two dimensional roll. This bifurcation diagram has been computed with only one amplitude equation (A_1).

in square container of porous media [62] have used around 100 ordinary differential equations, and accuracy have been checked by increasing the number of modes up to 153. In the following, we will prove that the bifurcation diagram continues to be qualitatively valid, that is, we provide an approximation of the branches in the bifurcation diagram with less amplitude equations. Quantitative convergence of the bifurcation diagram means checking that the number and kind of branches do not change if the number of slave and master modes is increased.

The criterion to decide if a mode is slave or master, is obtained by comparing the corresponding value of its amplitude. If it is small (in absolute value) relatively to the largest mode, the mode is considered slave. For Rayleigh numbers close to Ra_c , Eq. (4.73), (the first mode is master, the others are slave), is sufficient to describe the convective solution. By increasing the Rayleigh number (by step of $\Delta Ra = 1$) and taking for each new value of Ra the previous solution as the initial condition, the values of the amplitudes start to grow. For example, at $Ra = 100$, the modes A_4 , A_6 , A_7 , A_9 are also masters. This means that $A_4 \simeq A_6 \simeq A_7 \simeq A_9 \simeq A_1$ and $A_i \ll A_1$ for $i \neq \{1, 4, 6, 7, 9\}$. Other steady states (modes M_{10} , M_{11}, \dots)

	master 5 slave 5	master 10 slave 10	master 20 slave 20	master 30 slave 30
B1	0	0	0	0
B2	1.7803	1.7803	1.7802	1.7802
B3	3.005	3.005	3.005	3.005
B4	3.005	5.2531	5.2531	5.2531
B5	3.005	5.7531	5.7531	5.7531

Table 4.3: Position of the first five bifurcation points for different value of master and slave modes. $B_1 \rightarrow M_{00}$, $B_2 \rightarrow M_{20}$, $B_3 \rightarrow M_{11}$, $B_4 \rightarrow M_{10}$ and $B_5 \rightarrow M_{30}$.

bifurcate directly from the conduction branch for positive value of δ . Table 4.3 shows the position in the conductive branch of the first five bifurcation points for modes (M_{10} , M_{11}, \dots). B_1 is the branch point corresponding to the M_{00} mode; B_2 is the bifurcation point of the M_{20} mode; the bifurcation point B_3 corresponds to the M_{11} mode; at B_4 and B_5 the branches of the M_{10} and M_{30} modes take place, respectively. The fact that bifurcation points in Table 4.3 have the same value for different numbers of master and slave modes, do not imply necessarily convergence of the bifurcation diagram. In fact, we have observed differences in the branches, every time we have changed the number of modes (masters and slaves).

At $Ra = 243$, with the same set of stable and unstable ones, as for $Ra = 100$ (i.e. A_1, \dots, A_9), the temporal evolution of the amplitudes is oscillating. In our amplitude equations model, periodic behaviors are already observed with only five equations (A_1, A_4, A_6, A_7, A_9). The type of bifurcation that connects equilibrium solution with periodic motion is called a *Hopf* bifurcation [75]. In addition to the first bifurcation AUTO also detects several Hopf bifurcations. Table 4.4 shows, for different branches, how the position of the Hopf bifurcation points (of the uni-cellular solution) varies with the number of master and slave modes. Bifurcation diagrams in Fig. 4.8 have been computed with 43 ordinary differential equations. Now red solid lines represent stable periodic solutions, while dashed red lines represent unstable periodic solutions. After the supercritical pitchfork bifurcation, the uni-cellular solution undergoes a first Hopf bifurcation at $\delta = 8.7875$ ($Ra = 386.39$). This new branch is initially stable and becomes unstable at $\delta = 9.9327$ ($Ra = 431.60$), as shown in Fig. 4.8(a). A second Hopf

	master 5 slave 5	master 10 slave 10	master 20 slave 20	master 30 slave 30	master 43 slave 7
HB1	5.09	7.4520	6.9463	8.0428	8.7875
HB2			7.35	8.9328	9.0427
HB3			7.5141		9.4884
TR1(HB1)					9.9327
TR2(HB1)					11.1335
TR1(HB2)					9.8739
TR2(HB2)					10.9856
TR1(HB3)					10.5108

Table 4.4: Hopf bifurcations and torus bifurcation points of the M_{00} mode for different value of master and slave modes. In the upper part: HB1, HB2 and HB3 are Hopf bifurcation points located on the steady branch of the unicellular solution (M_{00}). In the lower part: two torus bifurcations take place on the first ($TR1^{(HB1)}, TR2^{(HB1)}$) and second periodic branch ($TR1^{(HB2)}, TR2^{(HB2)}$). The third one present only one torus bifurcation ($TR1^{(HB3)}$). The blanks in the table mean nonexistent branch point.

bifurcation takes place at $\delta = 9.0427$ ($Ra = 396.46$) and remains unstable, until the third Hopf bifurcation appears at $\delta = 9.4884$ ($Ra = 414.06$), see Fig. 4.8(b-c).

Since, between all the steady state that bifurcate from the conduction branch solution, the M_{20} mode is the one observed in full numerical simulation, we present also its bifurcation diagram. The M_{20} mode becomes stable at $\delta = 2.499$ ($Ra = 137.77$) through a Hopf bifurcation, as shown in Fig. 4.9(a). Two saddle nodes bring the steady solution to a new unstable condition, as shown in Fig. 4.9(b). The stability of this mode (three-cellular solution) explains the frequent occurrence of this solution, during the numerical simulations of Eq. (2.23).

Table 4.4, shows that each periodic solution of the uni-cellular mode undergoes a *torus* bifurcations which justify the appearance of a quasi-periodic state. In fact, quasi periodic regimes are the result of the stability exchange between limit cycles.

Due to its size the maneuverability of the ODE system begins to be challenging. We are surprised by the number of equations necessary to explore

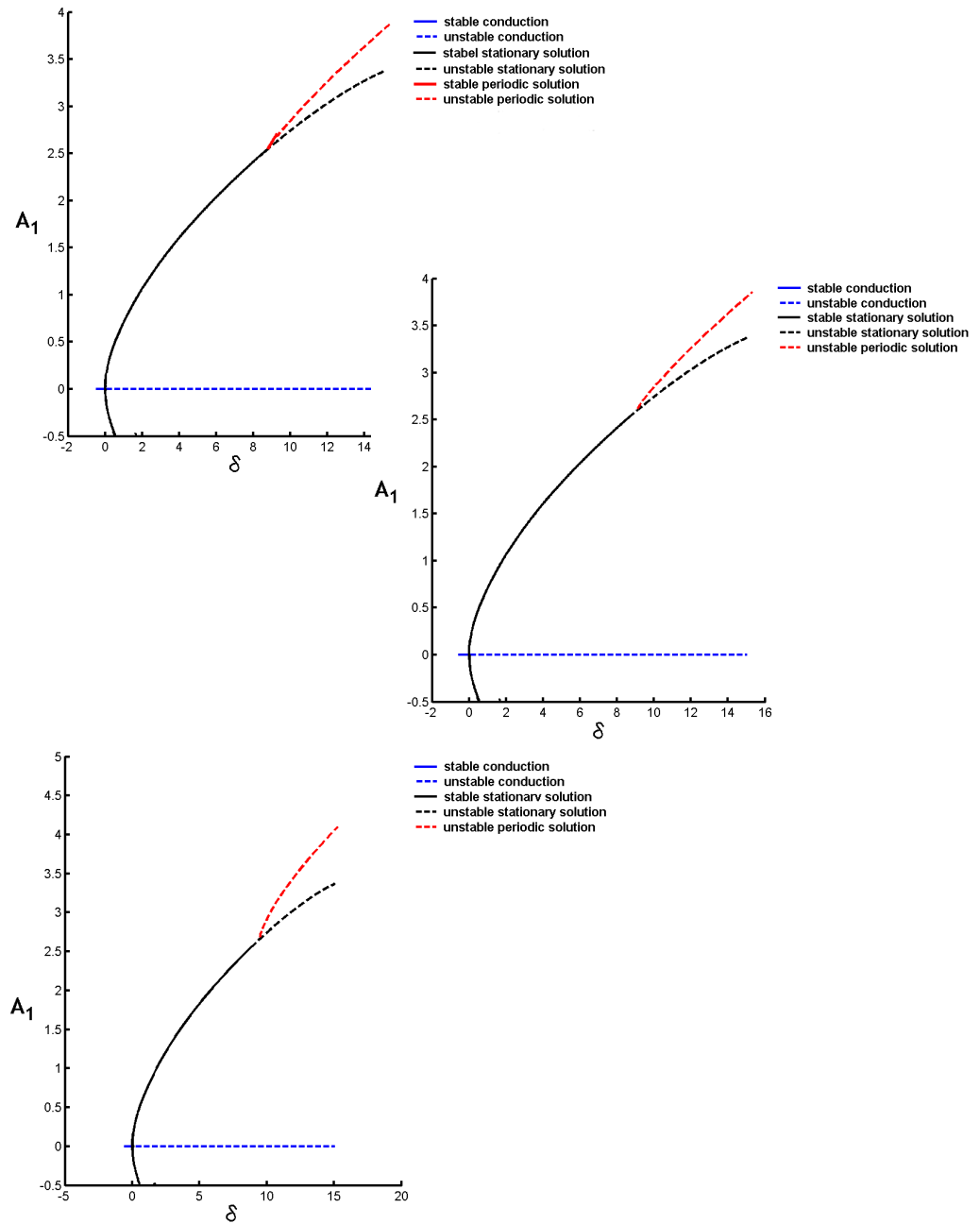


Figure 4.8: Periodic solution for the uni-cellular mode (M_{00}). A first Hopf bifurcation takes place at $\delta = 8.7875$. This oscillatory solution becomes unstable at $\delta = 9.9327$. Two other unstable Hopf bifurcations are located at $\delta = 9.0427$ and $\delta = 9.4884$. The diagrams have been computed solving 43 amplitude equations with AUTO.

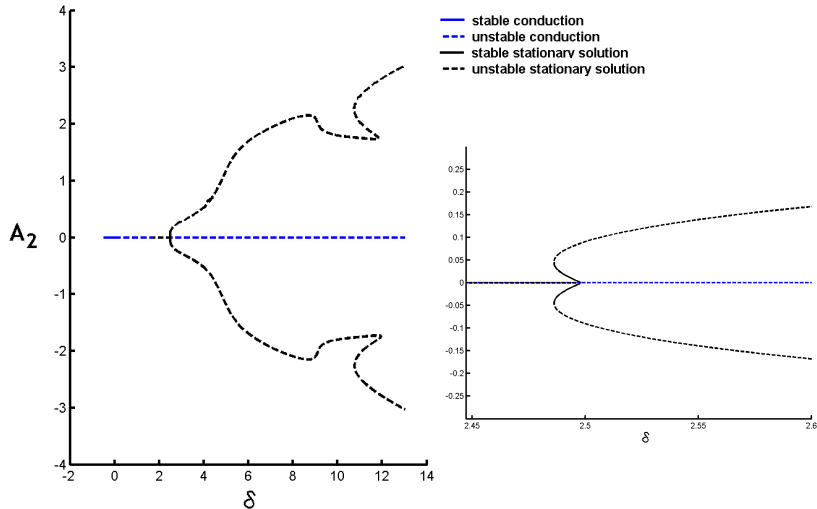


Figure 4.9: Bifurcation diagram for the M_{20} mode. The branch is born unstable at $\delta = 1.7802$ ($Ra = 109.75$). At $\delta = 2.499$, it becomes stable through a Hopf bifurcation. For $\delta = 2.486$ the oscillatory solution becomes unstable through a saddle node bifurcation. The above diagrams have been computed with 43 amplitudes equations.

the bifurcation diagram for larger value of δ . We have reached the limit given by our computational resources. However, from examining the numerical results of Eq. (2.23), we know that the scenario begins with a first bifurcation due to a time periodic fluctuation with spatial wave number $n = 5$. A second bifurcation lead to a quasi-periodic regime, and a third bifurcation restores the solution to the periodic behavior. This latter oscillation have wave number $n = 7$. Hence, the most dangerous perturbation around the second bifurcation point, is a travelling wave pattern of seven pairs of alternating warm and cold blobs swept around the box. Fig. 4.10 summarizes the scenario of the stability exchange between the periodic solution ($n = 5$) to the periodic solution ($n = 7$) through an excursion to the quasi-periodic state for intermediate value of δ , (or equivalently Ra). The diagonal line at the left represents the steady state, where are located the three Hopf bifurcations ($n = 5, 3, 7$). The horizontal lines indicates the periodic solutions which are born at the Hopf bifurcation points. The narrow lines predicts quasi-periodic solutions: the periodic uni-cellular solution

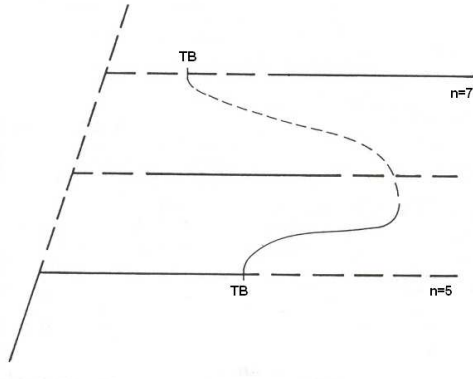


Figure 4.10: Solid line indicates stable solutions, dashed line unstable ones. Bold curve represent computed steady and periodic solution, narrow ones predicted quasi-periodic solutions.

($n = 5$) undergoes a torus bifurcation. The new frequency, uncomensurable with the first, corresponds to the frequency of the periodic solution with wave number $n = 7$. The quasi-periodic solution persists until it jumps back to a simply periodic solution with $n = 7$. This jump happens at saddle-node bifurcation point.

We suspect that the quasi-periodic regime observed at $Ra = 1000$ is again due to the interaction of periodic travelling wave states.

4.7 Conclusions

In this chapter the stability analysis of the M_{00} mode has been investigated thoroughly. Linear stability analysis yields a sufficient condition of instability of the eigenmodes. Weakly non linear analysis is valid close to the threshold. By increasing the distance to the threshold, we need to add more modes in order to reproduce accurately the dynamics. Previous works by Steen *et al.* used a large number of ordinary differential equations, and thus showed the limit of this kind of analysis. Conduction looses its stability at $\delta = 0$ where the first bifurcation point is located. A supercritical pitchfork bifurcation takes place and the corresponding spatial pattern is the unicellular mode. The first Hopf bifurcation is located at $\delta = 8.7875$. The

oscillatory solution is stable and becomes unstable at $\delta = 9.9327$ through a torus bifurcation. Several Hopf bifurcations follow the first one. Interaction of the limit cycles of periodic solutions are responsible of the quasi-periodic state. The present scenario is summarized in Fig. 4.10. The impossibility of using more equations prevents the investigation of the bifurcation diagram for larger value of the parameter δ . We assume that the scenario for large δ is characterized by the same interactions as discussed above. Other steady states (M_{20}, \dots) bifurcate from the conduction branch. In particular, by using 43 amplitudes equations the M_{20} stability has been investigated. This was motivated by the frequent occurrence of the three-cellular solution in the numerical simulation of Eq. (2.23).

Chapter 5

Synchronization

In the previous chapters we have shown that by heating uniformly from below a Hele-Shaw cell a large number of different dynamical regimes may appear: stationary convection, oscillatory convection, thermal plumes and turbulent flow. The diversity of these behaviors, in a rather simple geometry, is a good candidate in order to study possible synchronization mechanisms between two such cells. We give particular emphasis to the synchronization of chaotic dynamics. Different coupling schemes have been proposed in order to achieve synchronization. A widely used coupling, and controlling, technique is the so called “pinning” technique [13; 14; 15; 78], which connects pair of points of the two systems.

5.1 All internal points are connectors

Starting from two identical Hele-Shaw cells, we introduce a thermal bidirectional coupling between *all* the internal points. This means to add a dissipation term to the equations (A.34) and (A.35). The systems are now governed by

$$I \quad \begin{cases} \frac{\partial T^{(1)}}{\partial t} = \nabla^2 T^{(1)} + J(T^{(1)}, \psi^{(1)}) + \epsilon(T^{(2)} - T^{(1)}) \\ \nabla^2 \psi^{(1)} = -RaG_2(T^{(1)}) \end{cases} \quad (5.1)$$

$$II \quad \begin{cases} \frac{\partial T^{(2)}}{\partial t} = \nabla^2 T^{(2)} + J(T^{(2)}, \psi^{(2)}) + \epsilon(T^{(1)} - T^{(2)}) \\ \nabla^2 \psi^{(2)} = -RaG_2(T^{(2)}) \end{cases} \quad (5.2)$$

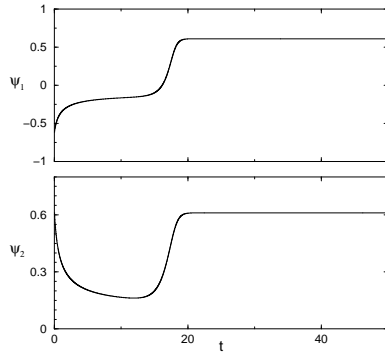


Figure 5.1: Time evolution of ψ_1 and ψ_2 at the point $x = 1/3$; $y = 1/3$. Complete synchronization for steady convection at $Ra = 44$.

where the indexes 1 and 2 refer to the two cells, ϵ is the thermal coupling and is applied in all the interior points ($i, j = 1, \dots, N - 1$).

Before presenting the results for the synchronization of chaotic systems, we want to briefly discuss the cases of steady and periodic convection.

At $Ra = 44$, two systems with a single convective cell, the first system with clockwise rotation flow, the second one with counterclockwise rotation flow are prepared by particular choice of the initial conditions. By setting the thermal coupling ϵ in the interval $[0.35, 1]$, synchronization between the two cells is achieved. The flow of one of the systems changes its rotation direction. Figure 5.1 shows complete coincidence of the dynamics of the two systems after some transient for the coupling $\epsilon = 0.5$.

For the periodic case, $Ra = 400$, the two cells are prepared with counterclockwise rotation but they are set initially out of phase, see Fig. 5.2(a). This can be done by taking as initial conditions for the second system the final state of the first after a time of exactly half period. By applying a thermal coupling $\epsilon = 0.05$ after 1000 iterations ($\Delta t = 0.0001$), the two periodic states come in phase, see Fig. 5.2(b). We underline that this is the simplest case of synchronization. We switch through two different states of synchronization: from synchronization in anti-phase to synchronization in phase.

Let us now discuss the case of chaotic dynamics at $Ra = 1200$. In this case, the correlation function is of interest because it is one central measure for quantifying synchrony. Recent papers illustrate the power of the correlation

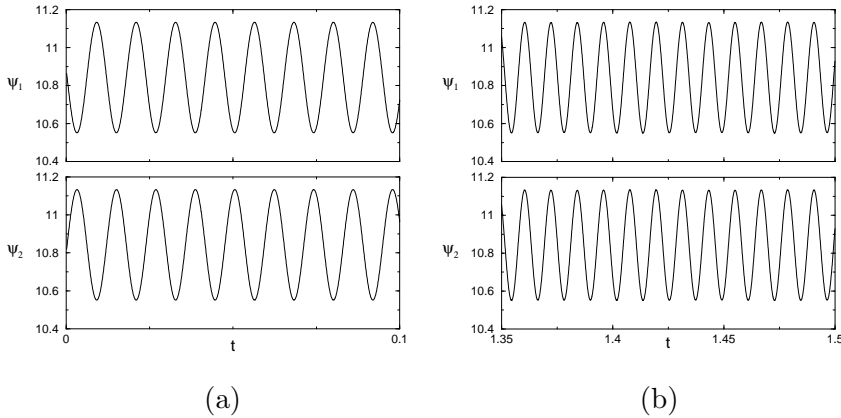


Figure 5.2: Time series of ψ_1 and ψ_2 at the point $x = 1/3$; $y = 1/3$. Complete synchronization for periodic convection at $Ra = 400$. (a) At the beginning the time series are out of phase. (b) Under the presence of the coupling the periodic oscillations come in phase.

in measuring the synchrony [2; 3; 18]. The most common way to quantify the degree of synchronization between two variables is by monitoring the Pearson's coefficient γ , or zero-lag cross-correlation

$$\gamma = \frac{\langle (T_1 - \langle T_1 \rangle)(T_2 - \langle T_2 \rangle) \rangle}{\sigma_1 \sigma_2} \quad (5.3)$$

where we recall that $\langle \rangle$ and σ^2 denote a full space-time average and the variance, respectively, and T_1 and T_2 are the temperature fields of the two systems. Precisely, when $\gamma = 0$ the two fields are linearly uncorrelated; $\gamma = 1$ marks complete correlation and $\gamma = -1$ indicates that the fields are negatively correlated. Figure 5.3 reports the Pearson's coefficient as function of the thermal coupling ϵ . The results indicate that for value of the coupling smaller than 0.02 the Pearson's coefficient is almost one. But, as we will see later, this not necessarily means the appearance of a complete synchronization state for such low values of the coupling.

The cells have been prepared both with counterclockwise rotation but with different initial conditions. The proper way to do this is analog to what has been done for the periodic case. In order to see the differences between the systems we plot the variables of cell I vs the variables of cell II, (what

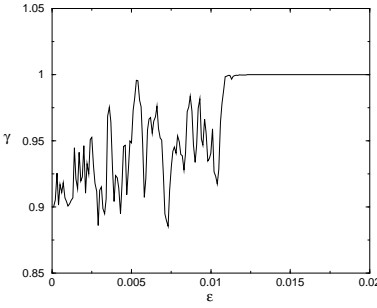


Figure 5.3: Pearson's coefficient (see text for definition) vs the thermal coupling ϵ .

is known as a Lissajous-type of plot) as in Fig. 5.4(a). Obviously, the time series give us the same information, as shown in Fig. 5.4(b). We connect the two systems with couplings $\epsilon = 0.5, 0.05, 0.02, 0.01$ at the dimensionless time $t = 0.01$. Once we get synchronization, the states of the systems are identical, as it can be easily seen on the plot ψ_1 vs. ψ_2 , (see Fig. 5.4(c)). The trajectory lies on the diagonal $\psi_1 = \psi_2$. However, it is important to note that the coupling does not destroy the chaotic dynamics, but the oscillations are nearly identical, as shown in figure 5.4(d).

In order to verify the complete synchronization we have defined the synchronization error as:

$$E = \sum_r |T_1(r) - T_2(r)| \quad (5.4)$$

where r stands for all the interior points. Another important parameter for characterizing the synchronization is the time that we have to wait in order to obtain the perfect coincidence of the trajectories of the two systems. The error has a practical importance, in fact we decide to stop the program when the error is less than 10^{-6} , a value for which we are sure to have reached a synchronized state. In Fig. 5.6, the error is plotted for different values of the coupling. Obviously, the rate of convergence to the synchronized state is faster for stronger couplings. For weaker couplings the transient times increase. There is a critical value of ϵ below which synchronization is no longer obtained. The space-time plots of the temperature taken at a height $h = 10/128$ (from the bottom wall) are shown in Fig. 5.5, showing the dynamics of the plumes drifting to the right wall after being created. At time $t = 0.01$ the coupling is switched on with $\epsilon = 0.5$. Immediately after

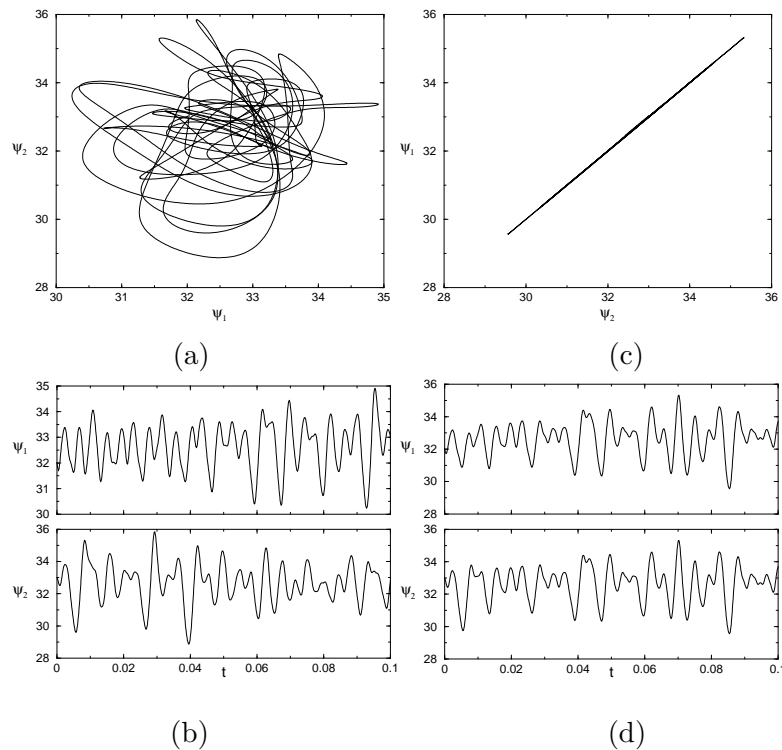


Figure 5.4: (a) Uncoupled Hele-Shaw cells, ψ_1 vs ψ_2 ($\epsilon = 0$, $x = 1/3$; $y = 1/3$). (b) Time series of the stream function below the synchronization threshold. (c) and (d) Complete synchronization in coupled Hele-Shaw cells ($\epsilon = 0.05$). The states of the systems are identical.

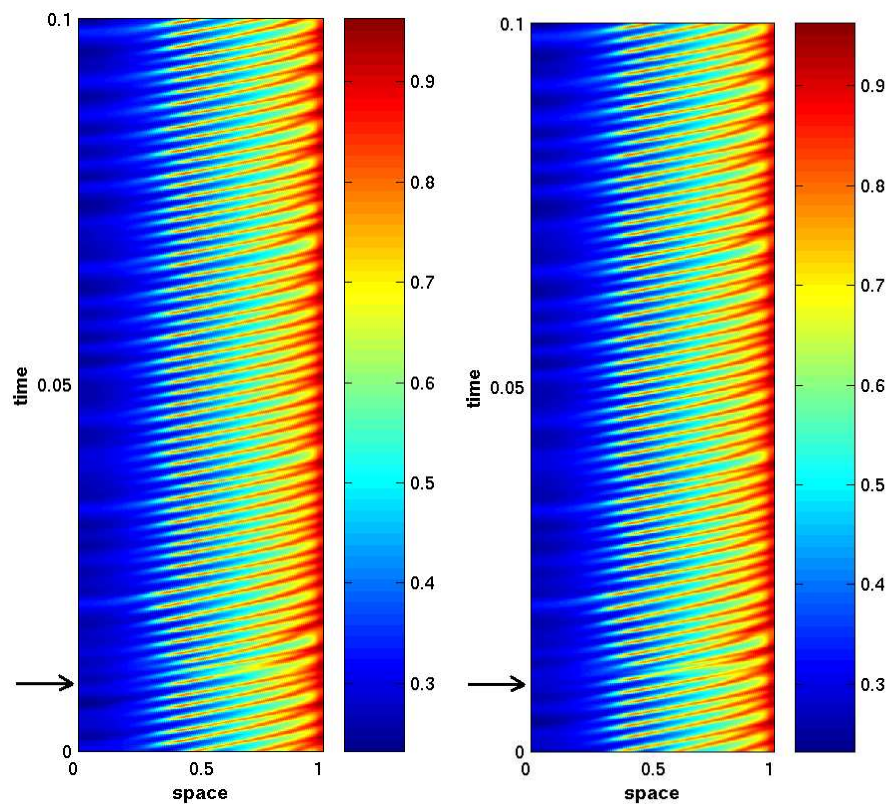


Figure 5.5: Space-time plots of the two convective cells at $h = 10/128$. At time $t = 0.01$ (where the arrows are located) the coupling ($\epsilon = 0.5$) is switched on.

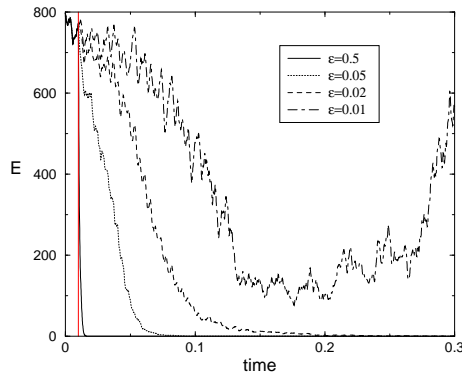


Figure 5.6: Synchronization error E (see text for definition), for several values of the coupling strength. The convergence rate is proportional to ϵ . For $\epsilon = 0.01$ synchronization is no longer achieved.

the coupling is set, the states come close to each other and they converge slowly towards the synchronized state.

5.2 Coupling through the lateral walls (only)

Until now, we have shown theoretically that synchronization between two Hele-Shaw cells is possible for a sufficiently large coupling. In this section, we consider its feasibility from the experimental point of view. This is not an easy task. An obvious limitation is how to implement the coupling between the two convective cells without perturbing too much the dynamics. The coupling technique used so far consisted in connecting the whole spatial domain. This is not clear yet how to realize such a connection between all the internal points of the systems. This may simply be impractical in experiments. On the other hand, because of the smallness of the spatial correlation length (see Fig. 3.12), it seems (at least intuitively) that we need to put several internal connectors between the two systems. This number of connectors must be finite and as small as possible. The reason for which we do not couple in the whole spatial domain is that the uncoupled areas receive information from the coupled areas that are in their neighborhood.

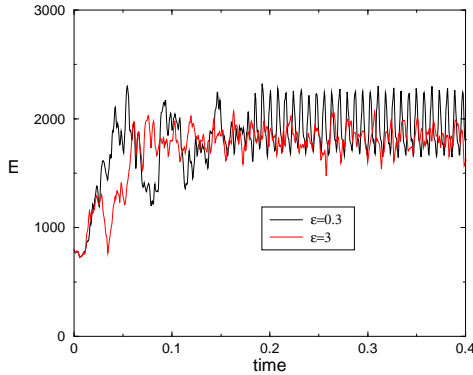


Figure 5.7: Synchronization error using an intermediate ($\epsilon = 0.3$) and a very strong coupling ($\epsilon = 3$) connecting only the points located at the lateral boundaries. Synchronization is not achieved in these cases.

In addition, we also mention that the experimental measuring devices have a finite time and space resolutions and measure local spatial information of some observable.

Let us now give a brief account of the future experiment. It has been thought to work by using the Peltier effect in order to add or extract heat from the system. In 1934, J. Peltier discovered that the passage of an electric current through the junction of two dissimilar conductors can either cool or heat this junction, depending on the direction of the current. Heat generation or absorption rates are proportional to the magnitude of the current and also the temperature of the junction. Let us now return to the results of the numerical simulation, the cells are prepared with different initial conditions. Both cells have Peltier devices connected on each lateral boundary. Their positions coincide for the two cells. The temperature of the fluid at the location of each Peltier device is constantly measured. Let us assume that a fluid parcel has a different temperature in the two cells. The Peltier device in contact with the warmer fluid will extract heat and locally cools the surrounding fluid, the corresponding device in the other cell will inject the same amount of heat. This process will last until the temperature measured in both systems are equilibrated.

In order to test the feasibility of this experimental setup, we are using controllers only belonging to the lateral vertical walls i.e. 256 mesh points.

With this particular choice the systems are governed always by the same equations (5.1), where the term $\epsilon(T_{i,j}^{2,1} - T_{i,j}^{1,2})$ appears when $i = 1, \dots, N-1$, but only for $j = 1$ and $j = N-1$. A direct inspection of the synchronization errors suggest that this type of connection is not strong enough to achieve synchronization. From Fig. 5.7, we observe that the synchronization error is even worse when using a very strong coupling, $\epsilon = 3$.

5.3 Finite number of internal points are used as connectors

The failed attempt of synchronization through only the lateral walls brings us to consider what are the minimal number of “internal” points necessary in order to obtain synchronization. As a rule, in experiments one will try to use as few controllers as possible. The simplest way to start investigating the minimal number of controllers is to put the connectors every two grid points and, in case of success, following the reduction of connectors in this way. For a controller every two grid points one gets synchronization, but we observe a change in the organization of the patterned flow, (see Fig. 5.8). For a connector every two grid points, the flow passes from a single roll cell (chaotic) to a three-cellular convection mode (stationary). The convergence to the synchronization state is not fast. Here the synchronization drastically affect the final dynamical state of the system i.e. we have chaos suppression. Presumably, the basin of attraction of the single chaotic cell is quite narrow and a sparse and strong coupling will bring the dynamics to fall in the three-cellular steady solution. The reason is that this solution is selected when strong perturbations are applied to the single chaotic cell. In order to avoid the destruction of the single cell solution, we have to increase very slowly the coupling from zero to its nominal value. Unfortunately, all attempts to keep the single mode with less connectors have failed so far. Even worse, is the case of a connector every four grid points, in that case the synchronization is no longer achieved and the solution single mode is destroyed into a two-cellular solution with recirculation flow in the lower corners that is still chaotic.

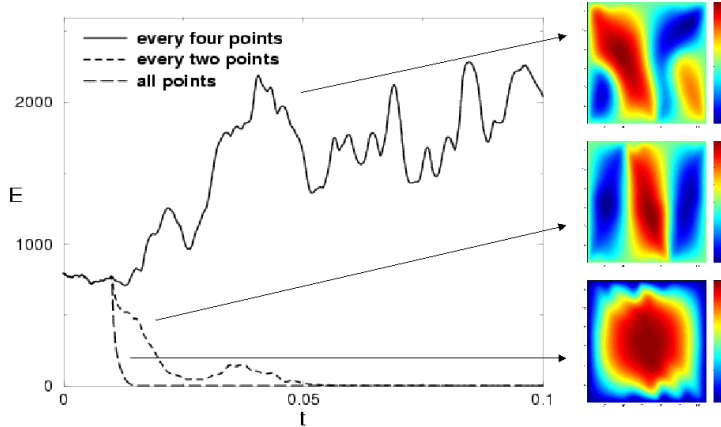


Figure 5.8: The synchronization error obtained by connecting all internal points, every two points and every four points. The coupling parameter, $\epsilon = 0.5$, is set at $t = 0.01$. For a loose connection (every two points) a new three-cellular stationary structure appears. For a connector every four points, synchronization is not achieved.

5.4 Non uniform grid

The dynamics of the Hele-Shaw cell is determined by the boundary layer instabilities. As the center of the cell practically does not participate in the dynamics, we propose to connect points belonging to a “hole-grid”. But, in order to avoid destroying the uni-cellular solution we need to couple the two cells with as much as 14000 points (85% of the number of grid points). Otherwise, synchronization is also achieved but the solution falls in a multi-cellular mode.

The best choice for the connectors would be couple points which follow the inverse of a gaussian distribution. In this case, the concentration of points would be larger near the boundaries and smaller in the center. This is typical of grid built over Chebyshev points. In fact, as $N \rightarrow \infty$ they are

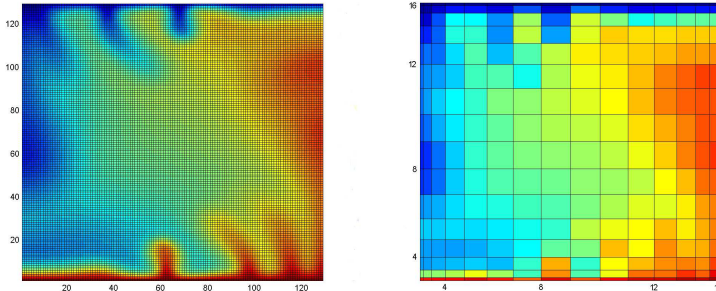


Figure 5.9: Uniform grid of 129×129 points and non uniform grid of 17×17 points.

distributed with density

$$d \sim \frac{N}{\pi\sqrt{1-x^2}}. \quad (5.5)$$

Geometrically, we can visualize these points as the projection on $[-1, 1]$ of equispaced points in the upper half of the unit circle. We send to Appendix B for technical details. In Fig. 5.9, we show that the uniform grid of 129×129 points used until now and a non uniform grid of only 17×17 points.

In this section, we test the synchronization by using Chebyshev points (CP). Time discretization is obtained with a simple Euler scheme. For the uni-cellular solution, 17×17 CP are sufficient to observe periodic oscillations. To obtain the quasi-periodic regime we need 22×22 points. Chaotic behaviors need 36×36 CP.

We investigate the synchronization mechanisms using as connectors all the internal points. At $Ra = 400$ we prepare the oscillating cells in anti-phase. Figures 5.10(a-b) show complete synchronization using thermal couplings $\epsilon = 0.5$ and $\epsilon = 1$, respectively for $Ra = 400$. In case of quasi-periodic ($Ra = 520$) and chaotic ($Ra = 1200$) regimes, stronger couplings and longer transients are needed to show complete coincidence of the trajectories. Figures 5.11(a-c) shows the behaviors of the temperatures T_1 and T_2 evaluated at the point $(x, y) = (1/3, 1/3)$ in quasi-periodic and chaotic regime, respectively. Figures 5.11(b-d) show the temperatures T_1 and T_2 after the application of the coupling $\epsilon = 1$. In order to achieve complete synchronization we can use less connectors with a lower coupling strength,

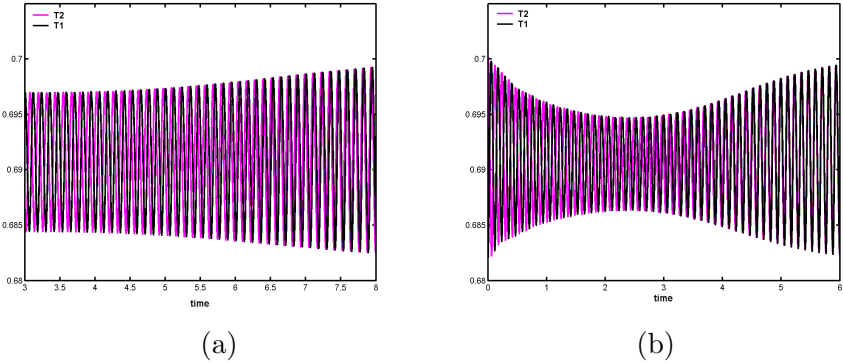


Figure 5.10: Time series of the temperatures T_1 and T_2 at the point $(x, y) = (1/3, 1/3)$. Complete synchronization of periodic convection at $Ra = 400$, using the internal points of a non uniform grid 17×17 as connectors, under the presence of thermal coupling (a) $\epsilon = 0.5$ and (b) $\epsilon = 1$.

but at expense of transient time.

5.5 Conclusions

In this chapter, we have investigated possible synchronization mechanisms between two Hele-Shaw cells. We have coupled them using a bidirectional thermal coupling ϵ . This means, adding a dissipation term, equal to the difference of the temperature fields, multiplied by ϵ . In particular, we use the pinning technique, which connects pairs of points of the two cells. For the first trials, the temperature and the stream function are discretized in space over a two dimensional uniform square ($\Delta x = \Delta y$) grid of 129×129 points. Using all the internal points (i.e. 16129) as connectors, complete synchronization is achieved for stationary convection ($Ra = 44$), periodic convection ($Ra = 400$) and chaotic regime ($Ra = 1200$). With this grid, small couplings are enough. $\epsilon = 0.01$ is the smallest coupling which leads to synchronization in the chaotic case. The future experiment, directed by H. Mancini, leads us to consider the synchronization also from the experimental point of view. In this context, the cell are connected with Peltier devices on the lateral boundaries. We numerically translate this set-up, but an in-

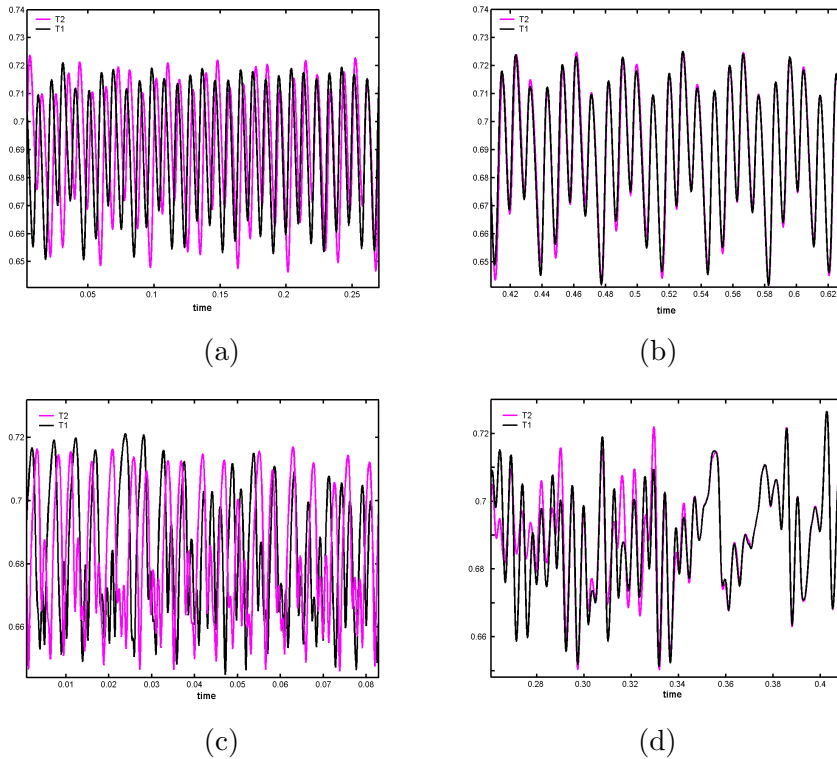


Figure 5.11: (a-c) Time series of the temperature T_1 and T_2 at the point $(x, y) = (1/3, 1/3)$ for quasi-periodic ($Ra = 520$) and chaotic ($Ra = 1200$) regime, respectively. Complete synchronization is achieved under the presence of a thermal coupling $\epsilon = 1$ and using (b) 400 (83% of the mesh grid numbers) and (d) 1156 (88% of the mesh grid numbers) connectors.

spection of the synchronization error suggests that this type of connection (i.e. 254 mesh points) is not strong enough to obtain synchronization. In experiments, one must try to use as few controllers as possible. As a consequence, we investigate the minimal number of internal points necessary to synchronize the Hele-Shaw cells. The simplest way to proceed is taking connectors every two points, every four, every eight...but all these choices drastically affect the final dynamical state, that is, they suppress chaos and synchronize the cells in other (stationary) solutions [79]. The consideration of the dynamics of a single Hele-Shaw cell which shows boundary layer instabilities, suggests to use more connectors near the boundaries and less in the center of the cell. The resulting non uniform grid is the one obtained by using Chebyshev points. The results are slightly improved. Chaotic signals are synchronized with only 1156 connectors (88% of the total numbers of grid points).

Chapter 6

Conclusions

In this thesis we have studied possible configurations to synchronize two Hele-Shaw cells. Before dealing with the synchronization of the cells, we have studied the dynamics of a single one. The dynamics of this fluid system is interesting in itself as it exhibits a boundary layer instability at reasonably small Rayleigh number. Let us recall the main results of this work:

- Since two dimensional systems are more amenable to experiments and simulations than three dimensional systems, we have proposed a model for the flow within the Hele-Shaw cell. If $K = d^2/12$ is the porous medium permeability, the governing equations of a flow in the Hele-Shaw cell are formally identical to that describing a flow through a uniform porous medium. Therefore, Lapwood's thermal instability analysis is valid, and the critical Rayleigh number for convective motion is $4\pi^2$.
- The integration of the Hele-Shaw cell for different values of the Rayleigh number has been done first by using finite difference scheme. The results made clear the richness of the dynamics of the Hele-Shaw cell. Two type of transitions have been observed. The first one is an horizontal decrease of the aspect ratio of the convective rolls. The second one is from steady to unsteady patterns.
- For large value of the Rayleigh number, there is multi-stability between multicellular stationary solutions and time dependent unicel-

lular mode. From the point of view of dynamical systems, we have decided to force the solution into the uni-cellular mode, which is unsteady for Rayleigh number larger than approximatively 350. The pattern selection depends from the history of heating: slow and controlled increase of the Rayleigh number maintains the uni-cellular structure.

- By increasing the Rayleigh number, we have found the following sequence of solutions: stationary - periodic - quasi-periodic - periodic - chaotic. Thermal plumes are generated in the lower unstable boundary layer for large value of the Rayleigh number ($Ra \geq 520$).
- For a fixed value of the Rayleigh number, the system exhibits multistability. Applying infinitesimal perturbations to the conduction state, the threshold of stability is determined by using simplified equations obtained by linearizing the basic equations. In order to solve the linear problem, the finite difference scheme has been substituted by a spectral collocation method, which guarantees spectral accuracy. The analytical solutions confirm the results.
- The asymptotic evolution of the perturbations is calculated by reducing first the original infinite system of partial differential equations to a non linear system of coupled ordinary differential equations for the amplitudes of the few modes that govern the dynamics near the threshold (adiabatic elimination).
- Far from the threshold, the above amplitude equations need many modes to describe the dynamics. We provide qualitatively and quantitatively convergence of the bifurcation diagrams, showing our limitations when we increase the degrees of freedom. The bifurcation diagrams have been computed with AUTO [68], a bifurcation analysis package for ordinary differential equations.
- In the chaotic regime, synchronization is possible if the cells are coupled with all the internal points and a sufficient strong coupling. These requirements are quite demanding and in view of future experimental realization not very encouraging. Let us recall that synchronization through the lateral walls failed as well as when only every 4 grid points were connected in space (6% of the total number of mesh

points). If we connect 25% of the total number of mesh points, synchronization is achieved, but the solution falls in the three-cellular mode [79].

- By using 2D non uniform grid (spectral method) the minimal number of connectors is outstandingly decreased. Also chaotic behaviors are reproduced with only 36×36 Chebyshev points and again synchronization is obtained by coupling all the internal points.

Appendix A

Finite Difference methods

Rayleigh-Bénard convection is so important that many numerical methods have been developed and tried for this problem over the years [80; 81]. Unfortunately, most of these methods have not been compared with each other to determine which best achieves a practical balance of efficiency, accuracy, ease of programming, and parallel scalability on some specific computer architecture. In this thesis we use two numerical scheme: finite difference methods [82; 83; 84] and spectral methods [63; 85; 86]. The purpose of this appendix is to explain the basic ideas of the finite difference approximation and to propose a serie of improvement which lead to the final code.

A.1 Solution of diffusive initial value problem

Let us consider the two-dimensional diffusion equation:

$$\frac{\partial T}{\partial t} = \nabla^2 T. \quad (\text{A.1})$$

We will begin considering how to solve the diffusion equation numerically by deriving some finite difference approximations to the Laplacian term [80; 84; 87; 88]. The basic idea of a finite difference procedure is to replace the continuous problem domain with a finite-difference mesh containing a finite number of grid points. In order to represent a function f on a two-dimensional domain spanned by Cartesian coordinates (x, y) , we use $f(i\Delta x, j\Delta y)$. The grid points are located according to values of i and j , so the equations are usually written in terms of the general point (i, j) and

its neighbors. The standard approach for approximating the differentials comes from truncated Taylors series [89; 90]. The Laplacian is written as

$$\nabla^2 T = \frac{T_{i+1,j} - 2T_{i,j} + T_{i-1,j}}{\Delta^2} + \frac{T_{i,j+1} - 2T_{i,j} + T_{i,j-1}}{\Delta^2}, \quad (\text{A.2})$$

where i and j number the grid lines in the y and the x directions respectively, with $i, j = 0, \dots, N$, of a 2-D square grid. Formula (A.2) is a second-order accurate approximation in the grid size spacing. However, including more and more neighboring points, higher order schemes can be obtained. Apart from the discretization of the thermal diffusion term we need to add the time derivative for the left-hand-side. Using a forward time step the approximation of the diffusion equation can be written

$$T_{i,j}^{n+1} = T_{i,j}^n + \alpha (T_{i+1,j}^n - 2T_{i,j}^n + T_{i-1,j}^n + T_{i,j+1}^n - 2T_{i,j}^n + T_{i,j-1}^n), \quad (\text{A.3})$$

where

$$\alpha = \frac{\Delta t}{\Delta^2} \quad (\text{A.4})$$

physically corresponds to the number of grid points that the heat flux reaches in a time step (or it is the inverse of the number of time step required for heat to diffuse a grid space) [91; 92].

It is evident that a variety of numerical schemes can be written, but they are not all equally acceptable. The difference representation given by (A.3) is referred to as the simple explicit scheme for the heat diffusion equation (Euler scheme). An explicit scheme is one for which only one unknown appears in the difference equation in a manner that permits evaluation in terms of known quantities.

The first requirement that any scheme should meet is that of stability and the stability requirement for the method represented by (A.3) is

$$\alpha \leq \frac{1}{4}. \quad (\text{A.5})$$

This means that a decrease in grid spacing, for example, by a factor of 2 in both direction requires a factor of 16 computer time. In fact, this choice for Δx implies that the grid's point numbers is increased by a factor 4 and from the condition (A.5) it follows that the new Δt is four times smaller than the original time step. Unfortunately, because the simplest centered schemes are only second order in space (and first order in time), we gain only a factor of 4 in reducing the truncation error.

A.2 Implicit scheme

If we use an explicit scheme we have to choose time steps that satisfy the restriction (A.5). But, sometimes time steps comparable to, or smaller than, $(\Delta x)^2/4$ may be physically unreasonable. For this reason we will use an implicit scheme which is unconditionally stable.

In an explicit scheme we have only one unknown, since the diffusion equation governs a marching problem for which an initial distribution of T must be specified. The temperature field T at time level n can be considered to be known. If the second derivative term in the equation were approximated by the temperature field taken at the $n + 1$ time level, three unknowns would appear in the difference equation. In this case the procedure is called implicit, indicating that the algebraic formulation would require the simultaneous solution of several equations involving the unknowns. The simplest implicit scheme for the heat diffusion equation can be developed from the Taylor series by simply evaluating the heat diffusion term at the $n + 1$ time level (all we have to do is to rewrite equation (A.3) replacing the diffusion rate at time step n with that at time step $n + 1$). A second order scheme in both time and space, can be obtained simply averaging the explicit and implicit schemes (Crank-Nicholson scheme). The latter into two dimensions leads to a band tridiagonal system which is significant more expensive computationally. One possibility to solve them is to use a sparse matrix technique, or another approach, which combines second order accuracy in space and time with the ease of tridiagonal solvers, it is the Alternating-Direction Implicit scheme.

A.2.1 Alternating-Direction Implicit scheme

One possibility is to use the ADI scheme, the idea is to split one process into its different directional components. For example, we could rewrite our multidimensional diffusion equation as

$$\frac{\partial T}{\partial t} = \mathcal{L}_x T + \mathcal{L}_y T \quad (\text{A.6})$$

where \mathcal{L}_x is the operator controlling diffusion in the horizontal direction and \mathcal{L}_y controls diffusion in the vertical direction. Given this splitting, ADI schemes then solve (A.6) by taking two-passes, first solving an implicit diffusion equation in the horizontal for the first half time step and then an

implicit diffusion equation in the vertical for the second half time step. In more detail, the ADI algorithm for (A.1) looks like

$$\begin{aligned} \frac{T_{i,j}^{n+\frac{1}{2}} - T_{i,j}^n}{\Delta t/2} &= \frac{1}{\Delta x^2} \left(T_{i+1,j}^{n+\frac{1}{2}} - 2T_{i,j}^{n+\frac{1}{2}} + T_{i-1,j}^{n+\frac{1}{2}} \right) \\ &\quad + \frac{1}{\Delta y^2} \left(T_{i,j+1}^n - 2T_{i,j}^n + T_{i,j-1}^n \right) \end{aligned} \quad (\text{A.7})$$

$$\begin{aligned} \frac{T_{i,j}^{n+1} - T_{i,j}^{n+\frac{1}{2}}}{\Delta t/2} &= \frac{1}{\Delta x^2} \left(T_{i+1,j}^{n+\frac{1}{2}} - 2T_{i,j}^{n+\frac{1}{2}} + T_{i-1,j}^{n+\frac{1}{2}} \right) \\ &\quad + \frac{1}{\Delta y^2} \left(T_{i,j+1}^{n+1} - 2T_{i,j}^{n+1} + T_{i,j-1}^{n+1} \right) \end{aligned} \quad (\text{A.8})$$

Only one tridiagonal system of equations must be solved for each half step. The equation (A.8) is an implicit, tridiagonal equation for the horizontal rows at time $n + 1/2$ which are then used in the equation (A.8) to update the vertical columns at time $n + 1$. The advantage of this method is that each time step requires only the solution of two simple tridiagonal systems.

A.3 The non-linear term

Our diffusion equation is not linear, it has the following form

$$\frac{\partial T}{\partial t} = \nabla^2 T + J, \quad (\text{A.9})$$

where J is the Jacobian non linear term and in two dimensions it is written

$$J = \frac{\partial \psi}{\partial y} \frac{\partial T}{\partial x} - \frac{\partial \psi}{\partial x} \frac{\partial T}{\partial y} \quad (\text{A.10})$$

this term is also known as the *advection term*. By studying the way to construct a computer model of the general circulation of the atmosphere, Arakawa [52] has explained that a simple finite difference approximation using central differences, for example

$$\frac{\partial \psi}{\partial y} \frac{\partial T}{\partial x} = \frac{(\psi_{i+1,j} - \psi_{i-1,j})(T_{i,j+1} - T_{i,j-1})}{4\Delta^2} \quad (\text{A.11})$$

causes numerical instability. At first he thought that it were “truncation error”. A computer cannot produce numbers with infinite precision. When

thousands of calculation are repeated and the numbers are truncated each time, we add up tiny discrepancies over and over. As result we have a big discrepancy. Eventually the solutions became unrealistic and “explode”. But after that Arakawa recognized that the instability was like the problem of a platoon of soldiers ordered to march across a bridge. If they march across in step, it may happen that somewhere there is a combination that resonates at just the frequency of their marching. Each time the feet come down, they hit that combination at the same phase of its swing, pushing it a little further. Soldiers know that bridges can resonate and they will break step before crossing.

Something like this happened with Arakawa’s simulations. Suppose the computer goes through a complete step and takes its next step after a simulation interval of, for example, one hour. Among the simulated waves there would be some with a frequency of just one hour. Every time the calculation was repeated, the computer would catch those waves at the same phase (aliasing occurs when the sampling frequency is too low with respect to the frequency content in the original time series. A new, but false frequency is obtained by the sampling procedure). Arakawa sought a way to make the small pushes cancel one another out, as the impact of the feet of the soldiers would cancel one another if they broke step. The key, he found, was to write equations in such a way that certain quantities would remain unchanged. For example, the kinetic energy. In the real world, the law of conservation of energy demands that there is never any change in the total energy, whereas kinetic energy alone is not normally conserved. But by using equations that did conserve kinetic energy, Arakawa could make sure that no unrealistic spike of wind speed grew exponentially from his calculations.

To avoid aliasing errors Arakawa developed nine- and thirteen-point representations of the Jacobian J which conserve the kinetic energy and which have a truncation error of the square and fourth power, respectively, of the spatial difference Δx . These numerical schemes are known as the second and fourth-order Arakawa schemes.

We choose second order Arakawa scheme. There are different possibilities

of writing the expression for the Jacobian [53; 54]:

$$\begin{aligned}
J(\psi, T) &= \frac{\partial \psi}{\partial y} \frac{\partial T}{\partial x} - \frac{\partial \psi}{\partial x} \frac{\partial T}{\partial y} \\
&= \frac{\partial}{\partial x} \left(\psi \frac{\partial T}{\partial y} \right) - \frac{\partial}{\partial y} \left(\psi \frac{\partial T}{\partial x} \right) \\
&= \frac{\partial}{\partial y} \left(T \frac{\partial \psi}{\partial x} \right) - \frac{\partial}{\partial x} \left(T \frac{\partial \psi}{\partial y} \right) \\
&= \frac{1}{2r} \left\{ \left(\frac{\partial \psi}{\partial y} - r \frac{\partial \psi}{\partial x} \right) \left(\frac{\partial T}{\partial y} + r \frac{\partial T}{\partial x} \right) - \left(\frac{\partial T}{\partial y} - r \frac{\partial T}{\partial x} \right) \left(\frac{\partial \psi}{\partial y} + r \frac{\partial \psi}{\partial x} \right) \right\}
\end{aligned}$$

The last expression follows from

$$\begin{aligned}
\eta &= x - \frac{y}{r} \\
\xi &= x + \frac{y}{r}
\end{aligned}$$

from which

$$\begin{aligned}
\frac{\partial}{\partial \eta} &= \frac{1}{2} \left(\frac{\partial}{\partial x} - r \frac{\partial}{\partial y} \right), \\
\frac{\partial}{\partial \xi} &= \frac{1}{2} \left(\frac{\partial}{\partial x} + r \frac{\partial}{\partial y} \right),
\end{aligned} \tag{A.12}$$

and

$$J(\psi, T) = \frac{2}{r} \left\{ \frac{\partial \psi}{\partial y} \frac{\partial T}{\partial x} - \frac{\partial \psi}{\partial x} \frac{\partial T}{\partial y} \right\} \tag{A.13}$$

The resulting schemes will depend on the choice of the mathematical expression for the Jacobian. From the first expression we have

$$J^{++} = \frac{1}{4\Delta x \Delta y} \left\{ (\psi_{i,j+1} - \psi_{i,j-1})(T_{i+1,j} - T_{i-1,j}) - (\psi_{i+1,j} - \psi_{i-1,j})(T_{i,j+1} - T_{i,j-1}) \right\},$$

from the second expression we get:

$$\begin{aligned}
J^{+\times} &= \frac{1}{4\Delta x \Delta y} \left\{ \psi_{i,j+1}(T_{i+1,j+1} - T_{i-1,j+1}) - \psi_{i,j-1}(T_{i+1,j-1} - T_{i-1,j-1}) \right. \\
&\quad \left. - \psi_{i+1,j}(T_{i+1,j+1} - T_{i+1,j-1}) + \psi_{i-1,j}(T_{i-1,j+1} - T_{i-1,j-1}) \right\}, \tag{A.14}
\end{aligned}$$

the third one leads to:

$$\begin{aligned} J^{\times+} &= \frac{1}{4\Delta x \Delta y} \left\{ T_{i+1,j}(\psi_{i+1,j+1} - \psi_{i+1,j-1}) - T_{i-1,j}(\psi_{i-1,j+1} - \psi_{i-1,j-1}) \right. \\ &\quad \left. - T_{i,j+1}(\psi_{i+1,j+1} - \psi_{i-1,j+1}) + T_{i,j-1}(\psi_{i+1,j-1} - \psi_{i-1,j-1}) \right\}, \end{aligned} \quad (\text{A.15})$$

finally, from the last one with $r = \Delta y / \Delta x$:

$$\begin{aligned} J^{\times\times} &= \frac{1}{8\Delta x \Delta y} \left\{ (\psi_{i-1,j+1} - \psi_{i+1,j-1})(T_{i+1,j+1} - T_{i-1,j-1}) \right. \\ &\quad \left. - (\psi_{i+1,j+1} - \psi_{i-1,j-1})(T_{i-1,j+1} - T_{i+1,j-1}) \right\}. \end{aligned} \quad (\text{A.16})$$

A viable form to represent the Jacobian is

$$J = aJ^{++} + bJ^{\times+} + cJ^{+\times} + dJ^{\times\times}, \quad a + b + c + d = 1 \quad (\text{A.17})$$

In the discretized expression for the Jacobian J the two super-indices indicate the points where ψ and T are evaluated respectively. For example, $J^{+\times}$ means that ψ is evaluated in the adjacent horizontal and vertical points and T is evaluated with the neighboring points on the diagonals. In the present thesis, we have chosen to use $d = 0$ and $a = b = c = 1/3$ for the discretization of the Jacobian [30].

A.3.1 ADI scheme revisited

The method until now is known as single-step because it uses information from only the last step computed. The value T_{ij}^{n+1} depends only on T_{ij}^n . It exists a class of methods that use past values for the approximation of the solution. They are known as multistep methods. By adding the non-linear term and using a second-order Adams-Bashforth method in the diffusion equation, the ADI scheme is modified as follow:

$$[-1 \quad \alpha + 2 \quad -1] T^{n+\frac{1}{2}} = \begin{bmatrix} 1 \\ \alpha - 2 \\ 1 \end{bmatrix} T^n - \frac{\Delta t}{2} \rho \quad (\text{A.18})$$

$$\begin{bmatrix} -1 \\ \alpha + 2 \\ -1 \end{bmatrix} T^{n+1} = [1 \quad \alpha - 2 \quad 1] T^{n+\frac{1}{2}} - \frac{\Delta t}{2} \rho \quad (\text{A.19})$$

where

$$\rho = \frac{1}{2} (3J(\psi^n, T^n) - J(\psi^{n-1}, T^{n-1})) \quad (\text{A.20})$$

In the ADI scheme we have to solve two tridiagonal systems, one for each spatial directions at every time step. We have not spoken yet about the implementation of boundary conditions. The equations (A.18) and (A.19) can be used to calculate the solution at the internal points, while the temperatures at the boundaries are supplied by the given boundary conditions. In the first half step we have to solve an implicit system in the x direction. In this case, the boundary condition that we have to consider are the condition at the lateral walls. We imposed a Neumann boundary condition that fixes the heat flux ($= 0$) at the boundary

$$\frac{\partial T}{\partial x}(0, y) = \frac{\partial T}{\partial x}(1, y) = 0. \quad (\text{A.21})$$

Hence we can obtain the temperature at the boundary by approximating the derivative in (A.21) by a finite difference. In sections 3.1 and 3.2, we have written a first approximation for the first derivative using only two points

$$\frac{\partial T_{i,0}}{\partial x} = \frac{T_{i,1} - T_{i,0}}{\Delta}; \quad \frac{\partial T_{i,N}}{\partial x} = \frac{T_{i,N} - T_{i,N-1}}{\Delta}. \quad (\text{A.22})$$

From (A.21) and (A.22) we deduce that

$$T_{i,0} = T_{i,1} \quad T_{i,N} = T_{i,N-1}. \quad (\text{A.23})$$

A derivative using three points formula increases the precision

$$\begin{aligned} \frac{\partial T_{i,0}}{\partial x} &= \frac{-3T_{i,0} + 4T_{i,1} - T_{i,2}}{2\Delta} \\ \frac{\partial T_{i,N}}{\partial x} &= \frac{T_{i,N-2} - 4T_{i,N-1} + 3T_{i,N}}{2\Delta} \end{aligned}$$

from which

$$T_{i,0} = \frac{4T_{i,1} - T_{i,2}}{3} \quad T_{i,N} = \frac{4T_{i,N-1} - T_{i,N-2}}{3}. \quad (\text{A.24})$$

For the second half step in the vertical direction we consider the upper and lower boundaries, where Dirichlet boundary condition are imposed:

$$T_{0,j} = 1 \quad \text{at the bottom} \quad (\text{A.25})$$

and

$$T_{N,j} = 0 \quad \text{at the top of the layer} \quad (\text{A.26})$$

A.4 Boundary value problem

In the previous section we have been concerned with time dependent initial value problems where we start with some assumed initial condition (plus appropriate boundary conditions), then we calculate how this solution will change in time. Now we consider the simplest elliptic problem which is a Poisson problem of the form:

$$\nabla^2 u = f(x, y) \quad (\text{A.27})$$

We have already discussed finite difference approximations in the previous sections on 2-D initial value problems. For boundary value problems, nothing has changed except that we do not have any time derivatives to deal with any more. For example, the standard 5-point discretization of the equation (A.27) on a regular 2-D cartesian mesh with uniform grid ($\Delta x = \Delta y = \Delta$) is:

$$\frac{1}{\Delta^2} (u_{i+1,j} - 2u_{i,j} + u_{i-1,j}) + \frac{1}{\Delta^2} (u_{i,j+1} - 2u_{i,j} + u_{i,j-1}) = f_{i,j} \quad (\text{A.28})$$

Finally, a note about boundary conditions. For determining T it is necessary to specify the boundary conditions. In general boundary conditions add auxiliary information that modify the matrix or the right hand-side or both. However, there are many ways to implement the boundary conditions and these depend somewhat on the method of solution. In general, for Dirichlet boundary conditions, because matrix methods can be so expensive, the fewer points the better so one approach is just to solve the unknown interior points. For certain classes of problems, of which the Poisson problem is one example, there are rapid methods that can take advantage of some of the special properties of the underlying matrix.

Problems with regular boundaries and constant coefficient stencil can often be solved using the Fast Fourier transform. A more general set of rapid methods, however exists for problems that are separable, in the sense of separation of variables. These methods include cyclic reduction. Numerical Recipes [87] gives a brief explanation of how these methods work which we do not repeat here. We use a collection of codes called FISHPAK packages [93]. These are a collection of generalized cyclic reduction Fortran routines for solving more general Helmholtz problems, 3-D Cartesian coordinates and general 2-D separable elliptic problem, for any combination

of periodic or mixed boundary conditions. These codes are extremely fast with solution time scaling like $N^2 \log N$, but they were written back in the eighties and the Fortran is inscrutable and therefore hard to modify for different boundary conditions. In addition they still only work for separable problems and could not, for example solve the more general problem $\nabla \cdot k \nabla T = \rho$ for a space varying conductivity. However, the only solvers that can compete in time with these routines and handle spatially varying coefficients are the iterative multi-grid solvers.

A.4.1 Explicit time-stepping procedure

In previous sections we have seen how we can solve a non-linear diffusion equation as well as the Poisson equation, so we have all the elements in order to study our specific problem. The latter we remember to be:

$$\frac{\partial T}{\partial t} = \nabla^2 T + \frac{\partial \psi}{\partial y} \frac{\partial T}{\partial x} - \frac{\partial \psi}{\partial x} \frac{\partial T}{\partial y} \quad (\text{A.29})$$

$$\nabla^2 \psi = -Ra \frac{\partial T}{\partial x}, \quad (\text{A.30})$$

$$T(x, 0) = 1; \quad T(x, 1) = 0, \quad (\text{A.31})$$

$$\frac{\partial T}{\partial x}(0, y) = \frac{\partial T}{\partial x}(1, y) = 0. \quad (\text{A.32})$$

We first discretize equations (A.30)-(A.32) in space by using second-order centered differences at the grid point (i, j) for $i = 1, \dots, N - 1$ and $j = 1, \dots, M - 1$ ($i = 0$ or N or $j = 0$ or M represent the points on the boundary). In particular the advection term is discretized using Arakawa scheme. The resulting equations are

$$\partial_t T_{ij} = G_1(T_{ij}, \psi_{ij}) \quad (\text{A.33})$$

$$\nabla^2 \psi_{ij} = -Ra G_2(T_{ij}) \quad (\text{A.34})$$

where G_1 and G_2 represent finite difference approximation for all the terms except the one with time derivative in (A.34). We use second-order forward and backward differences for the boundary condition of T .

We use a second-order Adams-Bashforth scheme to iterate in time

$$T_{ij}^{n+1} = T_{ij}^n + \frac{\Delta t}{2} \nabla^2 T_{ij}^n + \frac{\Delta t}{2} (3J(T_{ij}^n, \psi_{ij}^n) - J(T_{ij}^{n-1}, \psi_{ij}^{n-1})). \quad (\text{A.35})$$

More precisely, the scheme is implemented in the following way:

I. Initialization of the temperature and stream function at the time step n and also at $n - 1$. We suppose that the temperature has a linear vertical distribution. The stream function is identically zero.

II. Evaluate the intermediate temperature $T^{n+\frac{1}{2}}$ by solving the implicit diffusion equation in the horizontal direction for the first half time step

$$T_{ij}^{n+1/2} = T_{ij}^n + \frac{\Delta t}{2} \nabla^2 T_{ij}^n + \frac{\Delta t}{4} (3J(T_{ij}^n, \psi_{ij}^n) - J(T_{ij}^{n-1}, \psi_{ij}^{n-1})) \quad (\text{A.36})$$

for $i = 1, \dots, N - 1$ and $j = 1, \dots, M - 1$.

III. Implement lateral boundary conditions on $T_{ij}^{n+1/2}$.

IV. Evaluate the temperature T^{n+1} solving the implicit diffusion equation along the vertical direction for the second half time step

$$T_{ij}^{n+1} = T_{ij}^{n+1/2} + \frac{\Delta t}{2} \nabla^2 T_{ij}^{n+1/2} + \frac{\Delta t}{4} (3J(T_{ij}^n, \psi_{ij}^n) - J(T_{ij}^{n-1}, \psi_{ij}^{n-1})) \quad (\text{A.37})$$

for $i = 1, \dots, N - 1$ and $j = 1, \dots, M - 1$.

V. Implement top and bottom boundary conditions on T_{ij}^{n+1} .

VI. Solve

$$\nabla^2 \psi_{ij}^{n+1} = -RaG_2(T_{ij}^{n+1}). \quad (\text{A.38})$$

by the generalized cyclic reduction routine from the FISHPACK package.

VII. Implement boundary conditions on ψ_{ij}^{n+1} .

VIII. Go to the next time step.

Appendix B

Spectral collocation method

At first sight, the simple geometry of the Hele-Shaw cell did not give us any reasons to look for complicated methods of discretization. By combining various truncated Taylor series, it is possible to derive several difference schemes. The end product is a weighted combination of the values of the functions at neighboring points. But as we progressed in the thesis, it was clear that we needed to consider new methods able to describe the dynamics near the boundary layers. An alternative way to derive approximations for derivatives is by interpolation and differentiation. Given discrete data on a grid, the fundamental principle of spectral collocation methods is to interpolate the data globally and then evaluate the derivative of the interpolant on the grid [63; 85; 86]. Figure B.1 shows the convergence of fourth-order finite difference and periodic spectral method for the derivative of $e^{\sin(x)}$ in $[-\pi, \pi]$. We compare the approximations with the exact derivative, $e^{\sin(x_j)}\cos(x_j)$, for various value of N . Using finite difference approximation, the differentiation matrix is penta-diagonal and permits high values of N . Using spectral method, the matrix is dense, but the error is smaller. It decreases very rapidly until rounding errors on the computer prevent any further improvement. This is the so-called spectral accuracy. Generally, if the problem has periodic domain the natural choice is a trigonometric polynomial on equispaced grid. For non periodic domains and non periodic functions, one approach is to assume that the functions were periodic and use trigonometric interpolation in equispaced points. But generally this method sacrifices the accuracy advantages of spectral method. It is customary to replace trigonometric polynomials by algebraic polynomials on irregular grid.

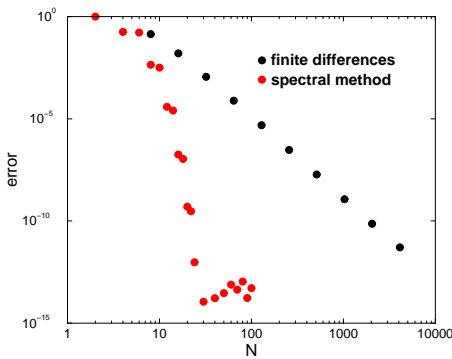


Figure B.1: Convergence of periodic spectral method and of fourth-order difference scheme. (Notice the logarithmic scales for both axes).

B.1 Chebyshev points

Different sets of unevenly spaced points are effective for the interpolation, but they have all a common property. Asymptotically as $N \rightarrow \infty$, the points are distributed with the density:

$$d \sim \frac{N}{\pi\sqrt{1-x^2}}. \quad (\text{B.1})$$

A set of points that satisfy (B.1) is the so-called *Chebyshev points*,

$$x_j = \cos(j\pi/N), \quad j = 0, 1, \dots, N. \quad (\text{B.2})$$

Geometrically, we can visualize these points as the projections on $[-1, 1]$ of equispaced points on the upper half of the unit circle, as in Fig. B.2.

If $N = 1$, from (B.2) the interpolation points are $x_0 = 1$ and $x_1 = -1$ and the interpolating polynomial through the data f_0 and f_1 , written in Lagrange form, is

$$y(x) = \frac{1}{2}(1+x)f_0 + \frac{1}{2}(1-x)f_1. \quad (\text{B.3})$$

The derivative is

$$y'(x) = \frac{1}{2}f_0 - \frac{1}{2}f_1, \quad (\text{B.4})$$

that is

$$f' = C_1 f, \quad (\text{B.5})$$

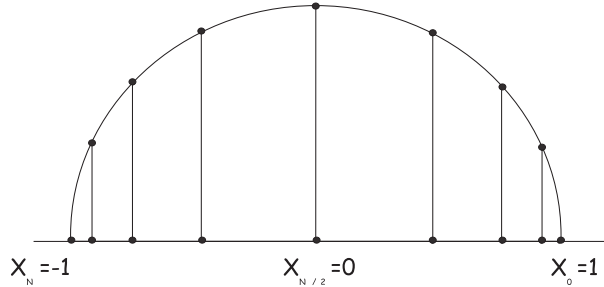


Figure B.2: Chebyshev points are the projection onto the x -axis of equally spaced points on the unit circle.

where

$$C_1 = \begin{pmatrix} \frac{1}{2} & -\frac{1}{2} \\ \frac{1}{2} & -\frac{1}{2} \end{pmatrix}, \quad (\text{B.6})$$

is a 2×2 Chebyshev differentiation matrix. For $N = 2$ the interpolation points are $x_0 = 1$, $x_1 = 0$ and $x_2 = -1$, and the interpolant is the quadratic

$$y(x) = \frac{1}{2}x(1+x)f_0 + (1+x)(1-x)f_1 + \frac{1}{2}x(x-1)f_2. \quad (\text{B.7})$$

The derivative is the linear polynomial

$$y'(x) = (x + \frac{1}{2})f_0 - 2xf_1 + (x - \frac{1}{2})f_2. \quad (\text{B.8})$$

The differentiation matrix is, in this case, the 3×3 matrix

$$C_2 = \begin{pmatrix} \frac{3}{2} & -2 & \frac{1}{2} \\ \frac{1}{2} & 0 & -\frac{1}{2} \\ -\frac{1}{2} & 2 & -\frac{3}{2} \end{pmatrix}. \quad (\text{B.9})$$

Generally, for each $N \geq 1$ the entries of the Chebyshev spectral differentiation matrix are [63]

$$(C_N)_{00} = \frac{2N^2 + 1}{6}, \quad (C_N)_{NN} = -\frac{2N^2 + 1}{6}, \quad (\text{B.10})$$

$$(C_N)_{jj} = -\frac{x_j}{2(1 - x_j^2)}, \quad j = 1, \dots, N - 1 \quad (\text{B.11})$$

$$(C_N)_{ij} = \frac{c_i}{c_j} \frac{(-1)^{i+j}}{(x_i - x_j)}, \quad i \neq j, \quad i, j = 0, \dots, N \quad (\text{B.12})$$

where

$$c_i = \begin{cases} 2, & i = 0 \quad \text{or} \quad N, \\ 1, & \text{otherwise.} \end{cases} \quad (\text{B.13})$$

B.2 Solving the eigenvalue problem

Spectral methods provide the great advantage of spectral accuracy. However, the implementation of the matrix C_N may result very difficult, especially for imposing boundary conditions. We start modifying and using such matrix to solve the eigenvalue problem (4.8)-(4.34), for which the description of the method result simpler, to show after in which way the procedure described in section A.4.1 changes. The equations are partial differential equations of second order in $[0, 1] \times [0, 1]$. Defining the Chebyshev points as in figure B.2 we need the new variables $\tilde{x} = 2x - 1$ and $\tilde{y} = 2y - 1$, with $\tilde{x}, \tilde{y} \in [-1, 1]$. Equations (4.34)-(4.8) become:

$$(D_{\tilde{x}}^2 + D_{\tilde{y}}^2)\tilde{g} + \frac{1}{2}RaD_{\tilde{x}}\tilde{f} = 0 \quad (\text{B.14})$$

$$(D_{\tilde{x}}^2 + D_{\tilde{y}}^2)\tilde{f} - \frac{1}{2}D_{\tilde{x}}\tilde{g} = 0 \quad (\text{B.15})$$

with boundary conditions

$$\tilde{g} = \tilde{f} = 0 \quad \tilde{y} = -1, 1, \quad \tilde{x} \in [-1, 1] \quad (\text{B.16})$$

$$D_{\tilde{x}}\tilde{f} = \tilde{g} = 0 \quad \tilde{x} = -1, 1 \quad \tilde{y} \in [-1, 1] \quad (\text{B.17})$$

In the following, tildes are omitted. For such problem, it is useful to set up a grid based on Chebyshev points independently in each direction, called a tensor product grid, see figure B.3. The easiest way to solve a problem on a tensor product spectral grid is to use tensor product, also known as

Kronecker product. If A and B are two matrices of dimensions $p \times q$ and $r \times s$ respectively, the Kronecker product, denoted by $A \otimes B$, is the matrix of dimension $pr \times qs$ with $p \times q$ block form, where the i,j block is $a_{i,j}B$. For example,

$$\begin{pmatrix} 1 & 2 \\ 3 & 4 \end{pmatrix} \otimes \begin{pmatrix} a & b \\ c & d \end{pmatrix} = \begin{pmatrix} a & b & | & 2a & 2b \\ c & d & | & 2c & 2d \\ \hline 3a & 3b & | & 4a & 4b \\ 3c & 3d & | & 4c & 4d \end{pmatrix} \quad (\text{B.18})$$

To explain how Kronecker products can be used in our case, let us consider the case $N = 3$. Suppose we have the initial nodes as shown in figure B.3. f and g have to be evaluated on the black and red nodes, respectively. We recall that f and g are the temperature and the stream function perturbations, respectively, for which g vanishes on all boundaries, while f is zero on the upper and lower boundary and its partial derivative respect to x is zero on the lateral walls. We suppose to have the data $F = (f_0, f_1, \dots, f_7)^T$ and $G = (g_1, \dots, g_3)^T$ at the interior grid points. We approximate the Laplacian by differentiating spectrally in the x and y directions independently. The first and second partial derivatives can be computed by the Kronecker product of C_N and the square of C_N respectively, with the identity matrix I :

$$\begin{aligned} D_x &= C_N \otimes I, \\ D_x^2 &= C_N^2 \otimes I \\ D_y^2 &= I \otimes C_N^2. \end{aligned} \quad (\text{B.19})$$

Let us consider equation (B.15). The boundary conditions imply that the first and last columns of C_N^2 have no effect, as the first and last rows. The 2×2 differentiation matrix with $N = 3$ in one dimension is given by the square of the matrix defined by (B.10)-(B.13), to which we remove the first and last columns and rows:

$$\tilde{C}_3^2 = \begin{pmatrix} -5.3 & 2.6 \\ 2.6 & -5.3 \end{pmatrix}. \quad (\text{B.20})$$

If I denotes the 2×2 identity, then the second derivative with respect to

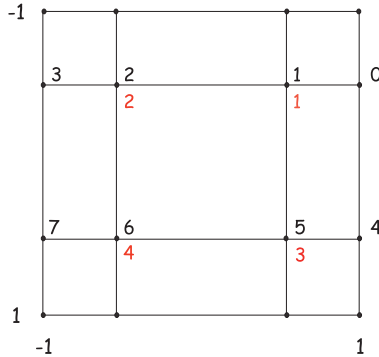


Figure B.3: A tensor product grid. Red points are nodes of g . Black points are nodes of f .

x will be computed by the matrix:

$$I \otimes \tilde{C}_3^2 = \left(\begin{array}{cc|c} -5.3 & 2.6 & \\ 2.6 & -5.3 & \\ \hline & & -5.3 & 2.6 \\ & & 2.6 & -5.3 \end{array} \right). \quad (\text{B.21})$$

The second derivative with respect to y will be computed by:

$$\tilde{C}_3^2 \otimes I = \left(\begin{array}{cc|c} -5.3 & 2.6 & \\ -5.3 & 2.6 & \\ \hline 2.6 & -5.3 & \\ 2.6 & -5.3 & \end{array} \right). \quad (\text{B.22})$$

The discrete Laplacian for g is now the Kronecker sum

$$L_{4 \times 4}^{(g)} = I \otimes \tilde{C}_3^2 + \tilde{C}_3^2 \otimes I. \quad (\text{B.23})$$

The construction of the Laplacian for f is slightly different because of the different boundary conditions. At the nodes 0, 3, 4 and 7 we wish to impose a condition involving the first derivative with respect to x . For this purpose we will use the spectral differentiation matrix C_3 . Starting from C_3^2 , where the first and last rows have been extracted from C_3 , we compute the second derivative with respect to x . In order to calculate the Laplacian of Eq. (B.23), we need to calculate the derivative with respect

to y , $(\tilde{C}_3^2 \otimes I)$. After having imposed the first and last row of \tilde{C}_3^2 equal to zero, we calculate the Kronecker product $\tilde{C}_3^2 \otimes I$, which we add to $I \otimes \tilde{C}_3^2$. For $N = 3$ solving (B.14)-(B.17) means to solve the eigenvalue problem

$$\left(\begin{array}{c|c} L_{8 \times 8}^{(f)} & -\frac{1}{2} D_{8 \times 4}^{(g)} \\ \hline & L_{4 \times 4}^{(g)} \end{array} \right) \begin{pmatrix} f_0 \\ f_1 \\ f_3 \\ f_4 \\ f_5 \\ f_6 \\ f_7 \\ g_1 \\ g_2 \\ g_3 \\ g_4 \end{pmatrix} = -\frac{1}{2} Ra \left(\begin{array}{c|c} & \\ \hline & D_{4 \times 8}^{(f)} \end{array} \right) \begin{pmatrix} f_0 \\ f_1 \\ f_3 \\ f_4 \\ f_5 \\ f_6 \\ f_7 \\ g_1 \\ g_2 \\ g_3 \\ g_4 \end{pmatrix} \quad (\text{B.24})$$

$D_{8 \times 4}^{(g)}$ has been constructed starting from C_3 , removing the first and last columns, substituting the first and last rows with zeros, and computing the Kronecker product with $I = I_{2 \times 2}$. $D_{4 \times 8}^{(f)}$ has been constructed starting from C_3 , stripping off the first and last rows and computing the Kronecker product with $I = I_{2 \times 2}$.

$L_{8 \times 8}^{(f)}$ being a no singular matrix, we can solve the simplest eigenvalue problem:

$$L_{8 \times 8}^{(f)} F = \frac{1}{2} D_{8 \times 4}^{(g)} G, \quad (\text{B.25})$$

$$L_{4 \times 4}^{(g)} G = -\frac{1}{2} Ra D_{4 \times 8}^{(f)} F. \quad (\text{B.26})$$

From the Eq. (B.25),

$$F = \frac{1}{2} (L_{8 \times 8}^{(f)})^{-1} D_{8 \times 4}^{(g)} G \quad (\text{B.27})$$

Substituting in (B.26)

$$L_{4 \times 4}^{(g)} G = -\frac{1}{2} Ra \left(\frac{1}{2} D_{4 \times 8}^{(f)} (L_{8 \times 8}^{(f)})^{-1} D_{8 \times 4}^{(g)} \right) G \quad (\text{B.28})$$

Now the eigenvalue problem appears in the generalized form

$$Ax = \lambda Bx \quad (\text{B.29})$$

($\lambda = -1/2Ra!$) and it can be easily solved by the routine GVCRG from the IMSL package.

For the temporal integration of Eqs. (2.23) by using spectral collocation method, the procedure is practically the same as in section A4.1. We initialize the temperature and the stream function at the time step n . The temperature has a linear vertical distribution, while the stream function is identically zero. From the diffusion equation, by advancing in time with a simple Euler scheme, we evaluate the temperature at the time step $n + 1$. By the Poisson equation the stream function is defined at the same time step. At the end of each time step, the boundary conditions are imposed as it has been explained for the eigenvalue problem (B.14)-(B.17).

Bibliography

- [1] A. Pikovsky, M. Rosemblum and J. Kurts. *Synchronization, A Universal concept in Non-linear Science*. Cambrige University Press, UK, 2001.
- [2] O.N. Bjornstad, R.A. Ims and X. Lambin. Spatial population dynamics: analyzing patterns and processes of population synchrony. *Trends in ecology and evolution*, **14**:427–431, 2000.
- [3] O.N. Bjornstad and J. Bascompte. Synchrony and second-order spatial correlation in host-parasitoid systems . *Journal of Animal Ecology*, **70**:924–933, 2001.
- [4] C. Huygens. *Horologium Oscilatorium*. Apud F. Muguet, Parisiis, France, 1673.
- [5] S. Boccaletti, J. Kurts, G. Osipov, D.L. Valladares and C.S. Zhou. The synchronization of chaotic systems. *Phys. Rep.*, **366**:1–101, 2002.
- [6] S. Boccaletti, D.L. Valladares, J. Kurths, D. Maza and H.L. Mancini. Synchronization of chaotic structurally nonequivalent systems. *Phys. Rev. E*, **61**:3172–3715, 2000.
- [7] S.H. Strogatz. *Nonlinear Dynamics and Chaos*. Addison–Wesley, USA, 1994.
- [8] L. Landau and E. Lifshitz. *Fluid Mechanics*. Pergamon, Oxford, 1959.
- [9] Y. Pomeau and P. Manville. Intermittent transition to turbulence in dissipative dynamical systems. *Commun. Math. Phys.*, **74**:189–197, 1980.

- [10] L.M. Pecora and T.L. Carroll. Synchronization in chaotic systems. *Phys. Rev. Lett.*, **64**:821–824, 1990.
- [11] S. Boccaletti, C. Grebogi, Y. C. Lai, H.L. Mancini and D. Maza. The control of chaos: theory and applications. *Phys. Rep.*, **103**:329, 2000.
- [12] U. Dressler and G. Nitsche. Controlling chaos using time delayed coordinates. *Phys. Rev. Lett.*, **68**:1–4, 1992.
- [13] G. Hu and Z. Qu. Controlling spatiotemporal chaos in coupled map lattice systems . *Phys. Rev. Lett.*, **72**:68–71, 1994.
- [14] R.O. Grigoriev, M.C. Cross and H.G. Schuster. Pinning control of spatiotemporal chaos . *Phys. Rev. Lett.*, **79**:2795–2798, 1997.
- [15] L. Junge and U. Parlitz. Synchronization and control of coupled Ginzburg-Landau equations using local coupling. *Phys. Rev. E*, **61**:3736–3742, 1999.
- [16] H.S.J. Hele-Shaw. Investigations of the nature of surface resistance of water and a stream motion under certain experimental conditions. *Trans. Inst. Nav. Arch.*, **40**:21, 1898.
- [17] D.A. Nield and A. Bejan. *Convection in Porous Media*. Springer-Verlag, New York, 1999.
- [18] J. Bragard, S. Boccaletti and H. Mancini. Asymmetric coupling effects in the synchronization of spatially extended chaotic systems. *Phys. Rev. Lett.*, **91**:64103, 2003.
- [19] S. Boccaletti, L.M. Pecora and A. Pelaez. Unifying framework for synchronization of coupled dynamical systems. *Phys. Rev. E*, **63**:066219/1–4, 2001.
- [20] P. Bergé and M. Dubois. Rayleigh-Bénard Convection. *Contemp. Phys.*, **25**:535–582, 1984.
- [21] H. Bénard. Les tourbillons cellulaires dans une nappe liquide. *Rev. Gen. Sci. Puers Appl.*, **11**:1261–1271, 1900.
- [22] Rayleigh, Lord. On convection currents in a horizontal layer of fluid when the higher temperature is on the under side. *Philos. Mag.*, **32**:529–546, 1916.

- [23] S. Chandrasekhar. *Hydrodynamic and hydromagnetic instability*. The Clarendon Press, Oxford, 1961.
- [24] P. Colinet, J.C. Legros and M.G. Velarde. *Nonlinear Dynamics of surface tension driven instability*. Wiley-VCH, 2001.
- [25] H.P.G. Darcy. *Les fontaines publique de la Ville de Dijon*. Victor Dalmont, Paris, 1856.
- [26] B.K. Hartline and C.R.B. Lister. Thermal convection in a Hele-Shaw cell. *J. Fluid Mech.*, **79**:379–389, 1976.
- [27] C.W. Horton and F.T. Rogers. Convection currents in a porous medium. *J. Appl. Phys.*, **16**:367–370, 1945.
- [28] E.R. Lapwood. Convection of a fluid in a porous medium. *Proc. Camb. Phil Soc.*, **44**:508–521, 1948.
- [29] J.P. Caltagirone, M. Cloupeau and M. Combarous. Convection naturelle fluctuante dans une couche poreuse horizontale. *Acad. Sci. Paris*, **273**:833–836, 1971.
- [30] R.N. Horne and M.J. O’Sullivan. Oscillatory convection in porous medium heated from below. *J. Fluid Mech.*, **66**:339–352, 1974.
- [31] A.S.M. Cherkaoui and W.S.D. Wilcock. Characteristics of high Rayleigh number two-dimensional convection in an open-top porous layer heated from below . *J. Fluid Mech.*, **394**:241–260, 1999.
- [32] J.N. Koster and U. Müller. Time-dependent free convection in vertical slots. *Phys. Rev. Lett.*, **47**:1599–1602, 1981.
- [33] J.N. Koster. Freie konvektion in vertikalen spalten. *Dissertation, Universität Karlsruhe*, 1980.
- [34] H. Frick and U. Müller. Oscillatory Hele-Shaw convection. *J. Fluid Mech.*, **126**:521–532, 1983.
- [35] J.Yang, G. Hu and J. Xiao. Chaos Synchronization in Coupled Chaotic Oscillators with Multiple Positive Lyapunov Exponents. *Phys. Rev. Lett.*, **80**:2963–2966, 1997.

- [36] M. Zhan, G. Hu and J. Yang. Synchronization of chaos in coupled systems. *Phys. Rev. E*, **62**:496–499, 2000.
- [37] N.F. Rulkov, M.M. Sushchik and L.S. Tsimring. Generalized synchronization of chaos in directionally coupled chaotic systems. *Phys. Rev. E.*, **51**:980–994, 1995.
- [38] L. Kocarev y U. Parlitz. Generalized synchronization, predictability, and equivalence of unidirectionally coupled dynamical systems. *Phys. Rev. Lett.*, **76**:1816–1819, 1996.
- [39] A.S. Pikovsky, M.G. Rosenblum, G.V. Osipov y J. Kurths. Phase synchronization of chaotic oscillators by external driving. *Physica D*, **104**:219–238, 1997.
- [40] M.G. Rosenblum, A.S. Pikovsky and J.Kurths. Phase Synchronization of Chaotic Oscillators. *Phys. Rev. E.*, **76**:1804–1807, 1996.
- [41] T. Yalçinkaya and Y.C. Lai. Phase Characterization of Chaos. *Phys. Rev. Lett.*, **79**:3885–3888, 1997.
- [42] D. Maza, A. Vallone, S. Boccaletti and H.L. Mancini. Experimental phase synchronization of chaotic convective flows. *Phys. Rev. Lett.*, **85**:5567–5570, 2000.
- [43] M.G. Rosenblum, A.S. Pikovsky and J.Kurths. From Phase to Lag Synchronization in Coupled Chaotic Oscillators. *Phys. Rev. Lett.*, **78**:4193–4196, 1997.
- [44] C. Bizon, J. Werne, A.A. Predtechensky, K. Julien, W.D. McCornik, J.B. Swift and H.L. Swinney. Plume dynamics in quasi-2D turbulent convection. *Chaos*, **7**:107–124, 1996.
- [45] C. Bizon, A.A. Predtechensky, J. Werne, K. Julien, W.D. McCornik, J.B. Swift and H.L. Swinney. Dynamics and scaling in quasi-two-dimensional turbulent convection. *Physica A*, **239**:204–210, 1997.
- [46] J.W. Wooding. Instability of a viscous liquid of variable density in a vertical Hele-Shaw cell. *J. Fluid Mech.*, **7**:501–515, 1960.
- [47] R.P. Davies-Jones. Thermal convection in a infinite channel with no slip side walls. *J. Fluid Mech.*, **44**:695, 1970.

- [48] H. Lamb. *Hydrodynamics*. Cambridge University Press, Cambridge, 1932.
- [49] S. Kimura, G. Shubert and J.M. Strauss. Route to chaos in porous-medium thermal convection. *J. Fluid Mech.*, **166**:305–324, 1986.
- [50] S. Kimura, G. Shubert and J.M. Strauss. Instabilities of steady, periodic and quasi-periodic modes of convection in porous media. *J. Heat Transfer*, **109**:350–355, 1987.
- [51] M.D. Graham and P. Steen. Plume formation and resonant bifurcations in porous-media convection. *J. Fluid Mech.*, **272**:67–89, 1994.
- [52] S. Weart. *Arakawa's Computation Trick*. [www.aip.org/ history/ climate](http://www.aip.org/history/climate), 2001.
- [53] J.M. Beckers. *Méthodes numériques appliquées à l'environnement*. [http:// modb.oce.ulg.ac.be](http://modb.oce.ulg.ac.be), 2002.
- [54] J.M. Beckers. *Mécanique des fluides non-homogènes*. [http:// modb.oce.ulg.ac.be](http://modb.oce.ulg.ac.be), 2000.
- [55] C.K. Aidun and P.H. Steen. Transition to oscillatory convective heat transfer in a fluid-saturated porous medium. *J. Thermophys. H. T.*, **1**:268–273, 1987.
- [56] P. Bergé, Y. Pomeau and C. Vidal. *L'ordre dans le chaos. Vers une approche déterministe de la turbulence*. Hermann, Paris, 1984.
- [57] M.R. Paul, M.C. Cross, P.F. Fischer and H.S. Greenside. Power law behavior of power spectra in low Prandtl number Rayleigh Bénard convection. *Phys. Rev. Lett.*, **87**:154501/1–4, 2001.
- [58] U. Frisch and R. Morf. Intermittency in nonlinear dynamics and singularities at complex times. *Phys. Rev. A*, **23**:2673–2705, 1981.
- [59] H. Kantz and T. Schreiber. *Nonlinear time series analysis*. Cambridge University Press, 1997.
- [60] R. Hegger, H. Kantz and T. Schreiber. *Practical implementation of nonlinear time series methods: The TISEAN package*. www.mpipks-dresden.mpg.de, 1998.

- [61] J.P. Caltagirone and P. Fabrie. Natural convection in a porous medium at high Rayleigh numbers. *Eur. J. Mech. B/Fluids*, **8**:207–227, 1989.
- [62] M.D. Graham and P.H. Steen. Strongly interacting traveling waves and quasiperiodic dynamics in porous medium convection. *Physica D*, **54**:331–350, 1992.
- [63] L.N. Trefthen. *Spectral methods in MATLAB*. PA: Society for Industrial and Applied Mathematics, Philadelphia, 2000.
- [64] H. Haken. *Synergenits: an introduction to non equilibrium phase transitions and self organization in physics, chemistry, and biology*. Springer Verlag, Berlin, 1977.
- [65] W. Eckhaus. *Studies in Nonlinear Stability Theory*. Springer-Verlag, New York, 1965.
- [66] P. Manneville. *Dissipative Structures and Weak Turbulence*. Academic Press, San Diego, 1990.
- [67] E. Hopf. *Abzweigung einer periodischen Lösung von einer stationären Lösung eines Differentialsystems*. Beicht det Math.-Phys. Klasse der Sächsischen Akademie der Wissenschaften zu Leipzig 94, 1942.
- [68] E. Doedel, R. Paffenroth, A. Champneys, T. Fairgrieve, Yu. Kuznetsov, B. Oldaman, S. Sonstade and X. Wong. *Auto 2000: Continuation and bifurcation software for ordinary differential equations (with Homcont)*. Technical Report, Concordia University, 2002.
- [69] E.J. Doedel. AUTO, a program for the automatic bifurcation analysis of autonomous system. *Cong. Numer.*, **30**:265–384, 1981.
- [70] E.J. Doedel and J.P. Kernévez. *AUTO: software for continuation problem in ordinary differential equations with applications*. Technical Report, California Institute of Technology, 1986.
- [71] E.J. Doedel and J.P. and X.J. Wang. *AUTO94: software for continuation problem in ordinary differential equations with applications*. Technical Report, Center for research on parallel computing, California Institute of Technology, 1995.

- [72] Bard Ermentrout. *XPPAUT5.0: the differential equations tool.* <http://www.math.pitt.edu>, 2001.
- [73] P.C. Dauby, Th. Desaive, J. Bragard and P. Cerialier. Amplitude equations for Rayleigh-Bénard convective rolls far from threshold. *Phys. Rew. E*, **64**:066301/1–7, 2001.
- [74] B. Friedman. *Principles and techniques of applied mathematics.* Dover, New York, 1990.
- [75] R. Seydel. *From equilibrium to chaos: practical bifurcation and stability analysis.* Elsevier, New York, 1988.
- [76] M.D. Graham, U. Müller and P.H. Steen. Time-periodic thermal convection in Hele-Shaw slots: the diagonal oscillation. *Phys. Fluids A*, **4**:2382–2393, 1992.
- [77] W. Hu and P.H. Steen. Transition to chaotic natural convection in tall Hele-Shaw slots. *Phys. Fluids*, **8**:1929–1937, 1995.
- [78] S. Boccaletti, J. Bragard and F.T. Arecchi. Controlling and synchronizing space time chaos. *Phys. Rev. E*, **59**:6574–6578, 1999.
- [79] A. Bernardini, J. Bragard and H. Mancini. Synchronization between two Hele-Shaw cells. *Math. Biol. and Eng.*, **1**:339–346, 2004.
- [80] W.J. Minkowycz, E.M. Sparrow, G.E. Schneider and R.H. Pletcher. *Handbook of numerical heat transfer.* Wiley, New York, 1988.
- [81] J.D. Lambert. *Numerical methods for ordinary differential systems: the initial value problem.* Wiley & Sons, London, 1991.
- [82] C. Jordan. *Calculus of finite differences.* Chelsea publishing company, New York, 1965.
- [83] L.M. Milne-Thomson. *The calculus of finite differences.* Macmillan and Co., New York, 1965.
- [84] G.D. Smith. *Numerical solution of partial differential equations: finite difference methods.* Oxford University Press, New York, 1999.
- [85] B. Mercier. *An introduction to numerical analysis of spectral methods.* Springer, Berlin, 1989.

- [86] D. Gottlieb and S.A. Orszag. *Numerical analysis of spectral methods: theory and application*. Society for Industrial and Applied Mathematics, Philadelphia, 1993.
- [87] W.H. Press. *Numerical recipes in FORTRAN: the art of scientific computing*. Cambridge University Press, Cambridge, 1992.
- [88] M. Spiegelman. *Myths & Methods in Modeling*. www.ldeo.columbia.edu/~mspieg, 2000.
- [89] R. Courant. *Differential and integral calculus*. Interscience, 1970.
- [90] E. Landau. *Differential and integral calculus*. Chelsea, New York, 1965.
- [91] W. E and J. Liu. *Vorticity boundary condition and related issue for finite difference schemes*. www.math.umd.edu/~jliu/research, 2000.
- [92] W. E and J. Liu. *Essentially compact schemes for unsteady viscous incompressible flows*. www.math.umd.edu/~jliu/research, 2000.
- [93] P.N. Swarztrauber and R.A. Sweet. Efficient FORTRAN subprograms for the solution of elliptic partial differential equations. *ACM Trans. Math. Soft.*, **5**:352, 1979.

Resumen

Este trabajo presenta una contribución teórica al análisis de los posibles mecanismos de sincronización entre dos celdas de “Hele-Shaw” uniformemente calentadas desde abajo. La celda de Hele-Shaw tiene una dimensión (la anchura) mucho más pequeña que las otras dos, lo que permite reducir el complicado estudio de un flujo tridimensional a dos dimensiones.

En primer lugar se calculan los estados dinámicos de una sola celda utilizando como parámetro de control la diferencia de temperatura entre las partes superior e inferior del sistema. Mediante el método de diferencias finitas se logran visualizar los diferentes estados convectivos que se desarrollan en el fluido.

Considerando dos celdas de Hele-Shaw idénticas se investigan los posibles fenómenos de sincronización introduciendo un acoplamiento térmico bidireccional, prestando particular atención al régimen caótico. Se proponen diferentes esquemas de acoplamiento capaces de llevar a sincronización completa.

Para minimizar el número de acoplamientos necesarios para sincronizar las dos celdas, se recalculan los estados dinámicos del sistema mediante métodos numéricos espectrales. Con este procedimiento resulta más sencillo analizar distribuciones espaciales no homogéneas para los puntos de sincronismo y se logra disminuir de forma notable el numero de conectores.